STRUCTURAL AND DYNAMICAL EVOLUTION OF NANOCRYSTALS

A THESIS SUBMITTED TO
THE GRADUATE SCHOOL OF NATURAL AND APPLIED SCIENCES
OF
MIDDLE EAST TECHNICAL UNIVERSITY

BY

CAN YILDIRIM

IN PARTIAL FULFILLMENT OF THE REQUIREMENTS
FOR
THE DEGREE OF MASTER OF SCIENCE
IN
METALLURGICAL AND MATERIALS ENGINEERING

JULY 2013

Approval of the thesis:

STRUCTURAL AND DYNAMICAL EVOLUTION OF NANOCRYSTALS

submitted by **CAN YILDIRIM** in partial fulfillment of the requirements for the degree of **Master of Science in Metallurgical and Materials Engineering Department, Middle East Technical University** by,

Prof. Dr. Canan ÖZGEN _____
Dean, Graduate School of **Natural and Applied Sciences**

Prof. Dr. C. Hakan GÜR _____
Head of Department, **Metallurgical and Materials Engineering**

Assist. Prof. Dr. Yunus Eren KALAY _____
Supervisor, **Metallurgical and Materials Eng. Dept., METU**

Examining Committee Members:

Prof. Dr. Tayfur ÖZTÜRK _____
Metallurgical and Materials Eng. Dept., METU

Assist. Prof. Dr. Yunus Eren KALAY _____
Metallurgical and Materials Eng. Dept., METU

Assist. Prof. Dr. Yener KURU _____
Metallurgical and Materials Eng. Dept., METU

Prof. Dr. Kadri AYDINOL _____
Metallurgical and Materials Eng. Dept., METU

Assist. Prof. Dr. Caner ŞİMŞİR _____
Manufacturing Eng. Dept., ATILIM UNIVERSITY

Date: 11.07.2013

I hereby declare that all information in this document has been obtained and presented in accordance with academic rules and ethical conduct. I also declare that, as required by these rules and conduct, I have fully cited and referenced all material and results that are not original to this work.

Name, Last Name: Can YILDIRIM
Signature :

ABSTRACT

STRUCTURAL AND DYNAMICAL EVOLUTION OF NANOCRYSTALS

Yıldırım, Can

M. Sc., Department of Metallurgical and Materials Engineering

Supervisor: Assist. Prof. Dr. Yunus Eren Kalay

July 2013, 93 Pages

Among all metallic glasses, marginal glass-forming alloys exhibit unique devitrification features due to their primary crystallization products having intriguing nucleation number density values up to $10^{24}m^{-3}$. Remarkable materials properties such as high strength, corrosion resistance and appealing magnetic properties along with the inconsistency of classical nucleation theory predictions with the experimentally observed number density of nanocrystals have recently attracted much of an attention. A full agreement as to how this abnormal nucleation event occurs is still lacking. The present work consists of investigation of amorphous state and devitrification behavior of Al-Tb system using advanced characterization techniques such as synchrotron X-rays and electron beam techniques. Two different amorphization precursors were used to emphasize the effect of topological ordering on devitrification behavior as well as understanding the nucleation mechanism. Samples were prepared using melt-spinning and magnetron sputtering techniques. In-situ XRD experiments showed difference in phase selection hierarchy between ribbons and films. DSC was used to furnish a description regarding the growth of fcc-Al nanocrystals embedded in amorphous matrix using isothermal and isochronal interpretation methods. Unlike melt-spun ribbons, a phase separation was observed in sputtered films. This is attributed to the difference in amorphous solid states in such a way that Al like MRO is decreased in sputtering processes according to XRD and FEM analyses. Approximately three orders of magnitude higher nucleation number density and smaller sized fcc-Al was observed for sputtered films in HRTEM results. A growth model supported by compositional analysis carried out in S/TEM was implemented.

Keywords: nanocrystallization, synchrotron X-ray, electron microscopy, isochronal heating, phase selection.

ÖZ

NANOKRİSTALLERİN YAPISAL VE DİNAMİK GELİŞİMİ

Yıldırım, Can

Yüksek Lisans, Metalurji ve Malzeme Mühendisliği Bölümü

Tez Yöneticisi: Yrd. Doç. Dr. Yunus Eren KALAY

Temmuz 2013, 93 Sayfa

Tüm metalik camlar içinde, marjinal camsı metal alaşımları $10^{24}m^{-3}$ oranlarına ulaşan yüksek sayısal çekirdek yoğunluğuna sahip birincil kristallenme ürünleri nedeniyle özgün devitrifikasyon özelliği göstermektedir. Bu sistemler yüksek mukavement, korozyon dayancı ve üstün manyetik özellikler gibi dikkate değer malzeme özelliklerinin yanı sıra deneysel olarak gözlemlenen sayısal çekirdek yoğunluğunun klasik çekirdeklenme teorisiyle olan tutarsızlığından ötürü oldukça ilgi çekmektedir. Bu anormal çekirdeklenmenin nasıl gerçekleştiğine dair henüz tam bir uzlaşma sağlanamamıştır. Bu çalışma Al-Tb sistemindeki amorf halin ve devitrifikasyonun sinkrotron X-ışınları ve elektron demeti teknikleri gibi ileri karakterizasyon yöntemleriyle incelenmesini kapsamaktadır. İki farklı amorf öncül kullanılarak topolojik düzenin devitrifikasyon ve çekirdeklenme mekanizması üzerine etkileri araştırılmıştır. Numuneler eriyik savurma ve püskürtümlü kaplama yöntemleriyle hazırlanmıştır. Yerinde XRD deneyleri şerit ve film numuneler için farklı faz seçimi hiyerarşisi göstermiştir. Amorf matrise gömülü fcc-Al nanokristallerinin büyümeleriyle ilgili bir tanımlama getirebilmek için DSC vasıtasıyla izotermal ve izokronal yöntemler kullanılmıştır. Şerit numunelerin aksine film numunelerde bir faz ayrışımı gözlenmiştir. XRD ve FEM sonuclarına göre bu durumun amorf haldeki Al benzeri orta-erimli düzen yapılarının püskürtme yönteminden kaynaklanan azalması nedeniyle oluşan farklılıklardan ileri geldiği öngörülmektedir. HRTEM sonuçlarında film numuneler için yaklaşık bin kat daha fazla ve daha küçük boyutlarda fcc-Al nanokristali oluştuğu gözlenmiştir. S/TEM de yapılan kompozisyon analizleriyle desteklenmiş bir büyüme modeli uygulanmıştır.

Anahtar kelimeler: nanokristalleşme, sinkrotron X-ışınları,elektron mikroskobu, izokronal ısıtma, faz seçimi.

To My Precious Family…

ACKNOWLEDGEMENTS

Work at METU was financially supported by BAP1 under the contact number of BAP-07-02-2012-101. Furthermore I would like to acknowledge with much appreciation the crucial role of International Center for Theoretical Physics (ICTP) and Jasper Rikkert Plaisier, the MCX beamline scientist at Elettra Synchrotron Facility in Trieste, Italy for the indispensible contributions to this thesis. I would also like to express my appreciations to Dr. Paul Voyles for his fabulous efforts in FEM experiments and Dr. Matthew Kramer for specimen preparation.

I am indebted to my advisor Assist. Prof. Dr. Y. Eren Kalay in the first place for his guidance all the way from the beginning to the end. I count myself quite lucky to had such an advisor who involves in each step of the research patiently and willingly.

It was a blessing to have such helpful, sincere and solidary lab-mates through the completion of this work. In this respect, I would like to thank Tuba Demirtaş for her incredible support at any time. Moreover I owe my gratitude to Ayşe Merve Genç, Serkan Yılmaz and Güher Kotan especially for their contributions to TEM experiments and all the other favors as well. I have to mention Anıl Kantarcıoğlu, Şermin Özlem Turhan, Mertcan Başkan, Mert Övün and Evren Tan for their aids at any level and especially Mustafacan Kutsal for his assistance in synchrotron experiments.

I should mention my dear friend Emre Mülazımoğlu separately because we had more or less the same motivation, feelings, the same ups downs throughout the thesis and our ways had already been crossed together prior to the progress of this work. Thus I would like to express my wholehearted and deepest appreciations to him for everything he did for me.

It is with immense gratitude that I acknowledge the support, compassion and patience of Noora Tuovinen even at the hardest times. I also appreciate Guthrie, Gonzales and Layne for their outstanding compositions that kept me company through writing of the thesis. I owe my gratitude for my friend Dénes for helping me at the final correction stage of this thesis

Last but not least, I have to say that this thesis would not have been in the way I wanted unless I had my parents and the rest of my whole family by my side, keeping their support by all means and believing in me through this work as they have been doing since I was born.

TABLE OF CONTENTS

LIST OF TABLES

TABLES

LIST OF FIGURES

FIGURES

NOMENCLATURE

APT: Atom Probe Tomography

BF: Bright-field

BMG: Bulk Metallic Glass

CCD: Charge Coupled Device

CN: Coordination Number

DSC: Differential Scanning Calorimetry

EXAFS: X-ray Absorption Fine Structure

FCC: Face Centered Cubic

FEM: Fluctuation Electron Microscopy

FFT: Fast Fourier Transform

HEXRD: High Energy Synchrotron X-ray Diffraction

HRTEM: High Resolution Transmission Electron Microscopy

JMA: Johnson-Mehl-Avrami

LRO: Long Range Order

MD: Molecular Dynamics

MGF: Marginal Glass Former

MRO: Medium Range Order

MUCAT: Midwest Universities Collaborative Access Team

NIST: National Institute of Science and Technology

PDF: Pair Distribution Function

RDF: Radial Distribution Function

RE: Rare-earth Elements

RMC: Reverse Monte Carlo

S(Q): Structure Factor Function

SAED: Selected Area Electron Diffraction

SAXS: Small Angle X-ray Scattering

SANS: Small Angle Neutron Scattering

SEM: Scanning Electron Microscopy

SRO: Short Range Order

S/TEM: Scanning Transmission Electron Microscopy

TEM: Transmission Electron Microscopy

TM: Transition Metal

TTT: Time Temperature Transformation

XANES: X-ray Absorption Near Edge Structure

XRD: X-ray Diffraction

VP: Voronoi Polyhedra

WAXS: Wide Angle X-ray Scattering

CHAPTER 1

INTRODUCTION

1.1. Amorphous Materials

Amorphous materials possess a wide range of application areas that extend from conventional glasses that have been used for centuries to optoelectronics which is one of the most promising research areas of the last couple of decades. Emulsions, different types of polymers, semiconductors (i.e. silicon), some of the thin film lubricants, and metallic glasses can be given as examples of different kinds of amorphous materials. It might seem difficult to incorporate a common point out of these diverse systems, yet the answer relies on their atomic structure.

In a crystalline material, atoms are arranged in three dimensional lattice with translation symmetry in which a unit structure that contains all symmetry elements for a particular system repeats itself throughout the material in a periodic manner leading to a long range order. Thus in a perfect crystal, for any given atom in the system, the number, position and the type of neighboring atoms are identical in other repeating units. However, this is unlikely to be said for an amorphous material in which the atoms are arranged in a rather random manner as far as a long range order is concerned. Instead, a short range order consisting of few angstrom length scales is observed in a typical amorphous material.

1.2. Metallic Glasses

Among amorphous materials, metallic glasses that attracted the interest of many researchers in second half of the last century hold a special place because of their unique properties such as high mechanical strength and hardness [1], large elastic limits along with good wear resistance, remarkable thermal stabilities [2], improved soft magnetic properties and high corrosion resistance. Metallic glasses owe their appealing properties to the nature of the atomic arrangement of their disordered structure. Since metallic glasses lack any long range order and only possess a local chemical configuration and topological ordering, it is evident that the material properties are altered dramatically compared to that of a crystalline material. Therefore a variety of application areas are in the grasp of the reach of metallic glasses. Figure 1.1 shows representative schematics for an ordered crystal and disordered amorphous structures.

Duwez et al. observed the first metallic glass in 1960 in Au-Si alloy system produced by splat quenching of the liquid alloy to obtain at a very high cooling rate the order of 10^6 K/s

[3]. This discovery was followed by many studies on numbers of different alloy systems to yield new metallic glasses. A few years later, ternary disordered metallic alloys in Pd-Si-X system where (X: Cu, Ag or Au) were produced in spherical shapes by Chen and Turnbull [4]. Moreover, Turnbull was able to obtain Pd-Ni-P alloys with 5 mm in thickness in the beginning of 1980s. In 1984, the first bulk metallic glass (BMG) was produced with a final casting thickness up to 1 cm in Pd-Ni-P system with a boron oxide flux by the same group [5]. The first Al-based metallic glasses were recognized in early 1980s by Inoe et al [6]. Upon the discovery of very high glass forming ability (GFA) of La-Al-Ni and La-Al-Cu alloys proposed by Inoue et al. [7] many different compositions of ternary and quaternary metallic glass systems were developed in the following years.

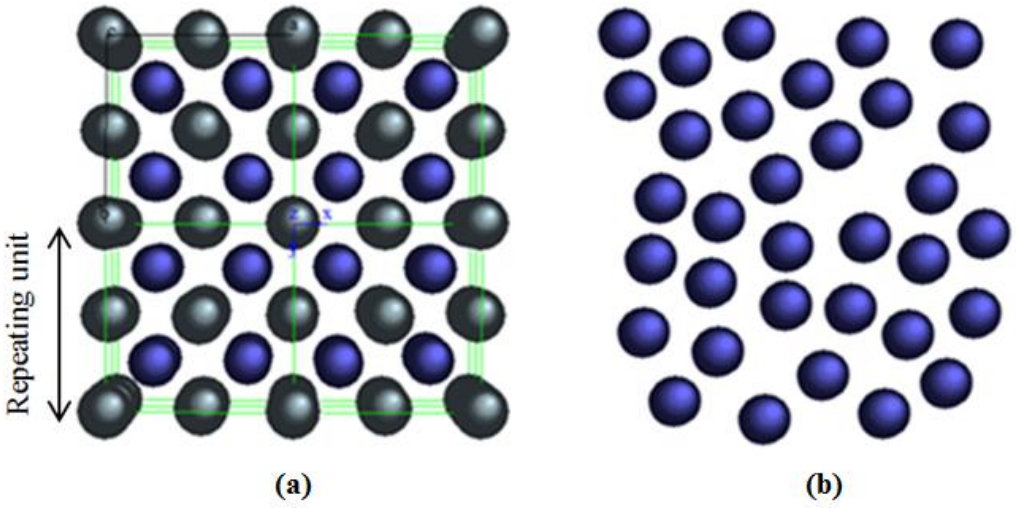

Figure 1.1 Schematics of (a) crystalline and (b) amorphous structures.

Vitreloy 1 ($Zr_{41.2}Ti_{13.8}Cu_{12.5}Ni_{10}Be_{22.5}$), one of the most extensively studied alloy system, was discovered by Peker and Johnson in 1993 [8]. The explicit glass transition and high thermal stability of Vitreloy led scientists to thoroughly investigate this system. In 1996 Vitreloy was produced with a cooling rate of ~ 1 K/s [6] and held the title to be the first metallic glass that was used in an application for the first time in 1998 [9]. More recent works were mostly based on altering the expensive elements such as Pt and Au to cheaper elements like Fe, Ti, Ni, Cu, Zr, and Al. Furthermore a fair amount of effort has been spent for the last two decades for binary metallic glasses. It was shown that small addition of a third element to binary alloys changes the local order in such a way that glass forming ability is increased [10].

Figure 1.2 shows the change in critical casting thickness with respect to years starting from the discovery of metallic glasses. Metallic glasses, recognized more than half a century ago, can now be readily found in many engineering applications from soft magnets to biomedical

implant parts, sports goods to nuclear waste disposal. Demand of better material properties due to development engineering applications has been pushing the scientists to seek even more sophisticated metallic glasses by a number of different respects. Materials with higher strength to weight ratio, better corrosion resistance, higher elasticity, narrower hysteresis loop for magnetic components hold the potential to pertain to future applications. In this perspective, metallic glasses harbor a great deal of importance due to their atomic structure. Defects persisting within crystalline materials disrupt the critical properties whereas the unique disordered nature of metallic glasses assures a homogenous structure in a larger scale. Understanding the fundamentals of supercooled liquid state, glass transition, glass forming ability, thermal stability and devitrification behavior of the metallic glasses which remains still not to be fully understood are of special importance for the development of new alloy systems with remarkable properties.

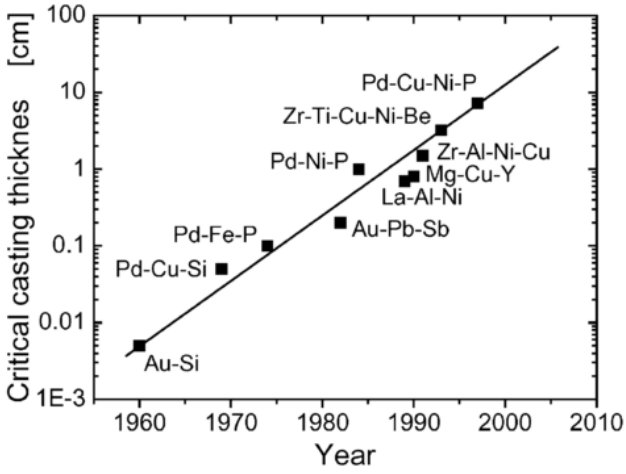

Figure 1.2 Change in critical casting thickness with respect to years. Adopted from [11].

1.3. Origin of Glasses from Liquid State Precursor

Even though amorphous solids which are said to be in glassy state (non-crystalline) show pretty similar structure to that of liquids, apart from the behavior of liquids they do not flow as liquids do. Instead they become non-flowing rigid bodies due to increased viscosity upon transformation to the glass transition. Albeit the fact that there are many different indications for glass transition in literature, the most widely accepted approach for observation of glass transition is to elaborate the change of viscosity upon solidification. A supercooled liquid has to have a viscosity value on the order of 10^{12} Pa s to turn in to a glass [12]. Upon cooling from liquid state, the raised value of viscosity limits the atomic diffusion which in turn causes a diminution in the attachment frequency of atoms to accommodate the critical nuclei size and eventually suppression of crystallization as viscosity continues to increase leading

to glass formation. Figure 1.3 shows the change in viscosity with respect to temperature indicating crystallization and vitrification upon solidification.

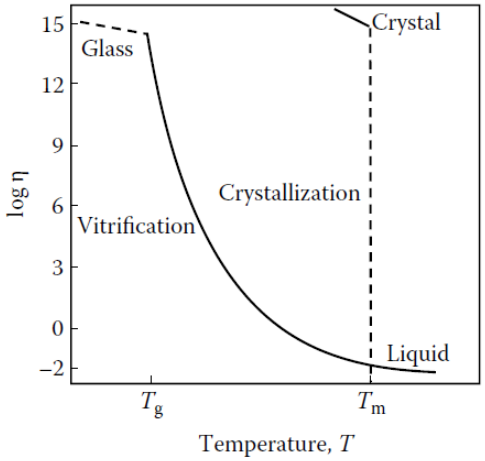

Figure 1.3 Change in viscosity with temperature. Adopted from [13].

1.4. Thermodynamic and Kinetic Aspects of Glass Formation

The stability of a system is dictated by the Gibbs free energy under given conditions where temperature and pressure are kept constant as the equation follows;

$$G = H - TS \qquad \text{Equation 1.1}$$

where H is enthalpy T is temperature and S is the entropy of the system. In this respect phase stabilities can be understood according to the dominating terms which can be either enthalpy or entropy. For example, at low temperatures metal atoms stick together with certain interatomic distances depending mostly on the crystal structure. Thus the enthalpy of the system is very low leading to a minimum Gibbs free energy which in turn suggests the stable phase is the crystalline phase under those particular circumstances. Yet at higher temperature due to the increased atomic vibration frequency the increase in entropy leads to the decrease in Gibbs free energy dictating the stable system to be liquid. Therefore as this simple example shows, the minimum Gibbs free energy criterion can also be applied for metallic glasses for a particular phase to be stable under given circumstances.

Figure 1.4 reveals the Gibbs free energy versus composition diagram for a hypothetical binary system having two solid phases and a liquid phase at equilibrium. The tangent lines drown from the minimum free energy values of corresponding phases suggest that the phase stability region of any composition lying between the range. Beyond the range dictated by

the tangent line single phase regions are observed due to the fact that either liquidus or α curves yield to lower energies thus in turn only one phase is thermodynamically stable.

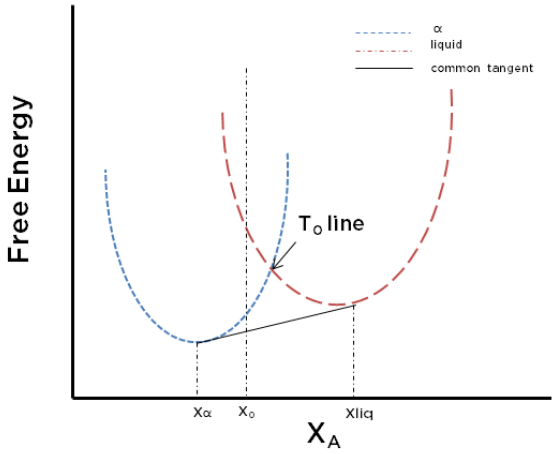

Figure 1.4 Free energy versus composition diagram for a hypothetical system.

However, under non-equilibrium conditions such as rapid solidification, the system may not have enough time to decompose into two phase by diffusion in order to have the stable phase. Instead for such cooling rates the liquid curve may be more stable due to the fact that diffusion is not allowed and the minimum free energy value still possessed by the liquidus curve depending on the structure of the solid phases. To be more specific, the lever rule that applies for lower free energy at X_0 composition will not be feasible since the liquidus curve will be having a lesser energy compared the composition configuration dictated by level rule. Figure 1.5 shows the phase selection hierarchy under non-equilibrium cooling conditions depending on the crystal structure and mutual solubility of lower temperature phases. Upon non-equilibrium cooling conditions intermediate phases might be bypassed and the structural resemblance of the solid phases may affect glass formation in such a way that the T_0 lines may not intersect upon cooling if the crystal structures of lower temperature phases are diverse along with poor mutual solubility.

Although liquid to glass transformation is a matter of thermodynamics that suggest non-equilibrium cooling to observe glass transition, it is the kinetic slowdown which causes atoms to teeter to make the necessary arrangements for crystallization. The decrease in mobility of atoms due to the increased viscosity indicates rather higher time scales for crystalline phase transformation to occur at relatively lower temperatures.

When a melt cools down, the specific volume continues to shrink even below the normal melting point of the liquid. It is this undercooling that gives the energy that is required to

overcome the surface energy term for crystal nuclei to form. Eventually at some point a nuclei forms and the free energy of the system starts to decrease. It is thus followed by the discontinuous change of specific volume when crystallization occurs. However liquid to glass transformation is somewhat different than liquid to crystal solid transformation. As it is mentioned earlier, the continuous change of volume keeps decreasing until viscosity becomes so high that the undercooled liquid acts like a solid in physical nature. This form change does depend on the cooling rate as well as the viscosity of liquid.

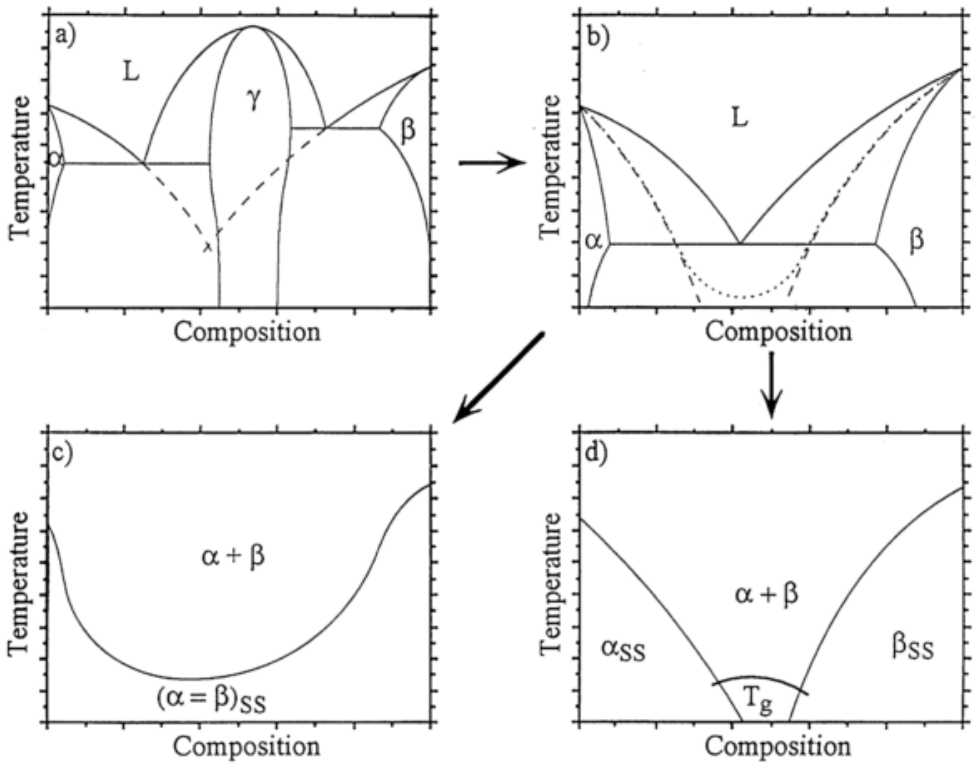

Figure 1.5 Phase selection hierarchy for a hypothetical system under non-equilibrium conditions (a) equilibrium phase diagram (b) non-equilibrium phase diagram (c) condition where primary phases have similar structures and solubility (d) condition where glass formation is favored. Adopted from [14].

In Figure 1.6 the change in specific volume is shown with respect to temperature. Upon cooling down from the melt in non-equilibrium conditions, glass formation occurs as the specific volume of the system follows the line of liquid under circumstances where the cooling rate is high enough to suppress crystallization.

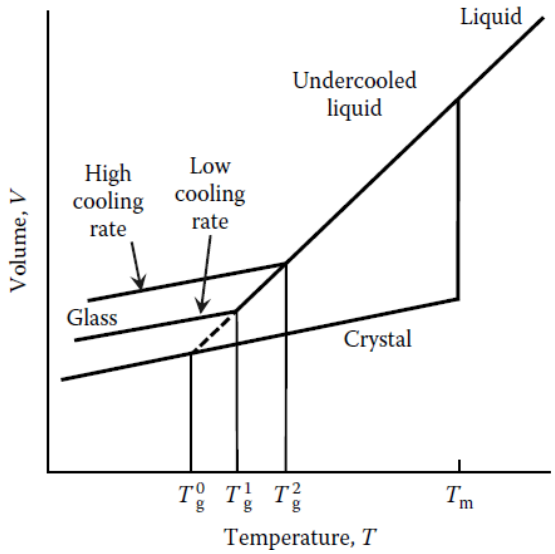

Figure 1.6 Specific volume change with temperature and the effect of cooling rate on glass transition temperature. Adopted from [13].

Upon amorphization, a liquid can be classified as "strong" or "fragile" depending on its behavior as to how the viscosity changes with decreasing temperature. The well-known equation of Vogel-Fulcher-Tammann (VFT) shows the relationship between liquid viscosity as a function of temperature:

$$\eta = \eta_0 \, exp \, [D * T_0 / (T - T_0)] \qquad \text{Equation 1.2}$$

where T is temperature, T_0 is the VFT temperature which is described as an ideal glass transition temperature η_0 and D* is a constant depending on the material [15]. Network forming melts such as SiO_2 whose viscosity follows an Arrhenius decrease with temperature and D* is higher than 20 [11] are identified as strong liquids. This kinetic description provides a solid understanding for a liquid to be a glass former. One of the most essential parameter for indicating the glass forming ability of a liquid is expressed by the reduced glass transition temperature (T_{rg}) which was pointed out by Turnbull as the ratio of the glass transition temperature to the liquidus temperature [16]. He proposed the reduced glass transition temperature to be the VFT temperature ending up in a ratio of $T_{rg} \geq 2/3$ [17]. Since the rate of crystal nucleation and growth is decreased with lowering reduced glass transition temperature, it was shown that strong liquids are having higher glass forming ability compared to fragile liquids. Some strong and fragile liquids are shown in Figure 1.7 along with the heat capacities.

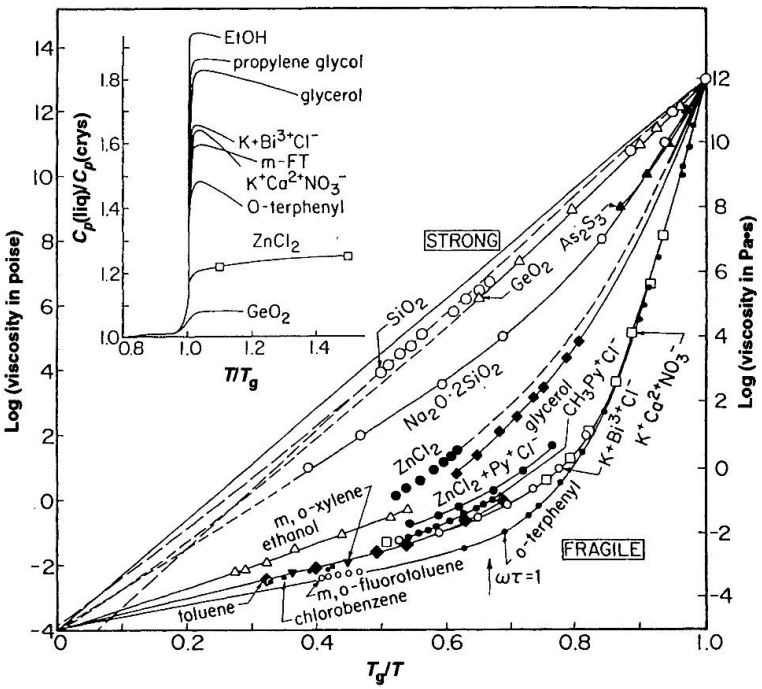

Figure 1.7 Logarithmic viscosity and unitless temperature T_g/T plot showing the strong and fragile liquid behavior. Heat capacity change with temperature is indicated for various strong and fragile liquids. Adopted from [15].

The heat capacity change (ΔC_p) is one of the key thermodynamic indications of the glass transition while viscosity is being the prominent parameter of kinetics of glass formation. The heat capacity of the liquid is higher than that of the competing solid crystals whose driving force is the Gibbs free energy difference (ΔG) of liquid and the solid caused by undercooling. Thus to account the difference in glass formation compared to crystallization the ΔC_p must be involved for the overall ΔG. It has been shown that for materials having high GFA exhibit higher heat capacity in supercooled region and that tend to increase with decreasing temperature [18]. Figure 1.8 exhibits the heat capacities of some supercooled liquids and that of a crystal with changing unitless T/T_{eut} ratio.

Thermodynamics and kinetics of glass transition can be correlated according to the Adam-Gibbs (AG) equation [19];

$$\tau(T) \sim exp\,[C/(TS_c(T))] \qquad \text{Equation 1.3}$$

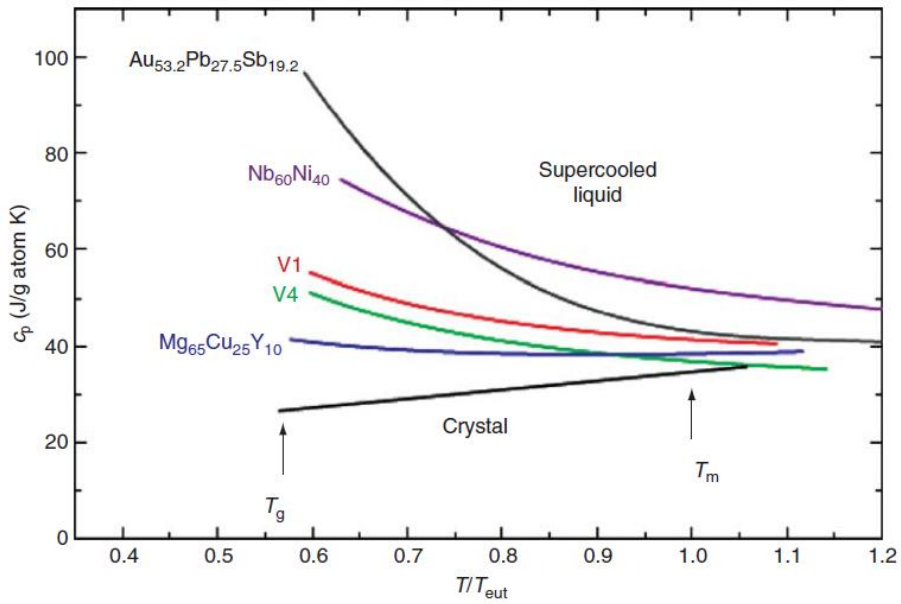

Figure 1.8 Heat capacity of various metallic glasses with respect to unitless$T/T_{eutectic}$. Adopted from [18].

where τ is the relaxation time as a function of temperature, T is temperature, C is a material constant pertaining to the amount of energy needed for the arrangement and S_c is the molar configurational entropy. The AG equation provides a connection between kinetic slowdown due to increased viscosity and thermodynamic terms to identify the glass transition such as entropy and chemical potential difference of the states. It has been shown that for fragile liquids, AG theory agrees well with the cooling behavior near T_g to describe the effect of temperature on relaxation time [20]. Yet this worthy achievement for fragile systems cannot be attained for strong liquid systems mainly due to the short range bond ordering in strong liquids [21].

The AG equation including thermodynamic parameters such as entropy and relating the relaxation time of a particular system with respect to temperature can be considered identical to VFT equation by correlating the viscosity and the relaxation time [17];

$$\eta = \eta_0 \, exp\,[\, C \,/\, (TS_c(T))\,] \qquad \text{Equation 1.4}$$

Figure 1.9 shows the entropy change of a system with respect to temperature. As the melt cools down with a sufficiently high cooling rate so that no crystal structure can form, the entropy crisis, that is the entropy of the system being negative if the liquidus entropy curve is followed with decreasing temperature, occurs. Therefore after T_g, entropy follows a constant value to overcome this crisis. This is the formation of solid amorphous in physical terms.

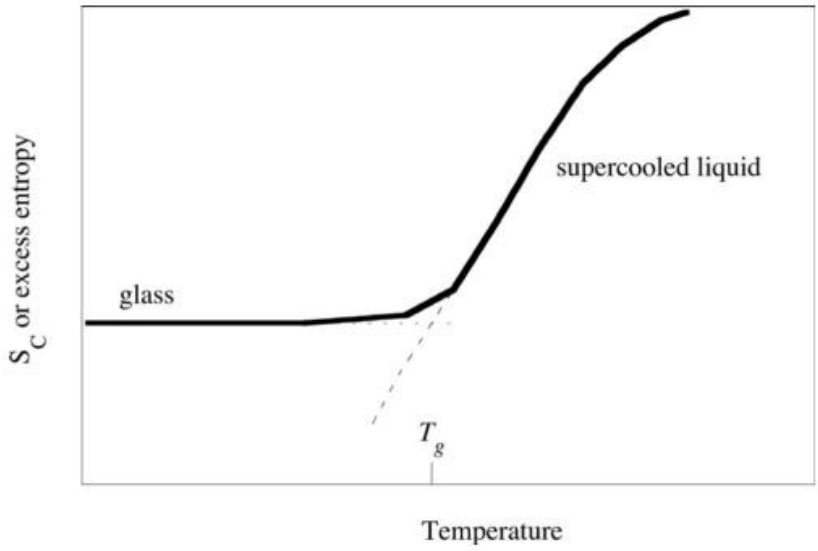

Figure 1.9 Schematic plot of entropy change with temperature. Adopted from [20].

1.5. Glass Forming Ability

According to the equation 1.3, as viscosity increases so does the relaxation time. This means at relatively lower temperatures the required time to fulfill the necessary atomic rearrangement for the competing crystal phase is much higher which can be explained in a time-temperature-transformation (TTT) graph. As it was stated earlier the GFA of a material is basically its ability to transform into glass in relatively slower cooling rates. Thus for a fragile melt, the critical cooling rate (CCR) is higher by the orders of magnitude compared to that of strong liquids. CCR can be described as the lowest rate of solidification at which a glass can be formed. Therefore GFA holds a great importance to adjust CCR thus the sizes of the metallic glass products.

It was previously mentioned that glass forming ability can be increased by micro-alloying yet it is an issue of more interest to be paid. An extensive amount of effort has been paid to understand GFA of metallic glasses. Inoue proposed some empirical approach that has been widely accepted for development of new alloy systems. He suggested three important empirical rules to point out the necessities of a particular system to be a glass forming alloy. According to these rules, the more negative enthalpy of mixing, minimum atomic size difference of 12 % and minimum three constituents are the musts of a system to be a glass former [22].

Following this by patterns, Greer has offered the “confusion principle” in regard to glass forming abilities of metallic glasses [23]. The principle simply states that increasing the number of the species in an alloy confuses the structure in such a way that alloy struggles to find itself in a stable crystalline form due to the increased possibility of different resultant crystal structures.

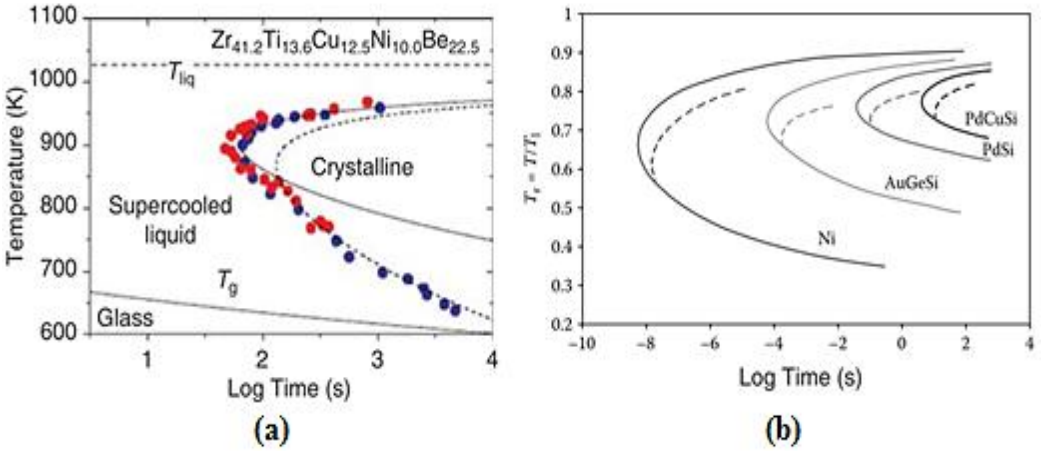

Figure 1.10 (a) TTT curves for Vitreloy 1 [18] and for pure nickel and $Au_{78}Ge_{14}Si_8$, $Pd_{82}Si_{18}$ and Pd_{78} Cu_6 Si_{16} alloys (b). Adopted from [13].

1.6. Amorphous Structure

The structural origin of the metallic glasses also lightens the GFA issue. The short range in the metallic melts does aid the system to be a glass former due to the atomic packing. As viscosity of melts is of great importance for a liquid to be a glass former, the packing density of atoms in liquid structure inherits GFA. Although face centered cubic and hexagonal structures are densely packed structures, due to their translational symmetry, liquids having these structures in short range are prone to crystallize. However icosahedral short range ordering are shown to be the essential topological short range order that is responsible for increasing glass forming ability of a liquid because of the lack of translational symmetry [24]. Different models for packing in metallic liquids that are acquainted with glass forming ability have been proposed.

Among these models Miracle recently showed a short to medium range packing order based on solute centered model that extends only a few nanometers due to the strains which arise from mismatch [25]. Examples of icosahedral short range and medium range packing order are shown in Figure 1.11.

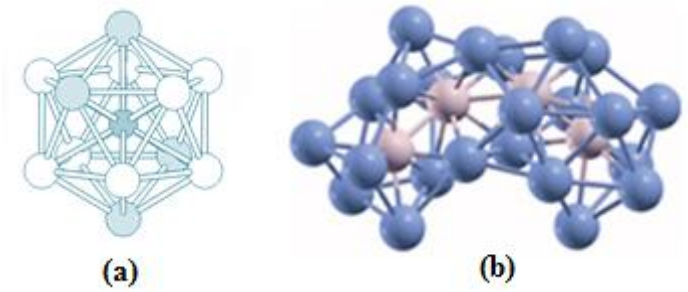

Figure 1.11 (a) Icosahedral short range order and (b) medium range order. Adopted from [26] and [27].

1.7. Synthesis of Metallic Glasses

Metallic glasses can be classified in two groups according to their glass forming abilities, namely as bulk metallic glasses and marginal glass formers. The main practical difference of these diverse kinds is the critical cooling rates. BMG alloys can be vitrified with cooling rates around 1-10^2 K/s whereas marginal glass formers require a cooling rate of ~10^6 K/s for most systems. In this thesis the emphasis will be given on marginal glass forming alloys.

Up to this point, glass formation through solidification has been elaborated. However, in principle any process that prevents the long range atomic distribution by any respect may form glasses. Strictly speaking, due to the thermodynamic constraints of undercooled liquid, amorphous solid is considered as a metastable state, yet one can still deal with the entropy of supercooled region, defining excess or configurational entropy to describe the state of the matter. Thus altering the equilibrium state to a sufficient extend of disorder will end up to amorphous structure. There have been many different methods that have been developed throughout the years since the first splat-quenched metallic glass. In this section, the methods that are used commonly to produce metallic glasses will be discussed.

1.7.1 Rapid Solidification Methods

The thermodynamic and kinetic aspects of liquid to glass process have been given to some extend in earlier sections. The main feature of rapid solidification techniques is basically to cool the material from liquid form to solid state in such a way that crystallization is suppressed. Therefore to achieve glass formation by solidification, cooling rate must be of critical importance. In this regard, metal-metal contact cooling techniques turn out to be the best choice as far as heat transfer capabilities are concerned. The invention of a process called melt-spinning was one of the milestones in metallic glass history [28]. The method consists of ejecting the liquid alloy onto a rotating copper wheel with tangential speeds of a few tens of m/s. By this manner, homogenous amorphous solid can be produced in ribbon

shape with typical thickness values of 20-80 micrometers. This process can be carried out under vacuum or argon atmosphere to avoid oxidation. After the discovery of melt-spinning method, number of different metallic glass compositions were produced and studied extensively since the method is simple and commercially available. Figure 1.12 shows a copper block melt spinner along with its schematic representation.

Other techniques of rapid solidification methods can be listed as;

- Flux melting technique [13]
- Casting methods (chill, mold, injection, die etc.) [13]
- Gas atomization [13,39]

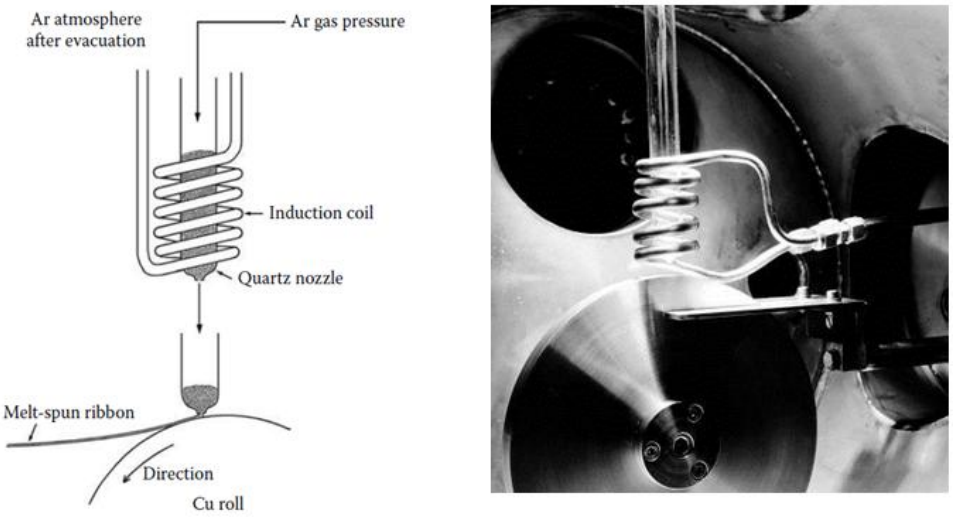

Figure 1.12 Schematic representation of melt-spinning technique (a) and the melt-spinning unit used in this thesis study (b). Adopted from [13] and [29].

1.7.2 Vapor State Methods

Another rapid quenching method can be given as reaching to the glassy state from vapor phase. Many of the thin film production have been conducted with chemical vapor deposition, electron beam deposition and sputtering ending up variety of microstructure including, fully crystal, partially crystal and amorphous [13].

Among these methods magnetron sputtering is one of the most useful technique to produce amorphous metals. Magnetron sputtering can be considered as a type of physical vapor

deposition in which the sputter metal is bombarded with ions to eject onto a metal target under an inert gas atmosphere. The metal target can be cooled by cryogenic means such as liquid nitrogen to obtain higher cooling rates on the order of 10^9 K/s resulting in a metallic glass. By this manner a thin films having thicknesses of micrometer size can be achieved. The major drawback of sputtering technique is the elusiveness of the nominal composition adjustment. Since even a tiny change in the composition of an alloy may affect GFA dramatically, partial or even full crystallization may be observed.

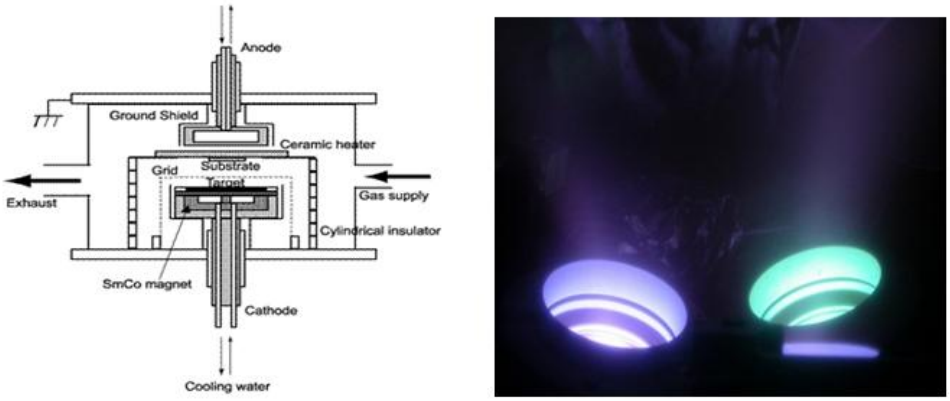

Figure 1.13 Schematic of magnetron sputtering technique. Adopted from [29] and [30].

Another disadvantage of this method is relatively slower deposition rates compared to other vapor deposition techniques. Nonetheless as far as amorphization ability is concerned, this method provides a great deal of reliance. A liquid nitrogen cooled DC magnetron sputter with a schematic representation of the components can be seen in Figure 1.13.

The emphasis was given mostly to melt-spinning and magnetron sputtering techniques among the other rapid quenching methods since they were used to obtain Al-based amorphous alloys in the scope of this work. The following methods that are given below are to provide a spectrum of production techniques for amorphous metals. The major differences of melt-spinning and magnetron sputtering are listed in Table 1.1.

Table 1.1 Different features of melt-spinning and magnetron sputtering techniques.

Method	Cooling Rate	Initial State	Typical Final Thickness	Composition
Melt-spinning	10^4-10^6 K/s	Liquid	20-80 μm	Easy to adjust
Magnetron Sputtering	10^9-10^{10} K/s	Vapor	5-10 μm	Hard to adjust

1.7.3 Solid State Methods

When solid state amorphization methods are considered, the most widely used way technique is the deformation induced mechanical amorphization. Mechanical rolling and milling can be given as the examples of this category. Rolling and milling has a common point as to how amorphization occurs in principle. In these two methods, the extensive deformation causes highly concentrated defect density and free volume within the system. Thus the free energy of the system then becomes higher compared to that of a possible amorphous phase which leads to break down in atomic arrangements in crystal lattice leading to an amorphous solid. It has been shown for some systems that a few tens of rolling and folding passes causes fully amorphous structure [31]. Figure 1.14 shows the schematic rolling ad folding sequence for solid state deformation induced amorphization. One other frequently used solid state amorphization technique is mechanical alloying. In this method, amorphous solid is obtain starting from powders and includes continuously cold welding and fracture of these welded particles by milling [32].

Another solid state amorphization technique is called solid state reaction (SSR). The method consists of interdiffusion of supersaturated metal layers connected and heated to temperatures where diffusion would take place for relatively shorter times. The asymmetric diffusion due massive difference in interdiffusivities of species is inherited from the atomic size difference elucidates the formation of an amorphous having a thickness of approximately half a micron. In addition to those methods explained above, amorphization by irradiation [33], hydrogen [34] and pressure induced amorphization [35] can be given as examples of techniques to produce amorphous metals by solid state methods.

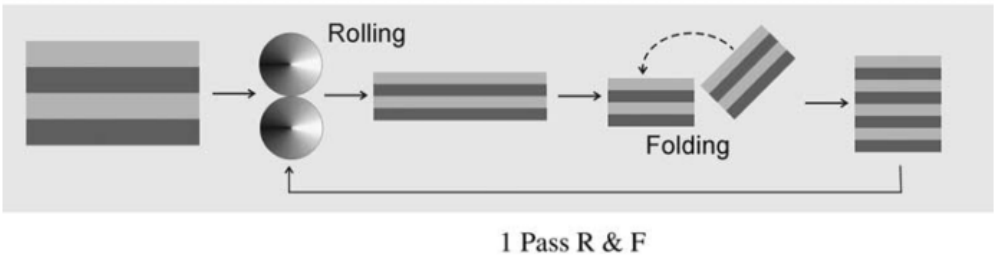

Figure 1.14 Schematic representation of amorphization by cold rolling process. Adopted from [31].

1.8. Structural and Dynamic Characterization of Metallic Glasses

In order to reveal the property-performance-structure relationships in metallic glasses, structural and dynamic characterization of these intriguing systems is of a great deal of importance. For this purpose a wide range of characterization techniques are in use. Some of these techniques are fairly simple but providing very fruitful results for understanding of dynamics and physical properties such as differential scanning calorimetry (DSC) whereas some others are really sophisticated in both engineering and physics respects such as transmission electron microscopy (TEM) and synchrotron light sources. The mystery relies on the uncanny structure of the metallic glasses and has been investigated over decades with these methods and there is still veiled information yet to be discovered.

1.8.1 Differential Scanning Calorimetry

Differential Scanning Calorimetry (DSC) is used to track thermophysical changes in a material with respect to change in temperature. Phase transformations, heat of reactions, activation energies of reactions, physical properties such as heat capacity and melting point can be determined precisely by this simple but powerful technique. Furthermore, important transformation points such as glass transition, crystallization, phase separation which is of vital importance in metallic glass studies can be easily investigated with this technique.

DSC consists of a small heating chamber which can be filled by a protective gas to have an inert atmosphere, such as nitrogen or argon. The chamber has two heating platforms and two pans which can be made of aluminum or copper depending on the experiment is placed on top of these platforms. One of the pans remains empty as a reference and the other one is filled with the sample. Both pans are heated in a constant rate that is ($\Delta T/\Delta t$). It is known that a first order phase transformation can be either exothermic or endothermic, that is heat is released for the former and heat is needed for the latter case, respectively. Therefore upon constant heating any phase transformation occurring in the filled pan will either use heat or release heat. Since the ingredients are different for each pan, the heat flow released is different. Thus the heat flow ($\Delta Q/\Delta t$) is measured in such a way that thermocouples placed

beneath the heaters while the constant heating rate along with the temperature for two pans are maintained the same throughout the experiment.

DSC can detect both first (such as crystallization, oxidation, melting) and second order (such as glass transition, order-disorder transformations) phase transformations. Examples are shown in Figure 1.15. Thermal analysis conducted by DSC can be used to describe the nucleation and growth phases in an amorphous solid. Furthermore there have been many different approaches proposed to interpret energy barriers associated with chemical reactions or phase transformations. These methods will be explained in details in the following chapters.

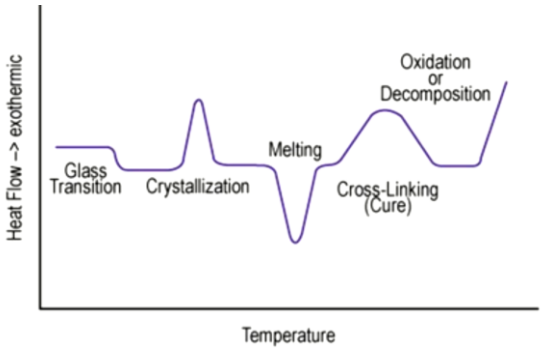

Figure 1.15 A representative DSC curve showing indications for various thermal events. Adopted from [36].

1.8.2 Transmission Electron Microscopy

Transmission electron microscope (TEM) is a very powerful electron beam technique that is frequently used in solid state material science. It is capable of providing resolutions in pico level which makes TEM quite attractive for atomic structure studies. Many studies in metallic glass field have been carried out with TEM investigations in order to observe devitrification of glasses, shape, size and crystallography of evolving phases.

TEM consists of a column that is kept under vacuum in which an electron gun placed at top having a potential difference of a few hundreds of kV. The applied voltage causes electrons to travel through the specimen and the movement of electrons is manipulated with the magnetic field within the column. The electron-specimen interaction leads to different events to take place within the optic rules. One of these can be attributed to diffraction phenomenon is being observable in TEM with a great reciprocal space resolution due to the high voltage applied. The real and reciprocal space information that can be received from the same region of specimen makes TEMs very distinguished among the other electron beam techniques. Moreover with an attached energy dispersive spectrum (EDS) detector, TEM provides elemental analysis for the specimen along with image in high resolution and diffraction with

a great spatial resolution. Figure 1.16 shows a bright-field (BF) image and corresponding selected area electron diffraction (SAED) images of the phases in that particular region investigated in BF.

In contrast to advantages, one drawback of TEM is the specimen preparation step. Since TEM is operated in such a way that the electrons pass through the material, the specimen must be thinned enough (around 100 nm) to provide this prerequisite. Therefore it is relatively tedious to prepare a TEM specimen compared to other electron beam techniques. Specimen preparation for TEM is explained in following chapters.

TEM can be made even more useful via different attachments applied to the microscope such as hot stage which allow heating the specimen to a desired temperature [37] or nanoindenter that performs deformation on the specimen under tensile or compressive loadings [38] within the column to conduct in situ experiments. In these regards, structural changes such as phase transitions, growth of phases and plasticity of materials can be monitored with time resolution depending on the capability of CCD used.

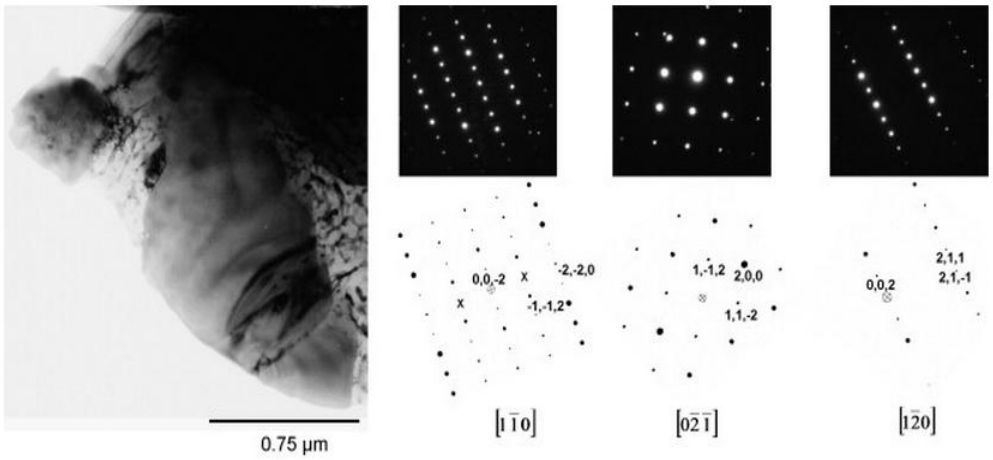

Figure 1.16 Bright-field (BF) and selected area electron diffraction (SAED) images of $Al_{90}Sm_{10}$ system. Adopted from [39].

1.8.3 Fluctuation Electron Microscopy

Fluctuation electron microscopy (FEM) is a combination of imaging and diffraction technique to reveal the medium range order (MRO) structures ranging from 0.5 to 3 nm. It is a relatively recent method to resolve MRO structure compared to other methods explained above [40]. It is used to observe the nanoscale structural fluctuations from many diffraction points and it measures V (*k)* with changing reciprocal space vector (*k*) that is $k = \sin(\theta)/\lambda$, R is being the probe diameter and **r** indicates the position on the specimen.

$$V(k,R) = \frac{\langle I^2(k,R,\boldsymbol{r})\rangle}{\langle I(k,R,\boldsymbol{r})\rangle^2} - 1 \qquad \text{Equation 1.5}$$

In other words, the intensity of scattered electrons is obtained from a few thousands of positions on the specimen and judged depending on the level of disorder in the system. This technique is conducted either in diffraction mode using scanning transmission electron microscope (S/TEM) or in real space mode using dark-field (DF) imaging. Figure 1.17 shows schematic working principles of FEM in both DF and STEM modes.

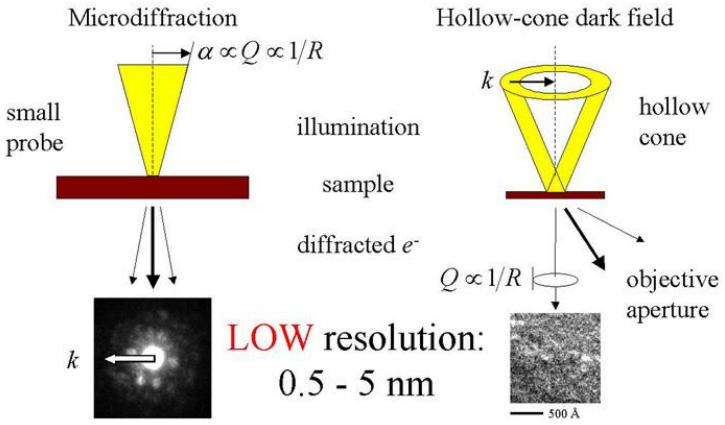

Figure 1.17 Principles of FEM. Adopted from [41].

1.8.4 Synchrotron Light Source

Synchrotron light sources are very sophisticated facilities offering deep investigation opportunities in many different physical, chemical and biological sciences. The radiation that is emitted from electrons or positrons when they change their energy in an accelerator is called synchrotron radiation and the corresponding light source is caused by this radiation by the help of undulators and bending magnets.

As compared to conventional X-ray tubes in laboratories, synchrotron light sources provides a much higher brilliance, that is the number of photons per unit area and time, on the order of 10^{18} compared to conventional X-ray tubes. Therefore high energy X-ray diffraction (HEXRD) experiments can be conducted in a number of in-situ tests in synchrotron light sources. High energy X-rays provide a great spatial resolution in reciprocal space. The tunable energy of accelerated electrons is used by diverse beamlines depending on different purposes not only wide angle X-ray diffraction which can also be done with thousands fold less brightness in conventional X-ray tubes but also sophisticated experiments using other features of synchrotron facilities such as inelastic scattering, X-ray Raman scattering, X-ray

imaging, macromolecular crystallography, multi-wavelength anomalous diffraction, micro-fluorescence imaging.

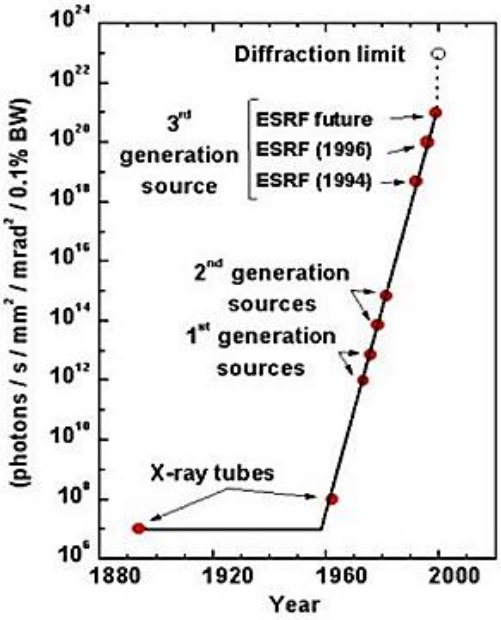

Figure 1.18 Evolution of X-ray brilliance with years. Adopted from [42].

The major drawback of synchrotron radiation is that the facilities are not readily available as in the case of laboratory X-ray tubes and available beamline times cannot be more than couple of times per year for most of the cases since those facilities are used by loads of scientists around the world. Nevertheless these powerful light sources offer very important opportunities for many in-situ or ex-situ experiments that cannot be performed in conventional X-ray tubes. The increase in X-ray brilliance of synchrotron facilities along with the first X-ray tubes that were followed by rotating anode method as can be seen from the Figure 1.18

A major part of this study was conducted at Elettra Synchrotron facility. Detailed information regarding to beamlines and experimental procedures is given in the following chapters. Figure 1.19 shows a schematic representation and a photo of Elettra Synchrotron facility in Trieste, Italy.

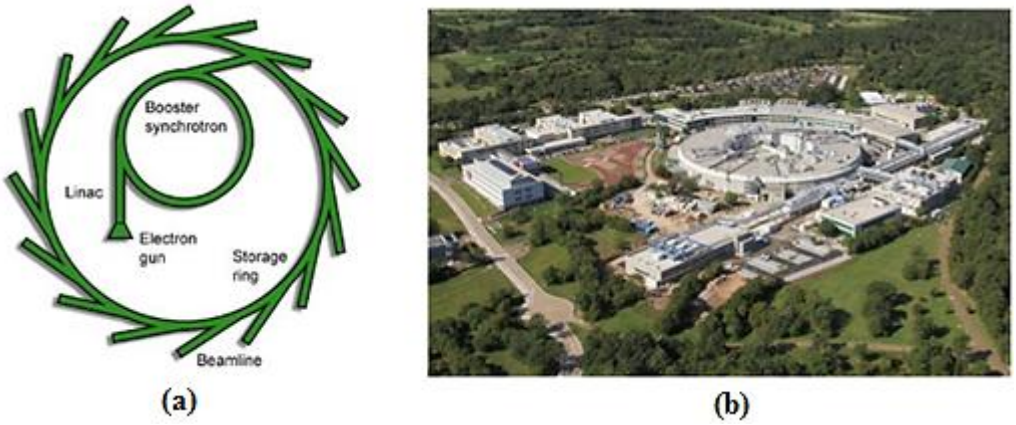

Figure 1.19 (a) Schematic representation of a synchrotron light source (b) Elettra Light Source in Trieste, Italy. Adopted from [43] and [44].

In addition to the methods explained above, there is many other characterization techniques such as neutron scattering, extended X-ray absorption fine structure (EXAFS), X-ray near edge structure (XANES), Scanning electron microscopy (SEM), electron energy loss spectroscopy (EELS), atom probe tomography which are in use by the scientists working in the field of metallic glass and amorphous structure.

1.9. Thesis Organization

The aim of this thesis is to investigate the structural and dynamic evolutions of nanocrystals in aluminum based marginal glass forming alloy system. In this respect, thesis consists of five individual chapters. The first chapter includes the background information to cover up the literature information on history of metallic glasses, the thermodynamic and kinetic aspects of glass formation and major characterization methods revealing the atomic structure and chemistry of metallic glasses. The second chapter focuses on Al-based metallic glasses, particularly on $Al_{90}Tb_{10}$ alloy system. Background information on how Al-based metallic glasses hold their place in metallic glass history is given. The main content of the second chapter includes the investigation of the phase selection hierarchy in melt-spun ribbons and sputtered films with the use of DSC, TEM and synchrotron radiation. The third chapter consists of thermal analysis of primary crystallization in melt-spun ribbons and sputtered films of $Al_{90}Tb_{10}$ alloy. The comparison between ribbons and films were done using the DSC results. From the isothermal and non-isothermal approaches such as Avrami, Kissinger, Ozawa and Matusita methods nucleation and growth behavior of fcc-Al nanocrystals in ribbons and sputtered films are discussed. The fourth chapter is based on isothermal growth behavior of primary crystallization product of the same alloy system. TEM, STEM and a mathematical model are used to describe the growth of fcc-Al nanocrystals in amorphous matrix along with nucleation number density calculations. Thus a comprehensive expression

is given as to how the amorphization precursor affects the nanocrystal growth in Al-RE marginal glass forming systems. The final chapter gives conclusions of the work and possible future direction for the subject of this study.

CHAPTER 2

PHASE SELECTION HIERARCHY IN HIGHLY DRIVEN Al-Tb GLASSY ALLOYS

2.1 Introduction

Al-based marginal glass forming alloys have been much of interest for more than twenty years mainly due to their high potential in light weight structural applications. Investigating controlled devitrification of these alloys with powerful characterization techniques provides great deal of information in regard to design new microstructures for desired engineering application. In this chapter one can find phase selection hierarchy Al-Tb glassy alloys produced by two different amorphization paths, namely as melt-spinning and magnetron sputtering.

2.2 Literature Review

2.2.1 Al-based Metallic Glasses

It has been stated in earlier sections that upon the discovery of metallic glasses, many different glassy alloys have been obtained in numerous composition combinations with various production techniques. Al-based metallic glasses find place among these innovations in early 1980s. The first Al-based metallic glasses were noticed in Al-Fe (or Co)-B alloys having more than 50 at% Al within the glass forming alloy composition [45]. Some other ternary glassy alloys were also proposed in following years. Yet the brittleness of these alloys was the biggest obstacle for further investigation of these systems due to the lack of application possibilities. Nevertheless after a couple of years in the late 1980s, relatively ductile Al-based glassy alloys have been reported by two independent research groups [46, 47]. Ribbons of ternary Al-based glassy alloys were produced by melt-spinning technique and these ribbons can bend up to 180 degrees without fracture. Al-TM-RE and Al-RE (TM: transition metal and RE: rare-earth) alloys of different compositions were reported to have very high strength values, on the order of those of steels, compared to that of conventional Al-based crystalline systems. Therefore a substantial amount of efforts have been given for understanding the promising features of Al-based metallic glasses such as mechanical properties, thermal stability, corrosion resistance and glass forming ability.

Table 2.1 Mechanical properties of various Al-TM-RE alloys. Adopted from [47].

Alloy	Tensile Strength (MPa)	Young's Modulus (GPa)
$Al_{90}Fe_5Ce_5$	940	66
$Al_{87}Fe_{8.7}Gd_{4.3}$	840	53
$Al_{87}Ni_{8.7}Y_{4.3}$	880	50
$Al_{87}Rh_{8.7}Ce_{4.3}$	730	63

2.2.2 Structure and GFA of Al-based Metallic Glasses

It is of great importance to have a fundamental understanding of structure to tailor the properties as well as to produce new alloys. Thermodynamic and kinetic aspects of metallic glasses have been mentioned to some extend in earlier sections along with glass forming ability. In Al-based systems the compositions mostly consist of Al-TM-RE and Al-RE combinations. The first glance to Al-RE type alloys shows contradiction to glass forming criteria in such a way that the alloy is a binary and the system in not "confused" by means possibility of variety of different competing crystalline structures to be formed upon cooling from the liquid. Moreover it is well known that eutectic points are said to be the best compositions to obtain metallic glasses due to the high suppression of liquidus temperature. However that is again not the case for Al-based systems since they can form glasses in off-eutectic compositions. Therefore from these points of views the structure of Al-based metallic glasses becomes more an issue for further investigations. The atomic size difference and negative enthalpy of mixing along with volume mismatch appears to be the decisive parameters for glass formation in Al-based systems. It has been studied extensively for a number of systems by Inoue and the glass formation ranges were reported in Figure 2.1 [48].

Metallic glasses are divided in two groups regarding their solidification behavior affecting the glass forming abilities, namely as bulk metallic glasses and marginal glass formers as it was mentioned earlier. Al-based metallic glasses reach Kauzmann temperature (T_k) faster than bulk metallic glasses which means they are rather fragile systems and classified in marginal glass forming alloys. Fragility of liquids is well described with VFT equation which was explained in chapter one. The derivative of Equation 1.1 with respect to T_g/T yields to value of *m* that is the slope of Angell plot given in Figure 1.4.

$$m = d[ln(\eta)]/d[T_g/T_k] \qquad \text{Equation 2.1}$$

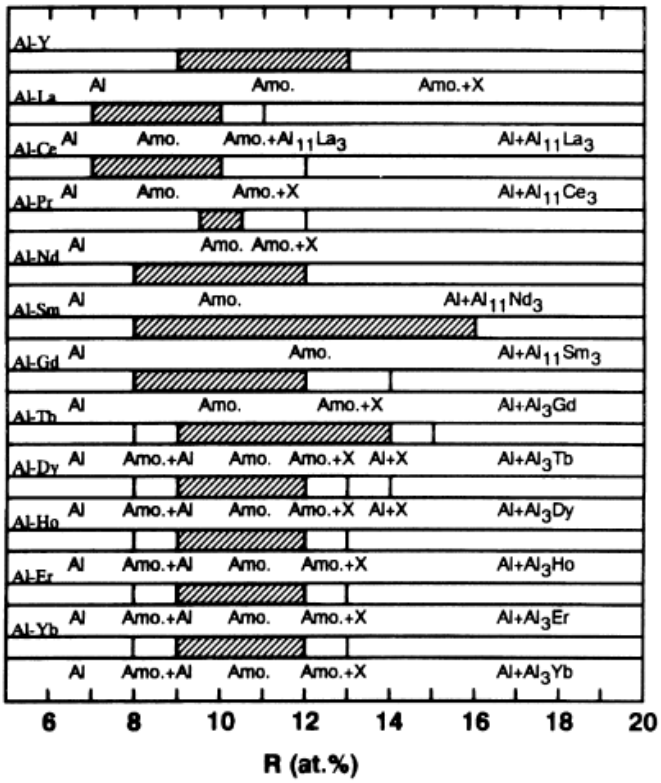

Figure 2.1 Glass forming ranges for some Al-RE. Adopted from [46].

Another comparison can be made to point out the fragility behavior with the ratio of glass transition temperature (T_g) to Kauzmann temperature. The stronger the liquid is the higher the T_g/T_k ratio. Table 2.2 shows the fragility parameters of different glass formers. It can be seen that Al-based metallic glasses have rather high m and low D values. Taking glass transition temperature and liquidus temperatures of these systems into account it is clear that to obtain amorphous structures in Al-based metallic glasses a typical cooling rate of 10^6 K/min is required. Such cooling rates can be reached by melt-spinning and sputtering in most of the studies on these systems.

Table 2.2 Fragility behavior of some glasses. Adopted from [48].

Alloy	***m***	***D***	T_g/T_k
SiO_2	20	100	-
$Mg_{65}Cu_{25}Y_{10}$	45	22.1	1.58
$Pd_{40}Ni_{40}P_{20}$	46	18.1	1.44
$Al_{87}Ni_7Ce_6$	127	5.6	1.15

Conventional X-ray diffraction (XRD) is the most convenient and fruitful method to investigate structure of metallic glasses as far as degree of amorphization and/or crystallization is concerned. A typical XRD pattern of Al-TM-RE and Al-RE type of alloys show one broad halo that is characteristic of amorphous structure. Figure 2.2 shows the XRD pattern of $Al_{87}Ni_7Nd_6$ as an example. The unusual XRD feature in these alloys compared to BMGs can be given as a pre-peak that is observed at lower reciprocal space (*Q*) than the main halo and also a side peak couple of angles higher than the main amorphous halo.

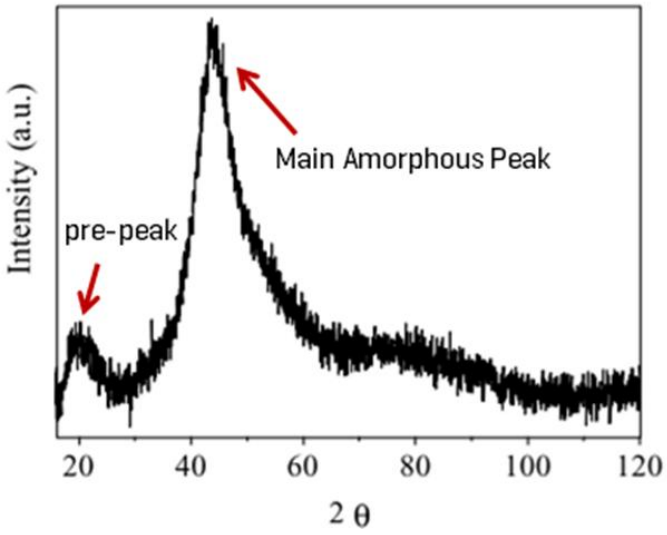

Figure 2.2 XRD pattern of $Al_{87}Ni_7Nd_6$ Adopted from [49].

Figure 2.2 shows the XRD pattern for amorphous $Al_{87}Ni_7Nd_6$ alloy. The topological ordering of RE-RE atoms is thought to give rise to the pre-peak found in this kind of alloys and the compositional dependence of pre-peak intensity has been shown. The RE atoms are surrounded by Al atoms within the alloy. Moreover the pre-peak shifts have been shown in accordance with alloying elements for Al-based metallic glasses. Therefore the origin of pre-peak is attributed to the topological ordering of RE atoms. The side peak that is observed at higher angles than main halo peak was suggested to be due to the quenched-in Al nuclei upon cooling since it overlaps with Al (002) reflection. The reason why Al (111) reflection is not seen in XRD was explained in such a way that main amorphous halo overlaps with Al (111) peak and hides that particular reflection for $Al_{85}Y_xNi_{15-x}$ system [50].

The pre-peak and side peak was also elaborated in another study. High energy X-ray diffraction (HEXRD) by synchrotron radiation was performed to reveal amorphous structure in Al-Tb system. The high range in *Q* space obtained by HEXRD was used to enable reverse Monte Carlo (RMC) simulations in appreciable levels of fit with the absence of radial

distribution function (RDF). It was reported that the strong interactions between Al and Tb atoms gives rise to pre-peak intensity not only in amorphous solid but also in liquid state. As a matter of fact this was attributed to topological ordering in Al-Tb system where Tb atoms are surrounded by Al atoms with a high coordination number [51]. Figure 2.3 shows HEXRD patterns for liquid and amorphous solid of Al-Tb alloy.

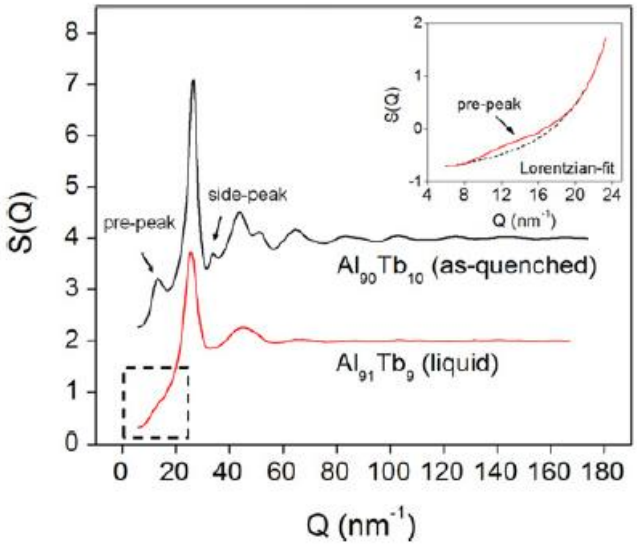

Figure 2.3 HEXRD of Al-Tb alloy in both solid and liquid states. Adopted from [51].

2.2.3 Devitrification of Al-based Metallic Glasses

Controlled crystallization of Al-based metallic glasses is an appealing research field due to the improved grain refinement. Aluminum nanocrystals that evolve by primary crystallization (i.e. the crystallization of a phase having a different composition from that of parent phase), from amorphous matrix with an extraordinarily high number density (on the order of $10^{21\text{-}24}$) along with good coarsening resistance have been attracted much attention. These peculiar nanocrystalline-amorphous systems are reported to yield high strength and high corrosion resistance. Therefore altering the microstructure with controlled devitrification of Al-based metallic glasses is a promising subject.

Differential scanning calorimetry (DSC) is one of the methods that have been widely used to trace the devitrification behavior of metallic glasses. Important parameters to understand thermal stability of metallic glasses such as crystallization onset temperature (T_x), glass transition temperature (T_g), reaction peak temperature (T_p) and heat of reactions can be obtained with a high precision using DSC under a controlled atmosphere. The supercooled liquid region of metallic glasses can be observed well by employing a DSC run. The temperature difference ΔT, that is the supercooled liquid region, is defined as T_x-T_g. Metallic

glasses behave more like liquid within this region. However, since a chemical equilibrium is not achieved during this period, the system is set to be in quasiequilibrium state [53]. Figure 2.4 reveals the critical T_g and T_x points on DSC trace of an Al-based metallic glass.

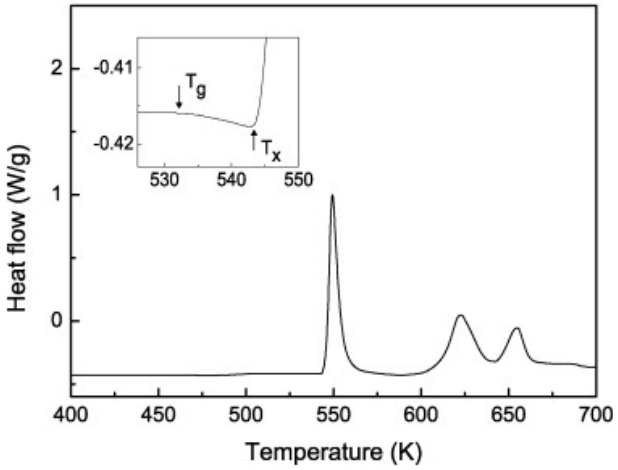

Figure 2.4 DSC trace of $(Al_{86}Ni_9La_5)_{98}Zr_2$ ribbons at constant heat rate of 20 K/min. Adopted from [52].

In Al-RE based metallic glasses, it has been shown that the RE content in glassy alloys changes the crystallization temperature T_x thus affects the thermal stability of the system. Different RE contents in binary Al-RE alloys can cause either an increased T_x of the first exothermic reaction yielding a higher thermal stability or an alteration of the phase transformation sequence changes. Figure 2.5 shows the change in crystallization temperature with respect to RE addition.

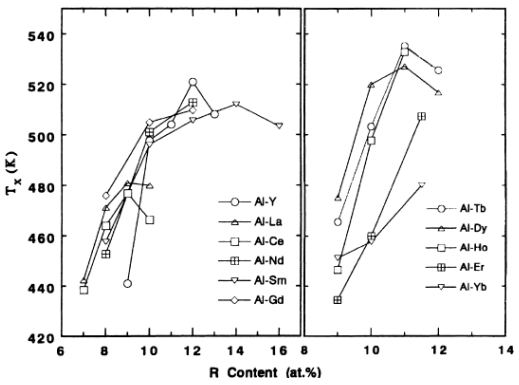

Figure 2.5 Change in crystallization temperature (T_x) with RE content in Al-based metallic binary metallic glasses. Adopted from [45].

2.3 Experimental Procedure

2.3.1 Production of Alloys

The master alloys were produced as ingots prepared in a copper hearth electric arc melting under argon atmosphere and remelted couple of times to ensure the compositional homogeneity. Amorphous ribbons of $Al_{90}Tb_{10}$ with 25-35 micrometer thickness and 2-2.5 mm width were produced with single block melt spinner operated at a tangential wheel speed of 30 m/s. Amorphous $Al_{100-x}Tb_x$ and (where $8.5 \leq x \leq 10$) sputtered films with 9-10 micrometer thickness were produced using liquid nitrogen cooled copper target cooled magnetron sputter process. Specimens were produced at Ames Laboratory DOE, USA. Figure 2.6 shows the produced as-spun ribbons and as-sputtered films.

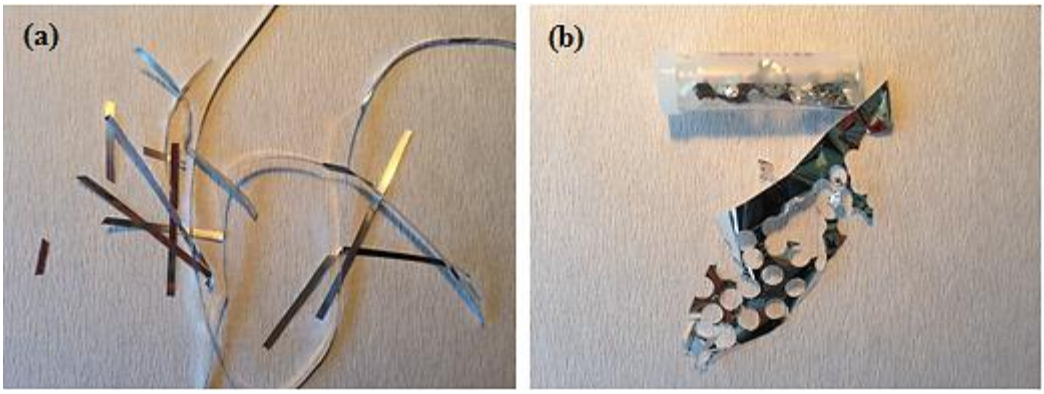

Figure 2.6 (a) Melt-spun ribbons and (b) sputtered films of $Al_{90}Tb_{10}$.

2.3.2 Differential Scanning Calorimetry Analysis

Differential scanning calorimetry (DSC) experiments were carried out using Perkin Elmer and Seiko 7000 DSC. Ribbons and sputtered films of $Al_{90}Tb_{10}$ were filled in aluminum pans and enclosed with aluminum lids. Samples were heated at different rates of (5, 10, 20, 30, 40, 60 K/min) from room temperature to 773 K under a protective N_2 gas atmosphere. For the preparation of interrupted heating specimens to be investigated under electron microscope, ribbons and the sputtered films were heated up isochronally to predetermined peak temperatures for each exothermic event at 40 K/min heating rate and quenched to room temperature. Figure 2.7 shows the instrument, Al pans and lids along with pressing tool to cover the lid on the pan and heating chamber explained in Chapter 1.

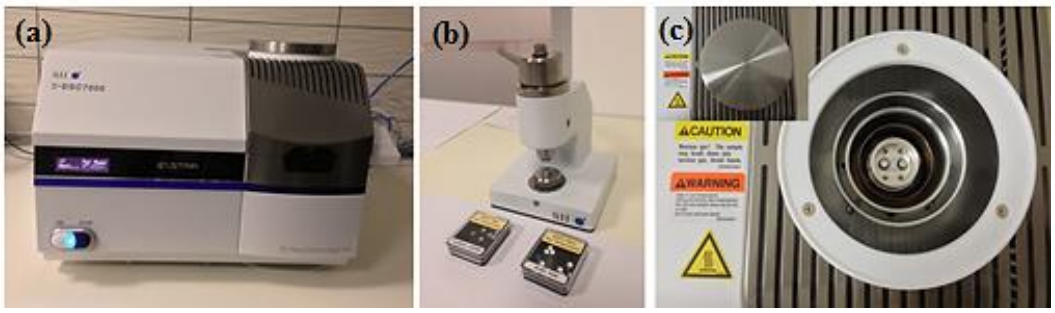

Figure 2.7 (a) DSC instruments (b) Al lids and covers and (c) heating chamber of DSC.

2.3.3 Transmission and Scanning Electron Microscopy Analysis

TEM analysis were performed in JEOL JEM2100F field emission scanning/transmission electron microscope at 200 keV operating voltage. Gatan beryllium single or double tilt specimen holders were used. Scanning electron microscopy (SEM) analysis was conducted in FEI Nova Nano SEM 430 Field Emission Scanning Electron Microscope to double check the nominal composition of the specimens by Energy Dispersive X-ray spectroscopy (EDS) especially for the grinded ribbons with SiC emery papers for synchrotron X-ray experiments.

The specimen preparation for TEM is essential to have a clear and representable investigation area that has sufficient thickness, typically 100 nm around the hole, on the specimen. Amorphous materials should be handled carefully during the specimen preparation step for TEM analysis since any crystallization event may easily occur due to thermal or mechanical regards. Specimens must be kept cooled during an ion milling procedure against any temperature rise within the specimen. Similarly, specimens should be held with utmost care with tweezers not to cause any bending or fracture that may also cause crystallization due to mechanical deformation.

In this study, TEM specimens were prepared in three steps for ribbons and two for sputtered films. Both melt-spun ribbons and sputtered films were cut down to proper round shape for TEM holder by the help of a punch. This was followed by the dimpling process to make a thinned zone having a thickness of 10 micrometers using Fischione Model 200 Dimpling Grinder for melt-spun ribbons. Dimpling step was not applied for sputtered films since that their thickness was already around 10 micrometers.

Second step of specimen preparation was performed to obtain a hole for TEM analysis. For this electropolishing was employed with Fischione Model 110 Twin Jet Electropolisher at temperatures ranging from 235 to 240 K in an acidic solution (25 volume % nitric acid 75 volume % methanol). Electropolishing was operated at 10 V and perforation process was carried out intermittently having 15 seconds periods for each run to see whether the hole is

created for melt-spun ribbons and for 5 seconds for sputtered films, respectively. It was quite hard to handle sputtered films by tweezers because of their brittleness, i.e. devitrification to crystalline phase and due to their overall thickness which cause a possibility of being torn apart, two copper disc shaped TEM specimen grids were veiled on the sputtered films before attachment to electropolisher lollipop. For those sputtered films having relatively ductile behavior, after obtaining round shape with punch, the films were directly undergone to electropolishing step.

For the final step, specimens were cleaned of the organic remaining which might lead wrong interpretation in TEM analysis, i.e. dirt, on the surface with Fischione (Model 1020) plasma cleaner for 1 minute. In this step attention should be given for the duration of cleaning since longer times may result in oxide particles on the surface of the specimen. Figure 2.8 provides the TEM specimen preparation steps that have been used for ribbons and sputtered films.

Albeit special efforts were given, some artifacts may remain within the system due the very nature of electropolisher for example. Contrast difference may occur since the solution preferentially attacks to Al part of the specimens. Thus for the TEM analysis interpretation one should bear in mind that artifacts may be present in the specimen and analyses the results accordingly.

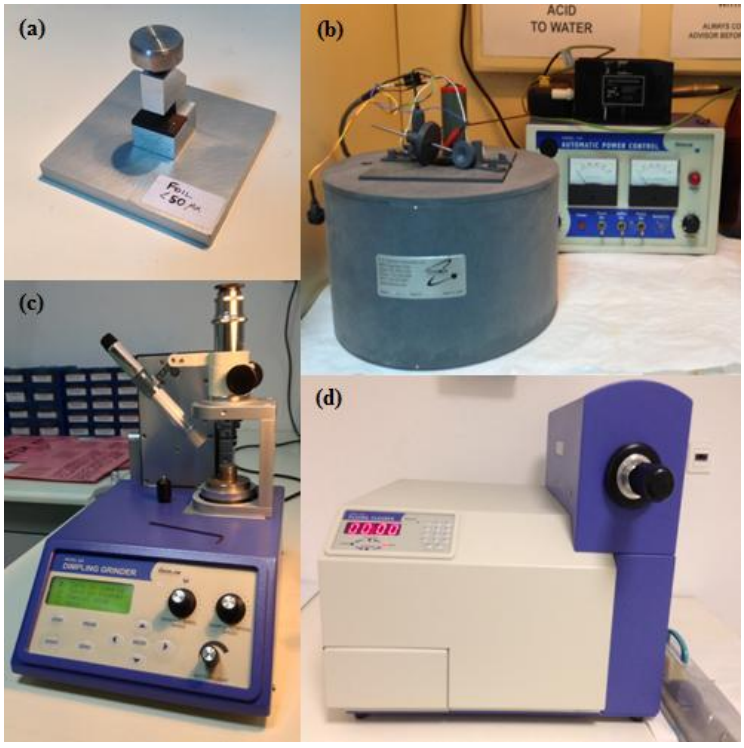

Figure 2.8 Specimen preparation steps for TEM analysis (a) punch (b) dimpler (c) electropolisher and (d) plasma cleaner.

2.3.4 Synchrotron X-Ray Diffraction Analysis

Synchrotron radiation was used to resolve the atomic structure and to trace in-situ phase transformations upon heating the melt-spun ribbons and the sputtered films of $Al_{90}Tb_{10}$. In this respect, three different beamlines in two distinct synchrotron facilities were used, namely Elettra in Trieste, Italy and Advanced Photon Source (APS) at Argonne National Laboratory, USA in collaboration with the Midwest Universities Collaborative Access Team (MUCAT).

The majority of the experiments regarding the phase selections in melt-spun ribbons and sputtered films of $Al_{90}Tb_{10}$ alloy were carried out at 7.1 MCX beamline in Elettra. Elettra is a third generation synchrotron facility operated at 2.3 GeV accelerating voltage and 7.1 MCX beamline offers energies in range of 20-23 keV. A double Si single crystal (111) monochromator having an active area of 50 x 50 mm^2 was used to select a wavelength of 0.0619882 nm. A point detector is used to collect diffracted data in back reflection mode with a 4-circle Huber goniometer having 2θ angular precision better than 0.0001°. A spinner tool is attached for the capillary experiments to rotate the sample at 3 revolutions per second. A standard Si powder was used to calibrate beam position.

Sample preparation procedures are as follows. Melt-spun ribbons and sputtered films were cut by a razor blade and filled into pyrex capillaries having 0.5 mm diameter, 10 μm wall thickness and softening temperature around 1073 K. Capillaries were sealed under vacuum in order to prevent oxidation during high temperature experiments. High temperature resistant (up to 1523 K) glue was used to thicken the sealed end of the capillaries to easy handling. Figure 2.9 shows the steps of sample preparation for synchrotron experiments.

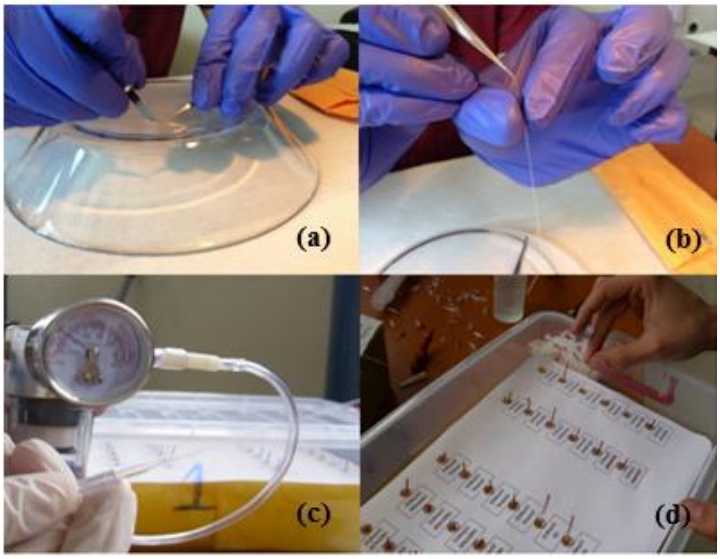

Figure 2.9 Synchrotron specimen preparation steps (a) cutting (b) filling in the X-ray transparent pyrex capillaries (c) sealing under vacuum (d) dipping to glue and placing.

The pyrex capillaries were heated using a hot air blower placed beneath the rotating capillaries at a constant heating rate of 5 K/min. The temperature of the samples was measured using the thermocouples placed right before the exit of the blower having ± 2 K tolerance. Two different heating sequences were used to detect the evolving phases from the amorphous matrix one of which the capillaries were heated from room temperature up to 833 K at constant heating rate of air blower. Capillaries were held isothermally at each 20 K step increase in the temperature and diffraction data were collected in 4°- 20° 2θ range with 0.05 $°s^{-1}$ step size and 1 second exposure time. The other heating sequence includes heating the samples from room temperature up to 573 K and X-ray diffraction data was collected while samples were held isothermally at every 10 K increase. The 2θ angular range is extended for this sequence up to 4°-26°. In order to conduct phase identification experiments, samples were heated to the pre-determined temperatures dictated by the first heating sequence and cooled down to room temperature. Each sample were exposed to X-ray beam in 4°-26° angular range with $0.05°s^{-1}$ step size and 3 seconds of exposure time in order to obtain better intensity values for the peaks. Empty capillaries under the same conditions were exposed to X-ray beam and used for background correction for the diffraction data obtained in high temperature experiments.

For the room temperature experiments flat amorphous as-spun ribbons and as-sputtered films were attached to the sample holder and held without rotation. The angular range was set between 0.5 °- 90°, step size was selected as $0.1°s^{-1}$ under 5 seconds of exposure time. Samples were placed perpendicular to the incident beam. Figure 2.10 shows the flat sample holder for the room temperature experiments and 7.1 MCX beamline.

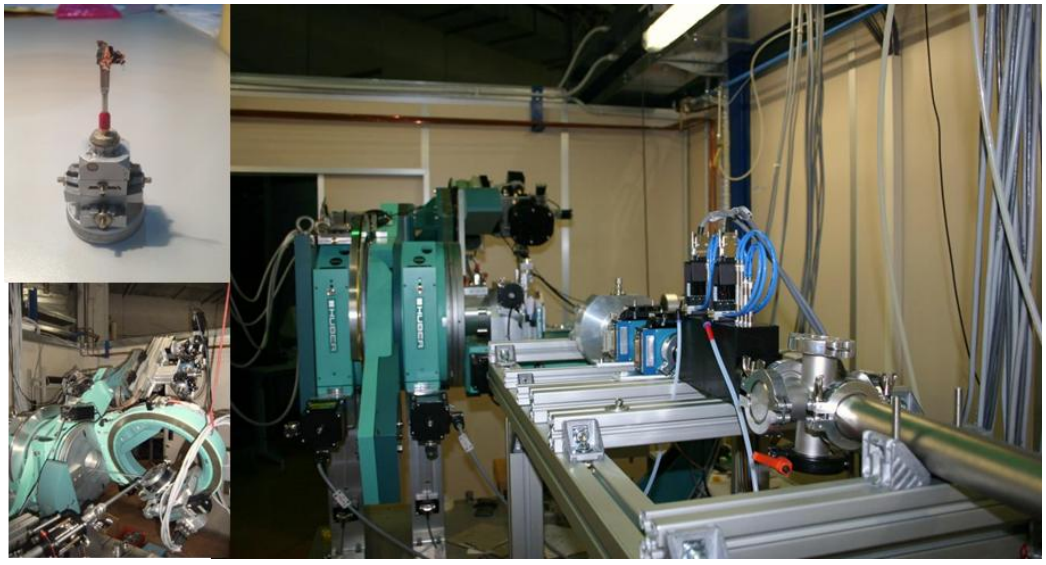

Figure 2.10 Flat sample holder and MCX beamline experimental hutch.

The second beamline used in Elettra synchrotron facility was SAXS beamline 5.2L where simultaneous SAXS and WAXS experiments can be conducted in with 2D detectors such as MAR300 image plate, a CCD and a Pilatus 100K detector. Figure 2.11 shows the experimental hutch of SAXS beamline 5.2L in Elettra. The 2D data reduction procedure is given in the following section. The aim of this experiment was to investigate the primary crystallization of fcc-Al phase in melt-spun ribbons and sputtered films. Yet due to the unfortunate problems occurred during beam time, only room temperature data could be collected which can be given here as a supportive result regarding the amorphous nature of sputtered films and melt-spun ribbons due to the fact that ribbons were thinned down to 10 μm thickness, the same as the sputtered films by grinding with SiC emery paper. The samples were examined under FEI Nova Nano SEM 430 with EDAX detector to make sure that there are no SiC particles left on the grinded ribbons. A flat asymmetric single crystal monochromator was used to select wavelength of 0.154 nm. The reciprocal space (Q) resolution of the set up was between 7 and 25 nm^{-1} in such a way that pre-peak and main amorphous peak could be detected.

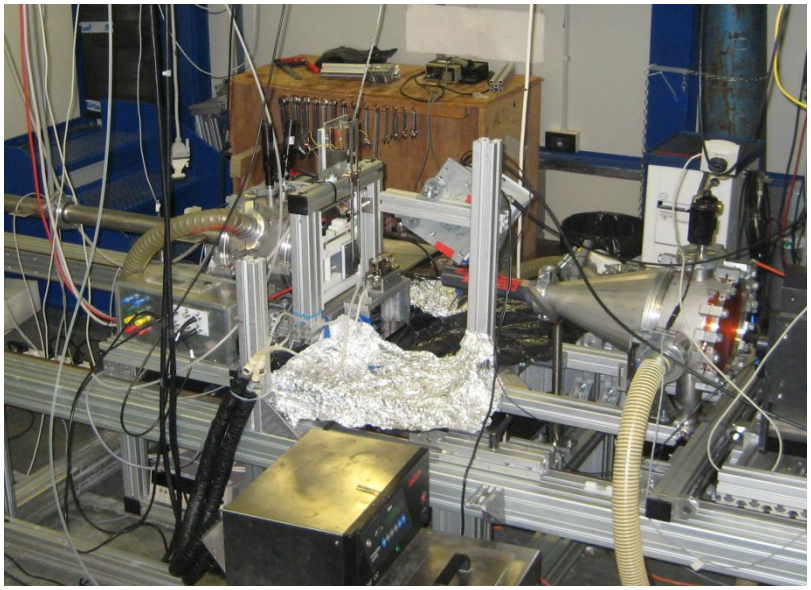

Figure 2.11 The experimental hutch of SAXS beamline 5.2 L Elettra.

The other synchrotron experiments were carried out independently in Advanced Photon Source (APS) beamline 34 ID-E at Argonne National Laboratory, USA in collaboration with the Midwest Universities Collaborative Access Team (MUCAT). Melt-spun ribbons of $Al_{90}Tb_{10}$ were placed in 2 mm diameter quartz capillaries and sealed under vacuum to prevent oxidation. A 2D Detector was used to collect diffraction data. The samples were exposed to radiation for 6 seconds per scan under isochronal conditions at a constant heating rate of 10 K/min from room temperature to 793 K. However for $Al_{90}Tb_{10}$ sputtered film the

data obtained lacked of being good enough to interpret. Therefore the experiments that were taken place in 7.1 MCX beamline are crucial for comparison of melt-spun ribbons and the sputtered films.

For 2D to 1D data reduction Fit2D Software were used [54]. As a calibration material a reference Si powder that had been purchased from National Institute of Science and Technology (NIST) with a 9 digit precision in lattice parameter has been exposed to the same wavelength at room temperature to calibrate the sample to detector distance. This calibration was done in such a way that a successive series of 5 data point inputs from the Si (111) reflection ring in Fit2D software. After obtaining calibrated distances 2D image data were reduced to 1D intensity versus 2 theta plot. The empty capillary data were subtracted from sample data before the reduction, in 2D image format.

2.4 Results and Discussions

2.4.1 The Amorphous State

Figure 2.12 shows the bright-field (BF) TEM images of melt-spun and sputtered film of $Al_{90}Tb_{10}$ samples. The featureless microstructure that is characteristic of any amorphous matrix can be seen in micrographs. The selected area electron diffraction (SAED) patterns of corresponding images confirm the amorphous nature having no periodic long range ordering.

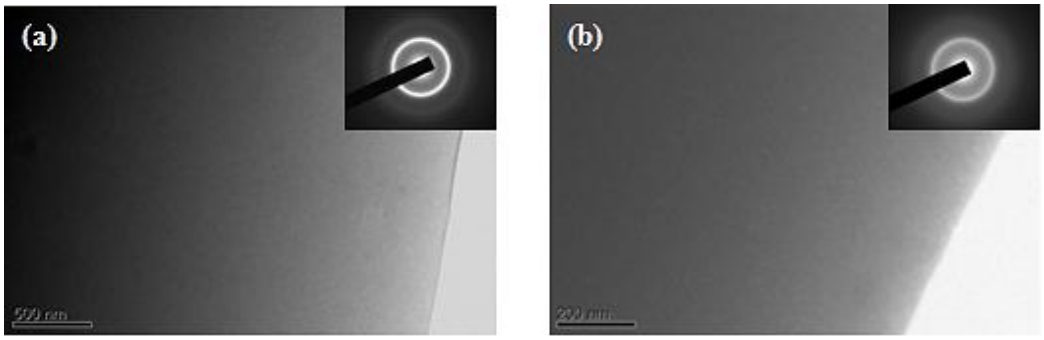

Figure 2.12 BF images along with SAED of (a) melt-spun ribbons and (b) sputtered films $Al_{90}Tb_{10}$ amorphous alloy.

As it is seen from Figure 2.13 the room temperature back reflection XRD data is in accordance with TEM results regarding their amorphous structure for as melt-spun and as-sputtered samples. The main halo can be observed in ribbons and the sputtered films that is the characteristic feature for amorphous materials. A pre-peak is observable for the melt-spun ribbons that has been reported in earlier works [49, 51]. However for sputtered films this pre-peak that has been attributed for the topological ordering between Tb centered

clusters has a lower intensity as compared to that of ribbons. The data has been cut below 4° due to the Compton scattering effect in relatively thin sputtered films.

Figure 2.14 reveals the amorphous nature of the same samples in both 2D XRD data obtained at room temperature and the corresponding reduced 1D data along with a Lorentzian fit that emphasizes the pre-peak intensity difference for the melt-spun ribbons and the sputtered films. Both the image and the reduced data agree well with the data collected using point detector in a different beamline.

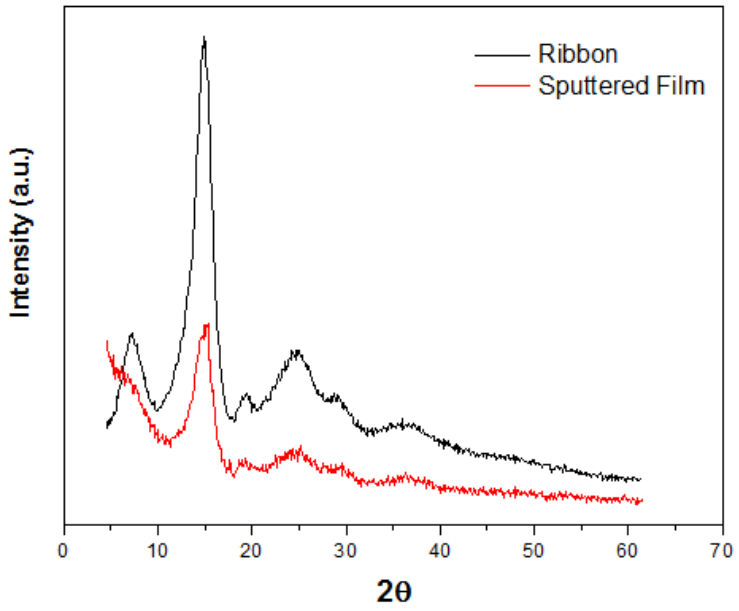

Figure 2.13 X-ray diffraction data for as-spun ribbons and as-sputtered films of $Al_{90}Tb_{10}$ at room temperature.

The TEM and XRD results clearly indicate a fully amorphous structure for the melt-spun ribbon and the sputtered films of $Al_{90}Tb_{10}$. The difference in pre-peak intensity can be attributed to the intermixing of Al and Tb atoms in the amorphous matrix. For the sputtered films, atoms are distributed in a more random fashion so that the rare-earth interaction that gives rise to pre-peak is decreased or even vanished. This suggests a difference in amorphous states even though both samples can be referred as amorphous within the limitations of XRD and TEM analysis.

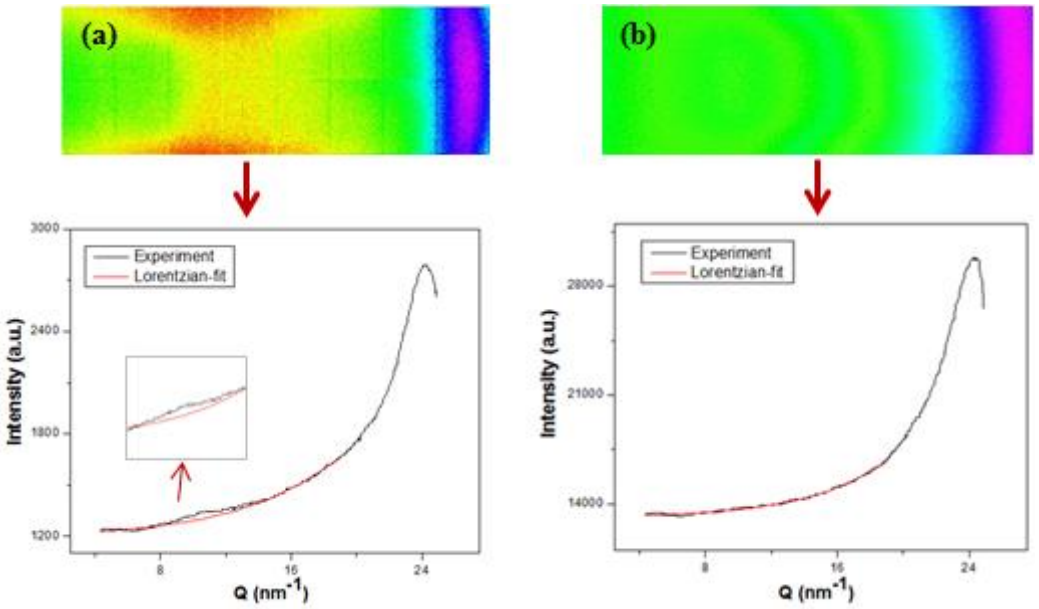

Figure 2.14 Transmission mode XRD results obtained by Pilatus 100 K 2D detector along with the reduced 1D intensity versus Q plot (a) melt-spun ribbon (b) sputtered film of $Al_{90}Tb_{10}$ alloy.

2.4.2 Controlled Devitrification

The DSC traces of melt-spun ribbons and sputtered films of amorphous $Al_{90}Tb_{10}$ at constant heating rate of 40 K/min can be seen in in Figure 2.15. The DSC traces show the difference in devitrification behavior. First of all, the fcc-Al peak for the ribbon is right next to the first intermetallic phase evolves from the matrix just after the primary crystallization of fcc-Al. On the other hand for the sputtered films this behavior is somewhat different in such a way that the primary crystallization of fcc-Al takes places at lower temperatures and the transformation curves is quite broad as compared to that of ribbons. The detailed investigation for the primary crystallization in $Al_{90}Tb_{10}$ system is given in chapter 3. The following phase which is the first intermetallic phase transforms at slightly higher temperatures and releases less amount of heat as compared to that of melt-spun ribbons. Same applies for the third phase by means of heat release as far as two distinct amorphization paths are concerned.

The clear differences in DSC trace indicate a change in the devitrification path between the amorphous ribbons and sputtered films of same composition. A matter of structural and chemical differences that relies on the amorphous state should dictate this observable difference. This was well supported with the difference in the amorphous state in wide angle X-ray scattering (WAXS) shown in Figure 2.14. Another critical result that agrees well with this finding is given in chapter 4 that exhibits how amorphous precursor affects the solid amorphous structure.

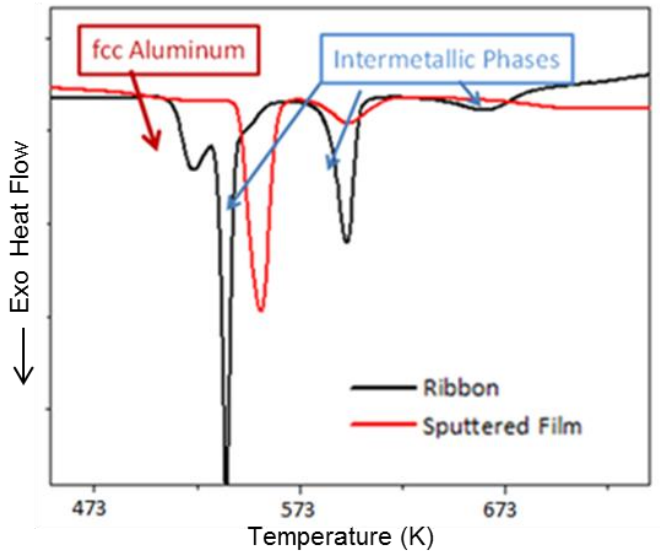

Figure 2.15 DSC traces of amorphous $Al_{90}Tb_{10}$ ribbons and sputtered films at constant heating rate of 40 K/min.

In order to investigate the structural differences that are recognized from the DSC trace, in-situ XRD and TEM are used separately to reveal the phase sequence hierarchy and morphologies of the phases, respectively. As it was mentioned in the experimental procedure section of this chapter, the DSC trace in Figure 2.15 does have a different heating rate as compared to the in-situ X-ray diffraction experiments. However this acts as a benefit since the system was more relaxed using a lower heating rate and it is an advantage to observe phase changes more closely since the related transformations are all thermally activated.

2.4.3 XRD Results

In these surface plots given below, x-axis shows the positions of the Bragg reflections, y-axis is the temperature and the contrast levels represent the diffracted beam intensity. Figure 2.16 shows the evolution of the phases from the amorphous matrix are shown for the melt-spun ribbons and the sputtered films upon heating until the last phase transformation is observed while heated at 5 K/min rate and data collected at every 20 K temperature increase. Same peaks occur with different intensities in the sequence reaching to the final phase. Transformations occur in the temperatures that can be predicted by DSC. An elaboration as to how the peak temperatures are affected by the heating rates is given in the following chapter.

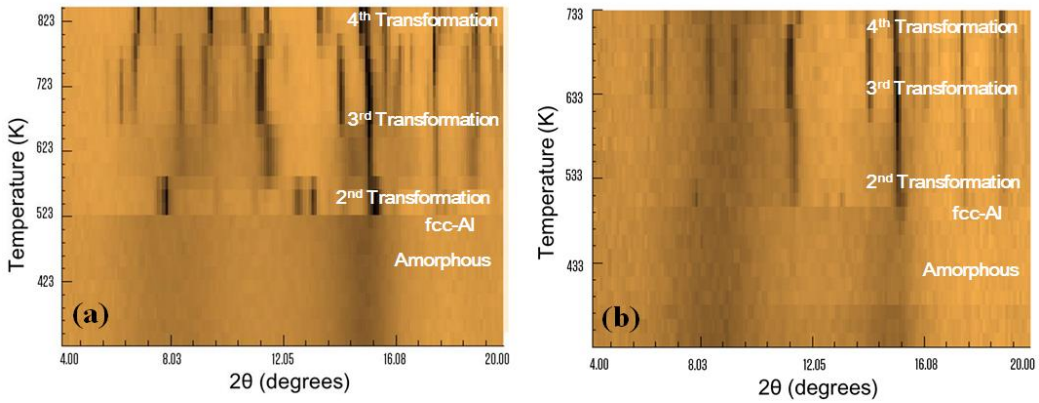

Figure 2.16 In-situ XRD of (a) melt-spun ribbons and (b) sputtered films of $Al_{90}Tb_{10}$ Alloy heated up to the last phase transformation.

Figure 2.17 summarizes the phase selection hierarchy in $Al_{90}Tb_{10}$ system. Starting from the amorphous phase both samples start their devitrification path with the primary crystallization of fcc-Al can be labeled as the first phase transformation. One point to mention regarding the difference in the data quality between melt-spun ribbons and the sputtered films is that due to the thickness of sputtered films, the signal to noise ratio intensity is relatively smaller for sputtered film as compared to that of ribbons. Upon heating the second phase transformation occurs from the remaining amorphous matrix for both of the cases. This transformation appears to be the same for both of the cases having an observable difference in transformation temperature and ratio of the intensity of the peaks as well. The following transformation yields a rather higher symmetry structure which is going to be referred as the third phase transformation from this on.

Upon further heating the present phases begins to transform into the stable phase Al_3Tb (space group Rm-3) which is shown as the fourth transformation in Figure 2.16 while fcc-Al phase still persist in the system. There is a slight transition can be observable from Figure 2.16 at temperatures between 743 and 783 K. For sputtered film the third transformation product keeps growing as temperature increases and yields to another phase that stands different from Al_3Tb.

Another feature that is worth noting is that for the melt-spun ribbons and the system reaches to equilibrium state dictated by equilibrium phase diagram where Al_3Tb and fcc-Al persist together in the system whereas for the sputtered films the final equilibrium state is reached later than melt-spun ribbons.

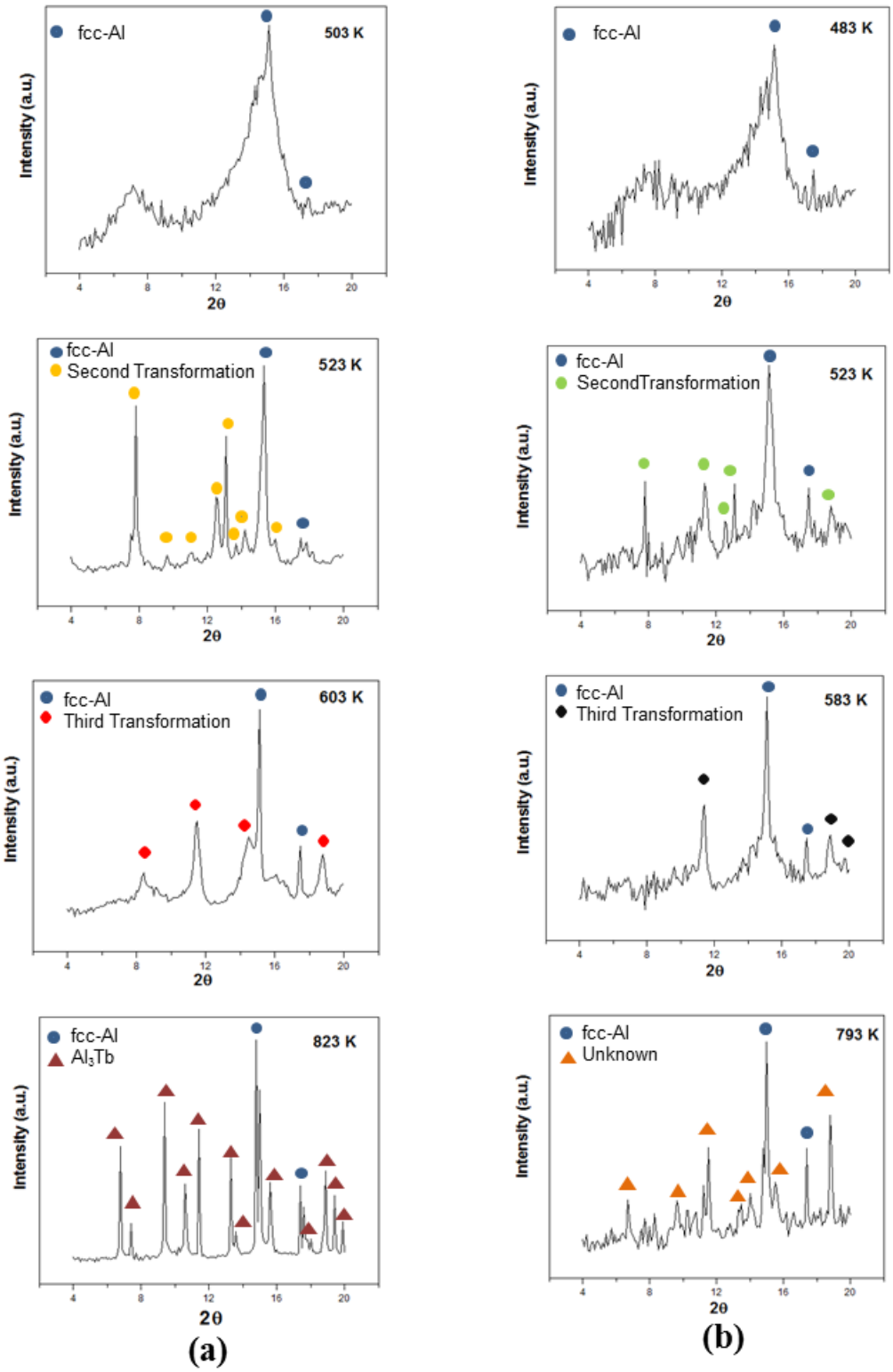

Figure 2.17 Intensity versus 2θ plots of in-situ XRD of (a) melt-spun ribbons (b) sputtered films at different temperatures.

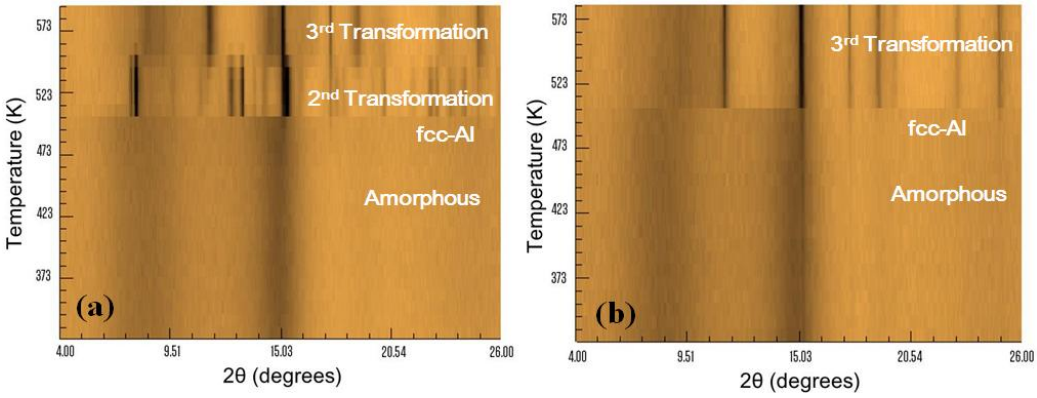

Figure 2.18 In-situ XRD of (a) melt-spun ribbons and (b) sputtered films of $Al_{90}Tb_{10}$ Alloy heated up to 593 K.

Figure 2.18 shows the in-situ XRD data of melt-spun ribbons and the sputtered films collected at every 10 K temperature increase where the samples were held isothermally between these steps upon heating to 593 K. These results possess a very important feature as to how the devitrification of the melt-spun ribbons and the sputtered films differ from one another. Both samples start from amorphous solid phase as shown in previous figures in the section regarding the amorphous state. Furthermore as dictated by the DSC results, fcc-Al nanocrystallization takes place for both of the cases as expected. However an intriguing event occurs after the fcc-Al phase transformation. The melt-spun ribbon follows the first intermetallic phase after the primary crystallization of fcc-Al phase in accordance with the phase sequence shown in Figure 2.16. The interplanar spacing values are the same with that of second transformation observed in the experiment where samples were heated up until 823 K. Further heating leads to third phase transformation for the melt-spun ribbons as in Figure 2.16. Yet this was not observed for sputtered film. It is clearly seen that the second phase transformation that is observed in Figure 2.16 (b) for both of the samples was bypassed under this heating condition for the sputtered films. Instead, fcc-Al crystallization was followed by the third phase transformation observed in Figure 2.16 which is having higher crystal symmetry.

One possible explanation can be as follows. The difference in number density of the fcc-Al nanocrystals nearly three orders of magnitude in sputtered films, which is shown later in this Chapter and given numerically by HRTEM analysis in Chapter 4, seem to play a key role in this interesting result due to growth characteristics. Smaller temperature steps that increases ability of long range diffusion by the increased time scales which appears to change the rare-earth content of the matrix as fcc-Al crystals grow. Thus a more stable phase configuration, that is the third phase transformation, shown in Figure 2.16, is able to be formed.

Figure 2.19 shows the 3D XRD plot for melt-spun ribbons and sputtered films whose surface plot is given in Figure 2.18 that is the XRD data collected at every 10 K temperature increase

where the samples were held isothermally between these steps upon heating to 593 K. As explained above it can be seen from the 3D data that both samples start with amorphous state and follow the primary crystallization of fcc-Al upon heating. It is even more obvious in 3D plot that melt-spun ribbons under goes two distinct phase transformation after fcc-Al evolution from the amorphous matrix and the change in intensities indicates that second phase transformation which evolves from the remaining amorphous matrix transforms to third phase that is having a higher crystal symmetry.

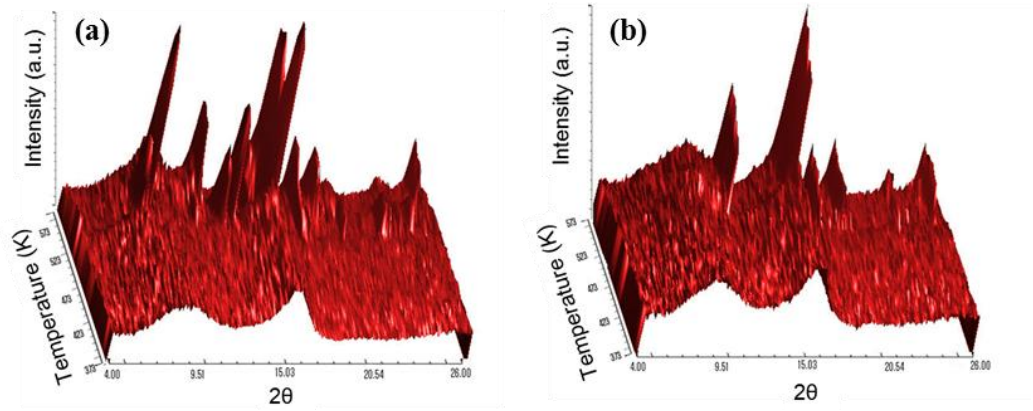

Figure 2.19 3D XRD plot for (a) melt-spun ribbons and (b) sputtered films heating up to 573 K by 10 K intervals.

On the other hand for the sputtered films the second transformation observed in melt-spun ribbons is bypassed under this particular heating sequence and directly the following phase transformation seen in the sequence of ribbon is observed right after fcc-Al crystallization. Thus starting from amorphous state for both of the cases, transformation sequence upon heating to 593 K with 10 K temperature steps is as follows;

Melt-spun Ribbons: Amorphous ⟶ fcc-Al ⟶ Second transformation ⟶ Third transformation

Sputtered Films: Amorphous ⟶ fcc-Al ⟶ Third transformation

2.4.2 TEM Results

In-situ XRD experiments revealed clear differences in phase transformation dynamics when the amorphization path is changed. In order to observe the microstructure, accurate shape and size of the phases TEM analysis were used. In this respect specimens were prepared for TEM investigations according to the specimen preparation steps that were explained in earlier sections of the chapter. Controlled devitrification experiments for TEM phase analysis carried out in such a way that melt-spun ribbons and sputtered films were heated up

at 40 K/min constant heating rate to the peak temperatures of each phase transformation curve that appears in DSC trace and instantaneously quenched down to room temperature.

Figure 2.20 shows BF images for melt-spun ribbons at 4 different temperatures dictated by the exothermic curves. Dendritic shaped fcc-Al crystals are seen from the BF images of the samples that were heated up to the first exothermic peak 516 K. Fcc-Al nanocrystals are embedded in amorphous matrix and their volume fraction is about 30 %. Upon heating to the second exothermic event, particularly at 536 K, one can see the appearance of the first intermetallic phase that has a rod like shape. The fcc-Al crystals retain within the system along with remaining amorphous matrix which is the parent phase for these two phase transformations. It seems that there is a transformation based on the alteration of the structure of the second phase transformation to a higher symmetry phase along with the remaining amorphous observed in high resolution transmission electron microscopy (HRTEM) to yield another intermetallic phase which is the third phase transformation.

The final exothermic event reaches its peak at 663 K. During this transformation fcc-Al still persists in the system whereas other two intermetallic phases give way to one Al_3Tb which is the equilibrium intermetallic compound for the given composition dictated by the phase diagram as shown if XRD patterns of the corresponding state. As can be seen from the Figure 2.20 (d) some of the Al_3Tb phase already reached their equilibrium shape which is hexagon.

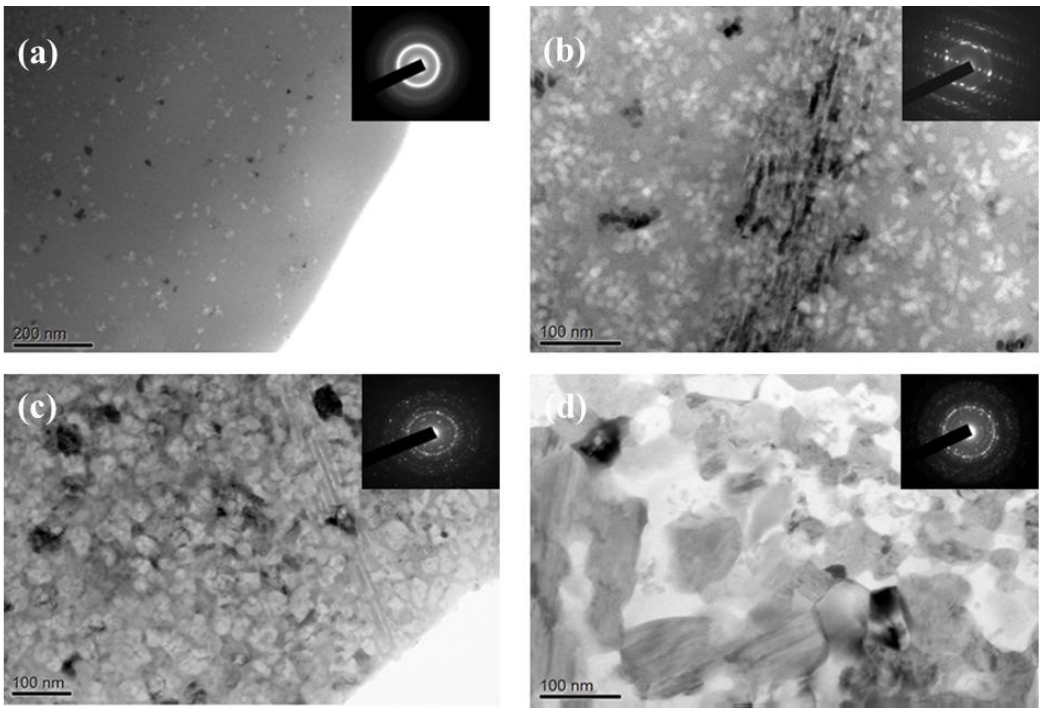

Figure 2.20 BF images of ribbons $Al_{90}Tb_{10}$ heated isochronally at constant heating rate of 40 K/min up to (a) 516 K (b) 536 K (c) 595K and (d) 663 K.

It can be seen from Figure 2.20 that after the primary crystallization of fcc-Al phase, the growth is quite sluggish by looking at especially evolution of first intermetallic. The shape and size of fcc-Al crystals within the matrix remains nearly the same with small variations during isochronal heating. This can be well attributed to the diffusional growth of fcc-Al phase that is hindered by the slow diffusivity of rather larger Tb atoms. Even during the second intermetallic phase transformation one can see that the high number density still persists in the system indicating a resistance to coarsening. This may be explained in such a way that since amorphous phase is the parent phase of fcc-Al and the second transformation which is the first intermetallic phase, the Tb content of the matrix increases to a high point and used for crystallization of intermetallic phases with correct stoichiometry. Therefore during these events, since the growth of fcc-Al phase relies on pushing the Tb atoms away from interface, interface movement is slowed down. The growth of primary crystallization products is discussed further in details in Chapter 4.

The interrupted isochronal heating TEM analysis of sputtered films of $Al_{90}Tb_{10}$ provides somewhat different results from that of ribbons. Before going any further explanation of BF images of TEM results it should be stated that some sample preparation artifacts were inevitable due to the fact that sputtered films are quite thin compared to ribbons and during electropolishing step, excessive etching may occur. These defects may occur as the black dots within the system. Furthermore folding of the sputtered film specimens may cause white lines appearing in BF images. Specimens for TEM analysis were first annealed and then prepared for electron microscopy. Although these defects should not affect the devitrification path, the features related to the sample preparation and the nature of sputtering process should be kept in mind when interpreting the results.

Figure 2.21 reveals the isochronal heating microstructures up to each peak temperature dictated by DSC with 40 K/min constant heating rate. Artifacts of sample preparation can be seen in first two images. However, from the SAED one can conclude that the first transformation is again primary crystallization of fcc-Al phase like in the case of ribbons. One important thing that is worth pointing here is the SAED pattern. It shows nearly a perfectly drawn diffraction rings indicating the distribution of the fcc-Al crystals are highly homogenous throughout the matrix and the number density of these nanocrystals are even higher than that of in melt-spun ribbons.

The following exothermic event is the evolution of an intermetallic. The morphology of the first intermetallic phase that evolves during 40 K/min heating rate in sputtered films reveal a difference in morphology compared to the second phase transformation observed for annealed ribbon specimens using the same heating rate. Unlike the rod shape intermetallic that was observed in melt-spun ribbons reaching a size of 150 nm, the second phase transformation in sputtered films exhibit a rather finer sized and homogenously distributed particles as far as the SAED patterns are concerned. This can be attributed to the number density and finer structure of the fcc-Al crystals embedded in amorphous matrix prior to the first intermetallic evolution in sputtered films. The higher number of nanocrystals with

smaller sizes casts different diffusion fields which happen to be the main reason for the difference observed in the first intermetallic phase. This issue is elaborated in Chapter 4.

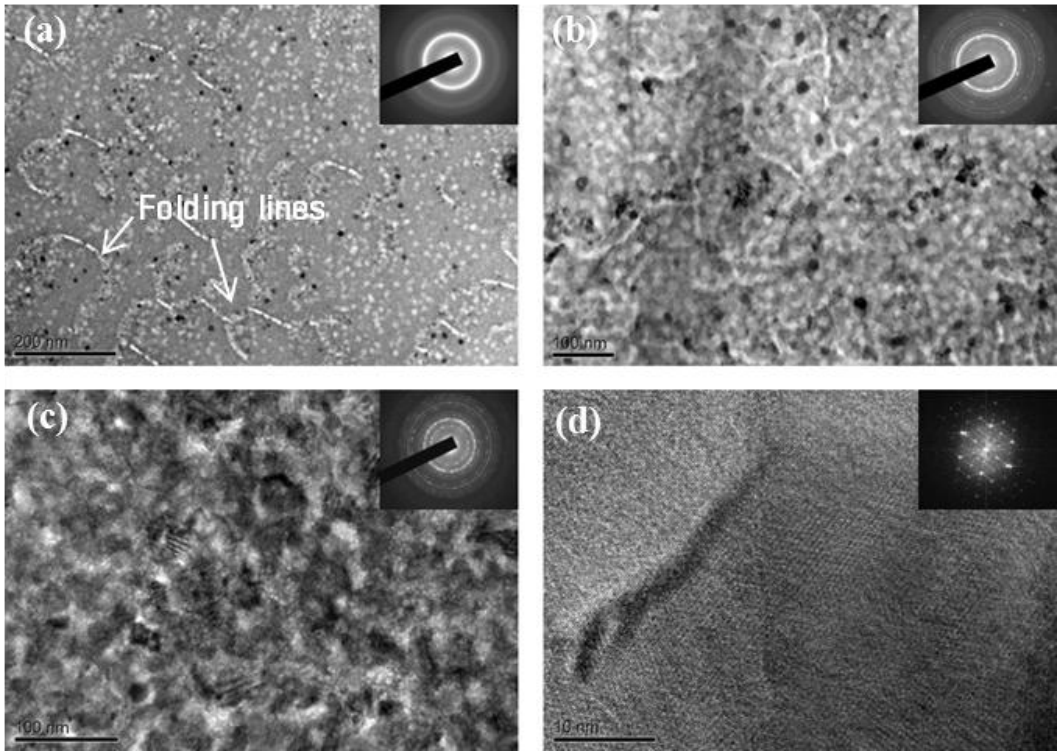

Figure 2.21 BF images of sputtered films of $Al_{90}Tb_{10}$ heated isochronally at constant heating rate of 40 K/min up to (a) 505 K (b) 549 K (c) 591K and (d) 696 K.

Figure 2.21 (c) shows the third phase evolution and as it can be seen from the BF image the features of homogenously distributed intermetallic particles are readily available in the system. The contrast provided by the transformation of amorphous phase to be completed yields in a better observation potential for the figure.

For the last phase transformation according to DSC trace due to brittleness of the sample, an adequate specimen for TEM observation was lacked. Therefore the samples prepared for the investigation of the last phase transformation does not pose a sufficiently good bright-field image due to excessive thickness for the observation. Nevertheless couple of HRTEM image was obtained and the corresponding fast Fourier transform (FFT) of the images showed a six fold symmetry that is the case for Al_3Tb with the adequate d spacing values. However due to the interaction of electrons with electrons, the scattering of charged particles leads to deviations in true d spacings as and the diffraction results obtained are not sensitive as XRD. Therefore when interpreting those results this should be kept in mind.

Even though fcc-Al crystals evolve in both types of samples, in the case of sputtered film bright-field resolution is not capable of revealing nanocrystals. Instead one can see the size

and shape difference of these Al nanocrystals between melt-spun ribbons and sputtered films by HRTEM analysis. Figure 2.22 shows the HRTEM images of dendritic and spherical fcc-Al nanocrystals in melt-spun ribbon and sputtered film, respectively. Another major difference between devitrification of melt-spun ribbons and the sputtered films can be seen as HRTEM images show the size of dendritic nanocrystal is around 25 nm whereas the size of spherical nanocrystals evolved in sputtered film is around 2 nm. This is quite a plausible result as far as the SAED of corresponding BF images are concerned. Therefore the number density of these nanocrystals in sputtered film must be higher compared to the number density in melt-spun ribbons. The change in the size, shape and number of the fcc-Al nanocrystals for these two types of samples obtained by diverse production methods will be elaborated and discussed more along with number density calculations in Chapter 4.

As it was mentioned earlier, while the second phase evolves, fcc-Al still persists in the system thus the intermetallic phase definitely evolves from the remaining amorphous matrix. This is shown in Figure 2.23. HRTEM shows some untransformed amorphous matrix. Yet in TEM analysis, especially in HRTEM mode, the representative area under consideration is extremely limited compared to a bulk result obtained from XRD.

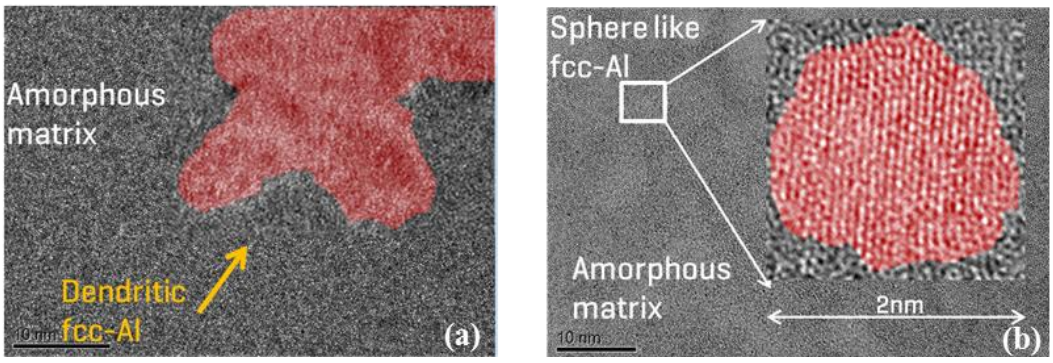

Figure 2.22 HRTEM of fcc-Al nanocrystals in (a) melt-spun ribbon (b) sputtered film.

Therefore, it may be too speculative to claim that the following transformation which is the third event occurs at 595 K evolves from remaining amorphous matrix. This may be due to the heating rate in such a way that the transformation may have taken more time to be completed for 40 K/min heating rate as compared to the heating procedure applied in XRD analysis. Thus this may in turn result in some amorphous matrix to be retained within the system onset of the third phase transformation. On the other hand together with the different morphology and size that second phase pose in sputtered films, from the HRTEM images an amorphous matrix is not observable as it was observed for the melt-spun ribbons even though both heat treatments were the same that is heating the samples up to peak positions dictated by DSC with 40 K/min constant heating rate. Thus the attribution may well be given for the fcc-Al crystallization difference which is thought to be inherited from the amorphous

state differences of these two amorphization methods. The differences in devitrification path have been attributed to the alteration of amorphous precursor.

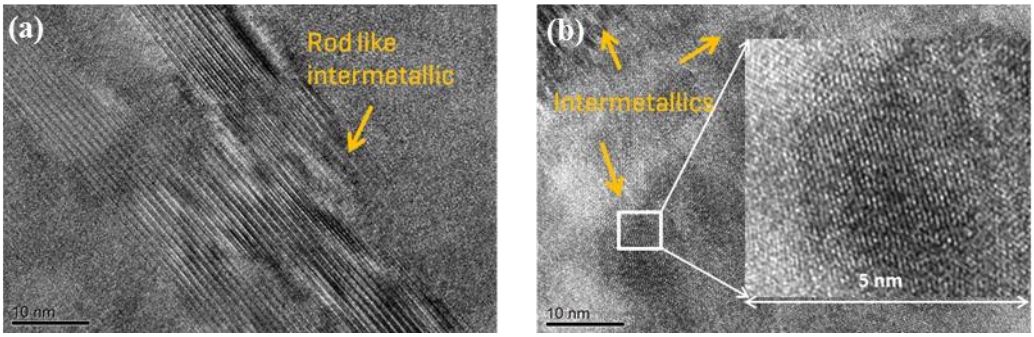

Figure 2.23 HRTEM of second phase transformation in (a) melt-spun ribbon (b) sputtered films.

2.5 Conclusion

Devitrification of $Al_{90}Tb_{10}$ alloys that are produced by two different amorphization precursors, from liquid and vapor phases, was investigated using DSC, in-situ XRD and TEM under isochronal heating conditions. Altering the amorphization precursor has showed differences in amorphous states that can be found in XRD results. Isochronal heating at constant heating rate by DSC showed a different devitrification behavior in terms of peak temperatures and shapes. This finding is elaborated by in-situ XRD analysis and TEM experiments revealing the diverse nature of devitrification path in melt-spun ribbons and sputtered films depending on their amorphous states. It is clearly shown that phase selection hierarchy differs for the two sample types under consideration. The differences in features of primary crystallization of fcc-Al nanocrystals from the amorphous matrix by means of size and shape lead to altered paths of further crystallization and evolution of intermetallic. Although the amorphous state in topological means were speculated to be the main difference there may well be the effect of the cooling rate in the production of amorphous alloys. Moreover the differences observed can also be a combined product of these different affects. However in order to understand whether the change in devitrification path is related to the amorphous state or the cooling rate more sophisticated experiments and corresponding local and topological order of the precursor atomic simulations should be made as a future study.

CHAPTER 3

KINETICS OF PRIMARY CRYSTALLIZATION IN Al-Tb MARGINAL GLASS FORMING ALLOYS

3.1. Introduction

Many researchers have given a substantial amount of effort to reveal the phase selection hierarchy in Al-TM-RE and Al-RE systems. The key in controlling the microstructure is to understand the characteristics of phase transformations to sufficient extend. For this purpose vast amount of work that has been carried out include structural and sequential identification of phases as well as their thermodynamic properties such as activation energies. In Al-RE systems it is mostly fcc-Al phase that appears as the first phase evolving from the amorphous matrix during devitrification of these alloys. Upon further heating a number of different intermetallic phase transformations are observed for the majority of the cases. Therefore it is of a great deal of importance to understand the primary crystallization, which is fcc-Al evolution in Al-RE alloys, by means of nucleation and growth behavior along with the activation energy of phase transformation.

In this chapter isothermal and non-isothermal (isochronal) analysis were carried out to investigate nanocrystallization kinetics in Al-Tb system. Devitrification path difference that was shown for melt-spun ribbons and sputtered films is going to be supported by the differences in kinetic analysis and discussions as to how amorphization precursor affects the nucleation and growth behavior of fcc-Al crystals in $Al_{90}Tb_{10}$ system.

3.2 Thermal Analysis of Metallic Glasses

3.2.1 Kissinger Analysis

It can easily be said that Kissinger analysis is one of the most widely used method to calculate activation energies of phase transformations. Reactions that are thermally activated which means the reaction temperature does depend on heating rate, have certain activation energies to overcome in order to initiate a phase transformation. As it was shown earlier DSC traces give exothermic peaks for crystallization events. Kissinger analysis basically provides an evaluation of the activation energy of a thermally activated phase transformation using the change in transformation temperatures that differs with heating rate. Rate of a reaction is given by the well-known Arrhenius relationship;

$$K = K_0 \, exp(-E_c/RT) \qquad \text{Equation 3.1}$$

Where K is the reaction rate, K_0 a material constant, Ec is the activation energy T is temperature and R is the gas constant. Since the peak temperature (T_p) depends on the heating rate (Φ) which is kept constant and the crystallization rate reaches to its maximum at T_p [55], the following relationship is obtained;

$$ln(\Phi/T_p{}^2) = const.(-E_c/RT_p) \quad \text{Equation 3.2}$$

This is the well-known Kissinger relationship that can be used for non-isothermal reaction kinetics to calculate activation energy of a reaction. A plot of $\ln(\Phi/T_p{}^2)$ vs $1/T_p$ results in a linear relationship where activation energy can be obtained from the slope of the curve.

3.2.2 Ozawa and Matusita Methods

Similar to Kissinger plot, activation energy can be obtained from Ozawa plot as well. In this analysis the degree of reaction is assumed to be constant and independent value of the heating rate resulting in the relationship [56];

$$ln(\Phi) = const.(-1.052E_c/RT_p) \quad \text{Equation 3.3}$$

Therefore from the slope of the plot $\ln(\Phi)$ vs $1/T_p$ the activation energy of a reaction can be found. In order to apply these methods at least three experiments carried out at a constant heating rate are required. Nearly twenty years later a new approach similar to Ozawa method was proposed by Matusita. This new method includes information as to how a typical phase transformation occurs by means of nucleation and growth mechanism particularly from an amorphous matrix was proposed by Matusita [57]. The applicability of this method was shown to be sufficient enough for $Li_2O.SiO_2$ glasses. The main difference of this approach from Ozawa method is that Matusita method provides information about nucleation process and growth dimension. Volume fraction of the parts crystallized (x), constant heating rate (Φ), activation energy E_c, dimensionality of crystal growth (m) and factor depending on crystallization process (n) is related with the following equation in Matusita method;

$$ln[-ln(1-x)] = -nln(\Phi) - 1.052mE_c/RT \quad \text{Equation 3.4}$$

The integer n and m are related in such a way that when nuclei forms during the constant heating process n is equal to (m + 1). However when a nuclei is formed in any pre thermal treatment n is equal to m [58]. Another advantage of Matusita method over Ozawa method is that by employing only DSC runs one can evaluate not only activation energy of a crystallization event but also the nucleation and growth mechanisms.

Nucleation and growth mechanisms have been mostly investigated and discussed under isothermal conditions due to the fact that the system is set to a more relaxed state at a fixed temperature. Therefore any transformations can be observed in time resolutions and transformation parameters are functions of time. However, under some circumstances a

system may react during the heating until a particular temperature for isothermal conditions is reached. This in turn may cause contradictions to the assumptions made for isothermal conditions. For this kind of situations non-isothermal kinetic analysis methods are more essential and proper. Using temperature dependent transformation parameters for non-isothermal conditions gives appropriate solutions for some special cases and also can be correlated for time dependent isothermal circumstances if applicable.

Table 3.1 Activation Energies for primary crystallization of some Al-based metallic glasses at their peak temperatures.

Alloy	**Kissinger E_c (kJ/mol)**	**Ozawa E_c (kJ/mol)**	**Ref**
$Al_{90}Sm_{10}$	171 ± 3	171 ± 2	[59]
$Al_{86}Ni_6Y_{4.5}Co_2La_{1.5}$	324 ± 30	333 ± 30	[60]
$Al_{85}Ni_5Y_6Co_2Fe_2$	294 ± 31	303 ± 31	[60]

3.2.3 Isothermal Kinetics

Similar to non-isothermal conditions, nucleation and growth of the phases may well be studied under isothermal conditions. In fact the vast amount of work to describe the behavior of evolving phases from a parent phase has been carried out under isothermal heating conditions. By this way transformation kinetic can be found with time dependency and can be applied to obtain desired microstructures. The well-known Johnson-Mehl-Avrami (JMA) approach has been widely used to describe nucleation and growth mechanisms. For a solid state transformation the fraction transformed (x) can be described with respect to time as follows;

$$x = 1 - exp\{-[k(t-\tau)]^n\} \qquad \text{Equation 3.5}$$

where k is the rate constant at a particular temperature, τ is incubation time and n is the Avrami exponent that gives indication as to how nucleation and growth proceeds. The interpretation of JMA analysis should be taken into account very carefully because of its must-have prerequisite. First of all it is assumed that nucleation and growth occurs homogenously and in a random fashion throughout a material. Therefore, before drawing any solid conclusion, the assumptions should be considered sufficient enough.

A very common use of this equation leads to a sigmoidal curve when fraction transformed (x) versus time plot is made. A small modification to the JMA equation results in a very useful relationship to find Avrami exponent n, that is the integer indicating the mechanism of nucleation and growth events, from the slope of the plot $ln(-ln(1-x))$ versus $(t-\tau)$.

3.3 Experimental

3.3.1 Production of Alloys

Melt-spun ribbons and sputtered films of $Al_{90}Tb_{10}$ were produced according to the methods explained in Chapter 2.

3.3.2 Differential Scanning Calorimetry Analysis

Perkin Elmer and Seiko 7000 DSC instruments were used to carry out thermal characterization of the samples. Details of the sample preparation can be found in previous chapters. 10 mg melt-spun ribbons and 2.3 mg sputtered films of $Al_{90}Tb_{10}$ were filled in different aluminum pans and enclosed with aluminum lids. The reason for the uneven weight of the samples was due to the lack of sputtered films at hand. Melt-spun ribbons were heated at 5 different rates, namely 10, 20, 30, 40 and 60 K/min from room temperature to 773 K under a protective N_2 gas atmosphere. Same ambient conditions and temperature ranges were applied for sputtered films and 4 different heating rates, 5, 20, 30 and 40 K/min, were performed due to the lesser sample amount for sputtered films compared to melt-spun ribbons. For isothermal experiments, 10 mg of melt-spun ribbons were heated up at a fixed heating rate of 60 K/min and were held for 1 hour at 483 and 493 K, respectively. After each scan an empty pan was placed into the instrument for baseline correction.

3.4 Results and Discussions

3.4.1 Isochronal Analysis

DSC traces of melt-spun ribbons and sputtered films of $Al_{90}Tb_{10}$ at constant heating rates are shown in Figure 3.1. In these figures only the primary crystallization of fcc-Al shown within the transformation temperature ranges since the attention is mostly given onto the crystallization of fcc-Al in this chapter. Nevertheless one can find the whole DSC trace of these two types of samples at 40 K/min heating rate in Chapter 2. The DSC traces for the sputtered films have been fitted into Lorentzian function behavior in order to exhibit the transformation in a better fashion. Since the peak temperatures and the area of the curves have been used for the kinetic analysis, choosing the Lorentzian plots for the experimental data causes no harm to the robustness of the results since each exothermic curve is consistent from the beginning and the end points.

Figure 3.1 reveals the difference of crystallization temperatures of fcc-Al phase in melt-spun ribbons and sputtered films. In case of sputterebd films, the crystallization of fcc-Al phase starts at lower temperatures compared to melt-spun ribbons. In that sense it can be concluded that the melt-spun ribbons possess a higher thermal stability. This can be attributed to the exothermic peak that occurs in Figure 3.2 around 423 K in sputtered films which can be identified as a phase separation in amorphous matrix to Al rich and Tb rich zones. Therefore

this may ease the crystallization of fcc-Al phase in these separated zones. However such a peak is not observable for melt-spun ribbons.

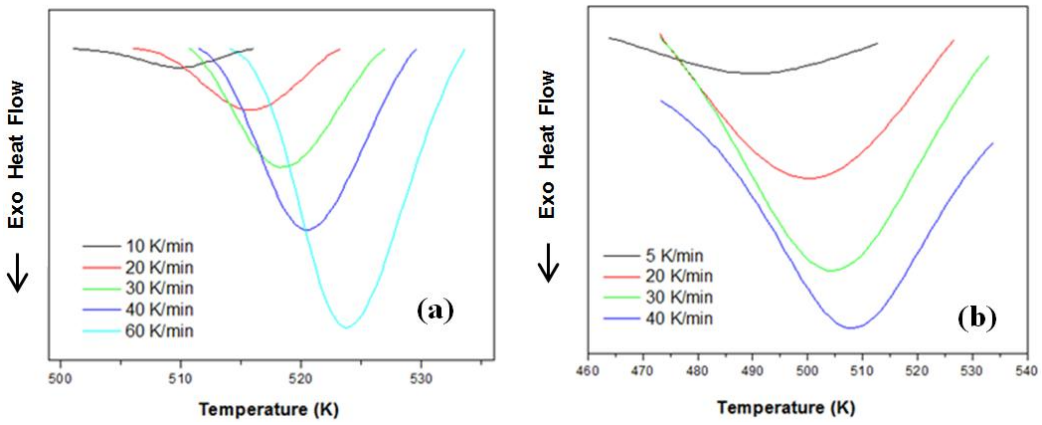

Figure 3.1 Isochronal DSC traces of (a) melt-spun ribbons and (b) sputtered films of $Al_{90}Tb_{10}$ selectively showing the primary crystallization event.

The Kissinger plots of melt-spun ribbons and sputtered films of $Al_{90}Tb_{10}$ are shown in Figure 3.3. The plot was made with $\ln(\Phi/T_p^2)$ vs $1/T_p$ axis as explained in earlier sections. Peak temperatures were used instead of crystallization onset temperature due to the fact that in assumptions of Kissinger analysis it is supposed that the reaction reaches its maximum rate is reached at peak temperature. The corresponding Ozawa plots having $\ln(\Phi)$ vs $1/T_p$ axis are also shown in Figure 3.3. The activation energies of primary crystallization of fcc-Al phase were obtained and tabulated in Table 3.2.

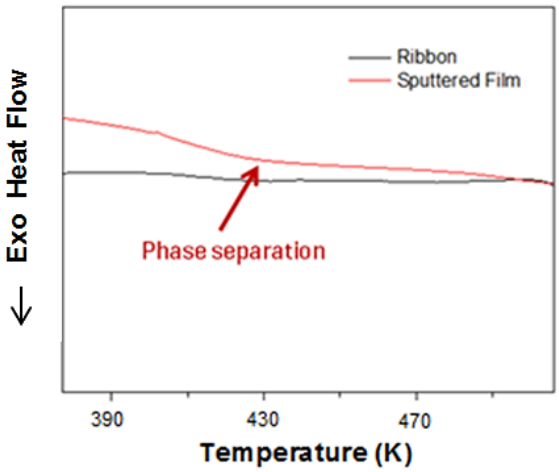

Figure 3.2 Isochronal DSC traces of sputtered film and melt-spun ribbons of $Al_{90}Tb_{10}$ alloy at 40 K/min constant heating rate.

The activation energies calculated by Kissinger, Ozawa approaches showed the difference between the melt-spun ribbons and the sputtered films in terms of energy that is required to initiate fcc-Al phase transformation. The calculated activation values differ slightly from one another in different analysis methods within the error limits. For the case of sputtered film, since there is an exothermic event prior to crystallization of fcc-Al that acts as a pre-treatment for this phase to transform which in turn lowers the transformation temperature. Likewise the activation energy for fcc-Al event is less than that of melt-spun ribbon case. This implies a structural change happens for the sputtered films upon heating before the devitrification takes place.

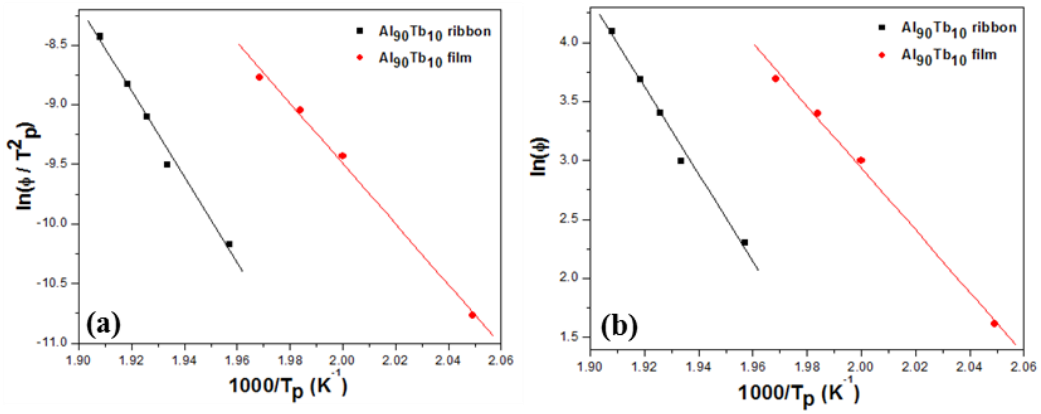

Figure 3.3 (a) Kissinger and (b) Ozawa plots of melt-spun ribbons and sputtered films of $Al_{90}Tb_{10}$.

One possible explanation of this observation may be given in the following way. Since atom probe tomography (APT) results in an earlier work reveal that as spun ribbons of $Al_{90}Tb_{10}$ in amorphous state revealed clusters of pure aluminum regions around 1 nm scale [51], it can be said that for the amorphization through rapid solidification, the system may already be divided into nano separated regions due to the fact that the internal structure of the liquid persists in a frozen like fashion having closer correlation distances between atoms achieved by the cooling rates reaching to 10^6 K/s. Thus upon heating, these separated regions might grow in size leading to the first exothermic event, fcc-Al phase transformation. On the other hand, reaching the amorphous solid state from vapor phase which is the case for sputtering, a more random distribution and higher level of disorder in the structure is likely to occur. System uses some of the energy given upon heating to overcome diffusion energy barrier provided that a phase separation which eases the crystallization of fcc-Al takes place.

It can further be inferred from the differences in activation energies of fcc-Al phase transformation for the melt-spun ribbons and sputtered films that the crystallization mechanism might be different. In order to investigate the nucleation and growth mechanism one might consider extracting the Avrami exponent from the isochronal data thus compare

the two mechanisms. For this purpose the melt-spun ribbons and sputtered films were analyzed from the continuous DSC traces at different heating rates. Equation 3.4 was used to calculate the exponent *n* and Matusita activation energy calculations. Figure 3.4 shows the sigmoidal curves for fcc-Al transformation as a function of temperature with different heating rates. From the DSC traces fraction transformed with varying temperature can be calculated by the following equation;

$$x = \frac{\Delta H}{\Delta H total} \qquad \text{Equation 3.6}$$

Table 3.2 Calculated activation energies for the fcc-Al phase transformation by Kissinger and Ozawa analysis.

Alloy	**Kissinger E_c (kJ/mol)**	**Ozawa E_c (kJ/mol)**
$Al_{90}Tb_{10}$ ribbon	298± 1	291± 2
$Al_{90}Tb_{10}$ film	210± 1	207± 2

This can be done via assigning a baseline for the fcc-Al peak and subtract the area of the peak from the baseline. One can observe the transformation temperature differences of the melt-spun ribbons and the sputtered films by looking at Figure 3.4.

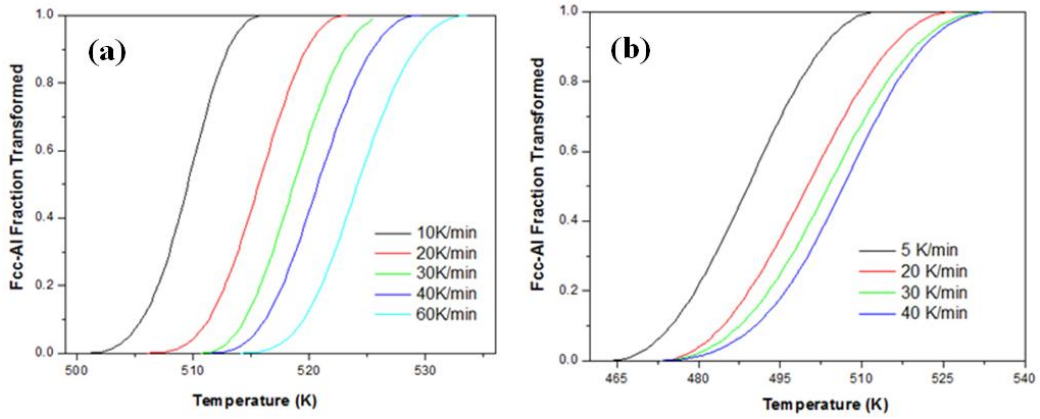

Figure 3.4 Fraction transformed vs. temperature graphs of (a) melt-spun ribbons and (b) sputtered films of $Al_{90}Tb_{10}$ at different heating rates.

The isochronal Avrami exponent *n* can be found from the slope of the plot ln[-ln(1-x)] vs. ln(Φ) and the activation energy found from the Ozawa method can be used to evaluate *m* value which provides information on the dimensionality of growth of the fcc-Al. This can simply be performed from the curve of the plot ln[-ln(1-*x*)] vs. 1/*T*. The slope is equal to -1.052mE_c/R thereby the value of *m* can be calculated. Matusita method is another form of Ozawa method which includes additional information as to how crystallization occurs. In this sense ln[-ln(1-*x*)] vs. 1/T plots were created and a linear regression has been applied to obtain the slopes of the curves. Lower transformation temperatures were not included to calculations since they deteriorate the linearity. Figure 3.5 shows the ln[-ln(1-*x*)] vs. 1/T plots for the melt-spun ribbons and the sputtered films.

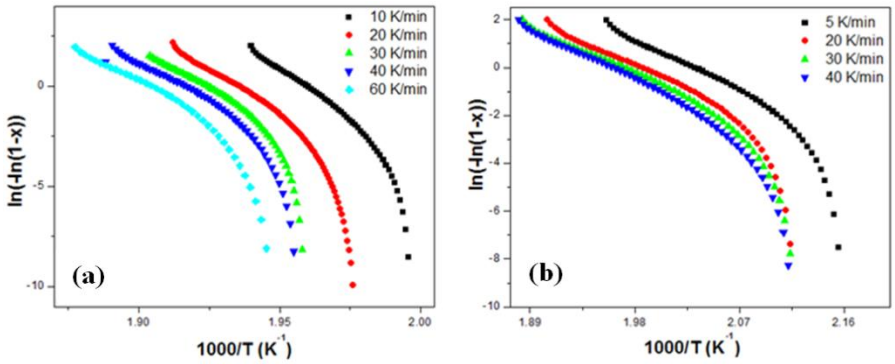

Figure 3.5 ln[-ln(1-*x*)] vs. 1000/T plots to calculate Matusita activation energies (a) melt-spun ribbons (b) sputtered films of $Al_{90}Tb_{10}$.

Taking the Ozawa activation energy for melt-spun ribbons as 290 kJ and for 207 for the sputtered films the *m* values were found and listed below in Table 3.3 for each heating rate.

Table 3.3 The calculated *m* values using Ozawa activation energies for different heating rates for melt-spun ribbons and sputtered films of $Al_{90}Tb_{10}$.

Sample Type	Heating Rate (K/min)	mE_c (kJ/mol)	*m*
Melt-Spun Ribbons	10	717	2.46± 0.18
	20	643	2.21± 0.16
	30	623	2.14± 0.13
	40	582	2.00± 0.18
	60	507	1.74± 0.15
Sputtered Films	5	168	0.81± 0.02
	20	167	0.80± 0.02
	30	155	0.76± 0.03
	40	150	0.73± 0.04

The error values appearing in the table indicate the linear fitting deviations and the same approach was used for the calculation of activation energies and the *n* values. The calculated dimensionality parameters of Matusita method exhibit variations in the case of melt-spun ribbons. The growth dimensionality of dendritic fcc-Al nanocrystals embedded in amorphous matrix decreases with increasing heating rate by a considerable amount. On the other hand dimensionality of the growth of smaller size sphere like fcc-Al nanocrystal in sputtered films remains the same possibly due to the fact that the increased number density of nanocrystals cause even more sluggish growth compared to that of melt-spun ribbons.

The estimation of *m* value obtained from activation energy calculations gives reasonable results for the dimensionality of fcc-Al growth. Now at this stage it is convenient to show the direct isochronal *n* calculation from the slope of the curves of ln[-ln(1-*x*)] vs. ln(Φ). For both of the cases, two transformation temperatures were selected to show the value of Avrami exponent. It should be noted that isochronal Avrami exponent was shown to be equal to 2*n* where *n* is the isothermal Avrami exponent [61]. It has also been shown that for the values of isochronal *n* to be higher than 3 indicates interface controlled growth process [62]. Thus the interpretation of the isochronal *n* value should be carried out cautiously.

In melt-spun ribbons, 4 data points were used out of 5 different heating rates since the sigmoidal curves of heating rates 10 K/min and 60 K/min cannot be intersected by one fixed temperature at the same time. For the case of sputtered films, 4 heating rates (5, 20, 30, 40 K/min) were applicable to choose common temperatures. Figure 3.5 shows the linear fit for the selected data points to evaluate the Avrami exponent *n*.

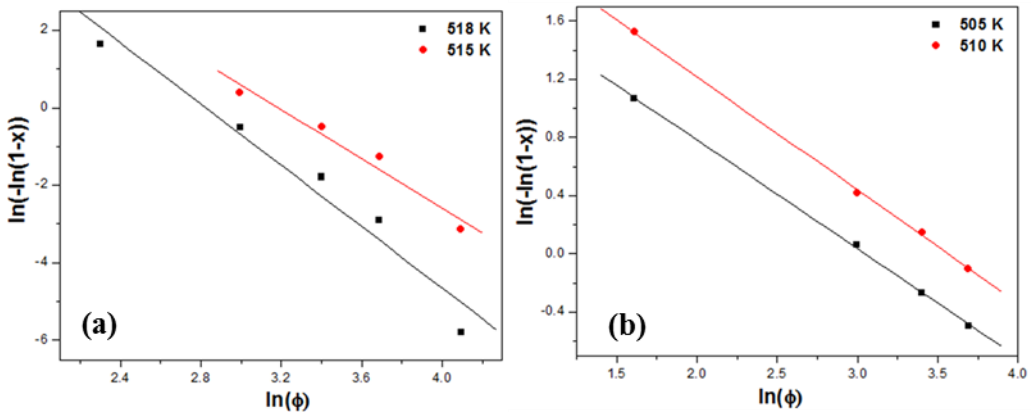

Figure 3.6 Isochronal Avrami plots for (a) melt-spun ribbons (b) sputtered films of $Al_{90}Tb_{10}$ at two different temperatures.

For melt-spun ribbons *n* is found to be 3.95 ± 0.48 for 518 K and 3.17 ± 0.44 for 515 K, respectively. This value corresponds to interface controlled growth according to [62]. However this result contradicts with earlier studies which showed the growth of fcc-Al

nanocrystals embedded in amorphous matrix is diffusion-controlled according to the isothermal JMA analysis. Of course when interpreting Avrami exponents and the applicability of this approach in a particular system, the assumption should be taken into account carefully. On the other hand according to Ruitenberg et. al [61] the *n* value found can be correlated with JMA isothermal *n* value by taking the half of what was found. Thereby the *n* value of this study can be correlated with 2-2.5 of isothermal studies that indicates diffusional growth.

The sputtered films showed an *n* value that was calculated through Figure 3.6 (b) appears as 0.8 ±0.02 for both 505 K and 510 K. This in fact turns out to be the first obvious difference in isochronal analysis that as the temperature increase during the linear heating upon advancing transformation, a single growth mechanism is possessed by the system. In contrast, fcc-Al nanocrystals in met-spun ribbons show a variation in *n* value as the temperature changes which indicates more than one mechanism might involve in the growth process such as diffusion controlled and mixed interface and diffusion controlled growth.

An important outcome of the Matusita growth analysis is that the earlier studies and this work are in agreement as far as a pre-heating process is concerned. According to Matusita method if the nuclei forms in any pre-process that also involves a process during the linear heating n is equal to *m* which is the case of sputtered film. This may be attributed to the phase separation occurs prior to primary crystallization which act as a pre-heating product affecting the physical state of the system. However as APT results showed in an earlier study [51] the as-quenched structure already possess the 1 nm sized pure Al regions where the crystallization is thought to be aided from. Thus upon heating no other process occurs such as a phase separation observed in case of sputtered films. Therefore the *n* value is equal to *m+1* for the melt-spun films. At any rate it was shown that the huge difference between *n* and *m* values between the primary crystallization of fcc-Al phase in melt-spun ribbons and the sputtered films indicates a different mechanism in nucleation and growth behavior of the nanocrystals that evolve from two distinct amorphous precursors.

3.4.2 Isothermal Analysis

In order to apply JMA approach to a particular system, it is assumed that the nucleation rate is either zero which means the growth of pre-existing nuclei or constant throughout the transformation which is dictated by isotropic growth of particles proportional to time t or t^2. It will be shown in Chapter 4 that diffusion controlled growth is the leading mechanism for the melt-spun ribbons since fcc-Al dendrites grow linearly with t^2. Isothermal DSC traces for melt-spun ribbons at 493 and 483 K are shown in Figure 3.7.

Interpretation of the comparison between isochronal and isothermal DSC results enlighten us to some degree whether nucleation and growth mechanism differ. It can be seen from Figure 3.7 that lower annealing temperature increases the reaction time for fcc-Al crystallization as expected. The transformation is completed around 8 minutes for the melt-spun ribbons

annealed isothermally at 493 K whereas for 483 K the crystallization time extends to 20 minutes. Using Avrami relation by taking the assumptions that were expressed above into account for 493 K Avrami exponent is found to be around 2.5 and showed in elsewhere.

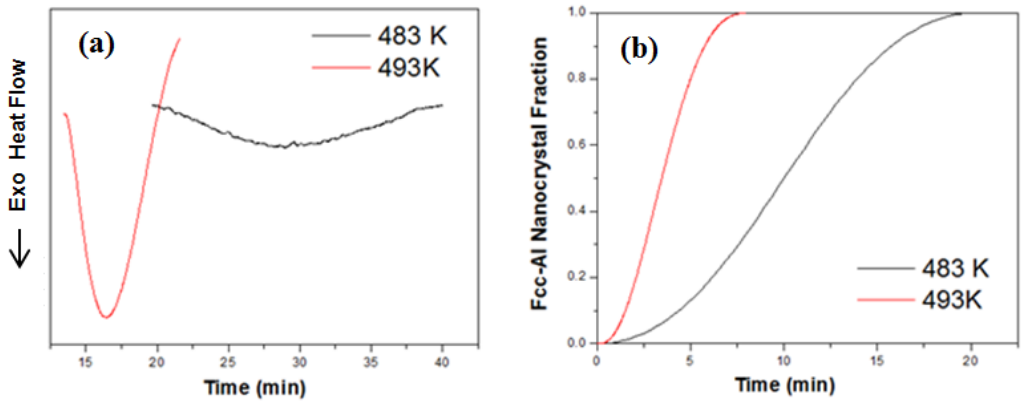

Figure 3.7 (a) Isothermal DSC traces for melt-spun ribbons at 2 different temperatures and (b) their corresponding sigmoidal transformation curves.

Figure 3.8 shows that the evolution of fcc-Al nanocrystals in melt-spun ribbons of $Al_{90}Tb_{10}$ annealed at 483 K is in accordance with previous studies. The Avrami exponent was found to be 2.5 indicating diffusional growth with constant nucleation rate. The local Avrami exponent as a function of crystallized fraction showed a monotonous increase up to 90% crystallization and a sudden jump is observed after this point. This change may be attributed to the impingement of diffusion fields of growing nanocrystals in three dimensions leading to inhomogenities to increase within the matrix.

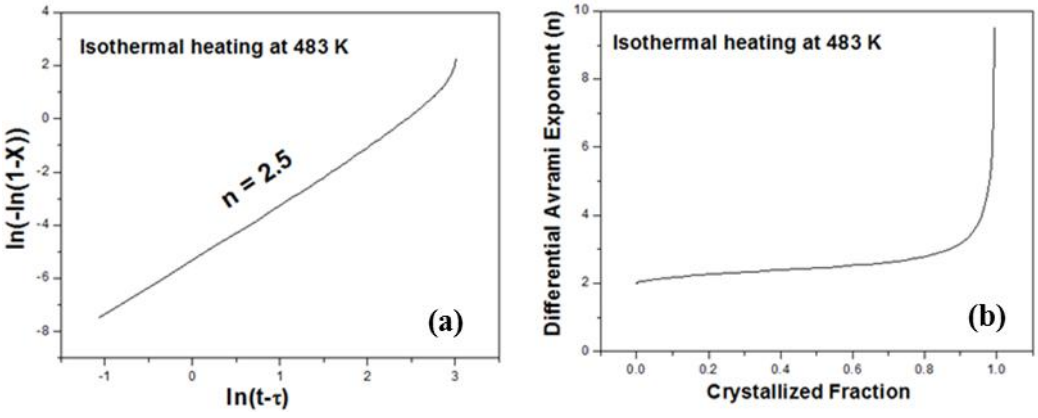

Figure 3.8 (a) Avrami and (b) local Avrami plots of melt-spun ribbons of $Al_{90}Tb_{10}$ at 483 K.

Under isothermal conditions Arrhenius equation can be used to calculate the activation energy of an alloy when rate constant is known. Thus by the use of Equation 3.1 one can find the activation energy of a reaction under isothermal conditions. Figure 3.9 shows the Arrhenius plot for the melt-spun ribbons of $Al_{90}Tb_{10}$. 155 kJ were found to be the energy barrier to activate fcc-Al crystallization under isothermal conditions. However this value contradicts with those values found in three different isochronal methods. One reason for this deviation may be related with lack of data points isothermal experiments thus affecting Arrhenius plot and resulting in a mistaken slope. It must be noted that only two isothermal temperatures have resulted in plausible DSC curves for fcc-Al phase transformation. Therefore the line was needed to be fit out of two data points in Figure 3.9.

Another reason why isothermal activation energy is different compared to isochronal analysis relies on a more solid basis can be the deviation of Avrami exponent throughout the crystallization. Since the Avrami exponent value does not remain constant as the transformation proceeds the assumptions made for the use of JMA approach gets less and less applicable. Furthermore it has been shown in a previous study that the more change in the local Avrami value through the crystallization the more difference appears between isothermal and isochronal activation energies [63]. It has been mathematically and experimentally revealed that Kissinger analysis is not in agreement with isothermal activation energies unless the local Avrami value remains the same. Therefore in case of melt-spun ribbons of $Al_{90}Tb_{10}$, activation energies found by isothermal and isochronal are not in agreement due to this reason.

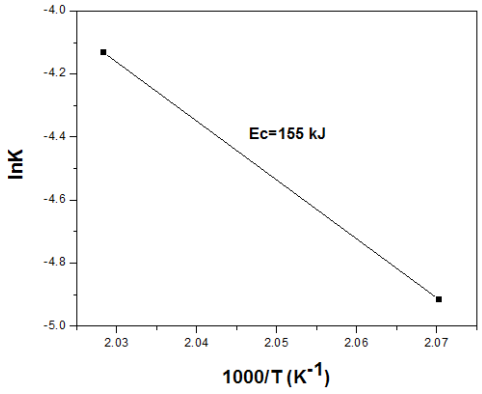

Figure 3.9 Arrhenius plot of melt-spun ribbons of alloy.

Despite the activation energies are not in agreement for isothermal and non-isothermal conditions, the exponents indicating the nucleation and growth mechanisms are in good accordance between isothermal and isochronal approaches for melt-spun ribbons. Therefore even though the isothermal Avrami investigation could not be done due to lacking of sample, this correspondence found for melt-spun ribbons gives an indication that the isochronal data

and the exponents found by isochronal analysis can be used to interpret the nucleation and growth behavior of sputtered films up to some degree. In this sense the value *n* found by Matusita method for the sputtered films indicate 0.8. Comparing this value with that of melt-spun ribbons it is not bizarre to say that the mechanism of nucleation and growth may be different and as it was mentioned earlier in this chapter that an exothermic event occurs well before the crystallization of fcc-Al phase may be responsible for such a deviation in exponent *n.*

Moreover since the phase separation in amorphous state indicates no preexisting nuclei it can be concluded that the value *m* in Matusita method indicating the dimensionality of growth must be equal to *n* due to the fact that according to the Matusita analysis *n* is equal to *m* +1 under circumstances where only growth of preexisting nuclei occurs upon heating. This approach may be a plausible manner to explain the mechanism behind the primary crystallization of the fcc-Al nanocrystals. However another feature of these nanocrystals in sputtered films may be used as a counter point of view as follows.

The peculiarities in fcc-Al crystallization of sputtered film compared to melt-spun ribbons can be found in Chapter 2 by microstructural investigations. Taking the high resolution transmission electron microscopy (HRTEM) image of fcc-Al nanocrystals in sputtered films in Chapter 2 into account, one can observe that these nanocrystals have a nearly perfect circular shape with an average size of 2 nm. For a spherical isotropic particle it is expected that growth must be in three dimensions unless there are some obstacles deteriorating the homogeneity and isotropy of the system. Therefore it is either the dimensionality found by Matusita method for melt-spun ribbons is not valid or the shapes of these nanocrystals observed by HRTEM is a rather cylinder than a circle since electron imaging shows two dimensional picture of the materials. This may be an artifact of sputtering process as the vapor condenses in accumulative layers onto one another. Yet alternative methods different from TEM, such as APT or sophisticated simulations are required to be more certain as to how these nanocrystals are deposited and this affect their nucleation growth behavior. Nevertheless the correlation between isothermal and isochronal studies by means of nucleation and growth trend to some degree for the ribbons can be used to compare the nucleation mechanism to be different than sputtered films even though the growth regime may not hold for the sputtered films.

3.5 Conclusion

In this chapter the primary crystallization of fcc-Al nanocrystals in melt-spun ribbons and sputtered films of $Al_{90}Tb_{10}$ amorphous alloys has been investigated by the use of experiments conducted using DSC. Interpretation of nucleation and growth mechanism relying on isothermal and non-isothermal (isochronal) thermal treatments to these samples showed that nucleation and growth mechanism for fcc-Al crystals are affected with the amorphization path and corresponding amorphization precursors which is in good agreement with the

results that were showed Chapter 2. It has been found that thermal stability of melt-spun ribbons is higher than that of sputtered films due to the phase separation event detected by DSC at lower temperatures for the film samples. This exothermic event for sputtered films may be a possible reason in regard to the difference observed in Avrami exponent values of sputtered films and melt-spun ribbons found by Matusita method under isochronal heating conditions. The activation energies calculated by Kissinger, Ozawa analyses in isochronal studies revealed that a higher energy barrier has to be overcome for the melt-spun ribbons which can also correlated with the phase separation prior to partial devitrification of sputtered films. It has also been mentioned that isochronal and isothermal activation energies for fcc-Al phase transformation are not in agreement for the melt-spun ribbons resembling to earlier studies in different metallic glasses.

CHAPTER 4

DEVITRIFICATION BEHAVIOR OF Al-Tb MARGINAL GLASS FORMING ALLOYS UNDER ISOTHERMAL CONDITIONS

4.1. Introduction

Unlike most of the bulk metallic glasses, marginal glass forming alloys exhibit an intriguing devitrification behavior. The interesting feature in these alloys lies in the primary crystallization products. The number density of the nanocrystals that evolve from the amorphous matrix during devitrification by primary crystallization is on the order of $10^{21\text{-}24}$ m^{-3} which is highly unexpected as long as the classical nucleation theory is concerned. This contradiction with the classical nucleation theory has given birth to many studies on this subject especially in Al and Fe based marginal glass forming alloys due to their potential importance to be used in structural and magnetic applications. In order to control the microstructure and therefore the emerging materials properties, the mechanism of nanocrystallization must be understood. Even though a great number of studies has been conducted to describe this mysterious behavior a full knowledge regarding the structure and dynamics of nanocrystallization from amorphous state is still lacking.

In this chapter Al-Tb amorphous system is studied under isothermal conditions using TEM, DSC. The amorphous state is investigated by FEM. Discussions can be found in combination with the other results in previous chapters as to how the nucleation mechanism of the fcc-Al nanocrystals can be described. A mathematical model relating the particle size and the annealing time regarding the growth of the nanocrystals embedded in amorphous matrix is presented.

4.2 Nucleation and Growth Mechanisms in Marginal Glass Forming Alloys

The steady state nucleation rate is well described by the classical nucleation theory which is capable of ensuring many nucleation events in numerous different systems. The key parameters of the theory consist of surface energy and the bulk free energy terms which are in competition along with the attachment frequency of the atoms upon the onset of transformation at a certain temperature. The driving force for nucleation can be given as the difference in the Gibbs free energy of competing phases which is related with the undercooling of the liquid for solidification processes. In case of crystallization from amorphous solid state, the viscosity and interatomic spacing terms come into play to describe the nucleation rate. Nucleation number density is given as follows;

$$N = \left[t\frac{kTN_0}{3\eta(T)a^3} \right]\exp\left(-\frac{\Delta G^*}{kT}\right) \qquad \text{Equation 4.1}$$

where N is steady state nucleation rate, t is time, k is the Boltzmann constant η is viscosity, a is interatomic spacing and ΔG^* is the activation energy barrier for the formation of a critical radius [64]. Although the equation holds well at elevated temperatures Johnson et al. revealed the inconsistency of classical nucleation theory upon crystallization of Vit 1 using small angle neutron diffraction (SANS) at lower temperatures. Figure 4.1 shows the variation of nucleation rate calculated by the classical nucleation theory approach and the experimental observation of nucleation rate out of SANS study. The figure clearly points the contradiction of the nucleation number density dictated by the calculations of classical nucleation theory and the experimental observations in an increasing fashion at relatively lower temperatures.

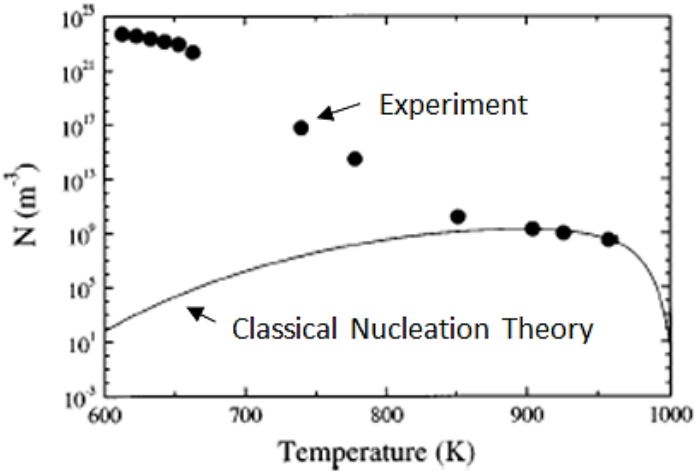

Figure 4.1 Nucleation number density determined from SANS experiment and classical nucleation theory calculations. Adopted from [64].

The unusual nucleation behavior of marginal glass forming alloys along with some bulk metallic glasses still remain obscure even though number of studies have been done to tackle this question. Nevertheless very important findings have been extracted through the studies initiated to answer this mysterious observation. Perepezko proposed the "quenched-in nuclei" theory in order to explain the nucleation behavior of Al-TM-RE and Al-RE alloys. The overall framework of this approach can be given as follows. Upon solidification some amount of small crystallites are formed which are unable to grow due to the enormous slowdown of the diffusion due to viscosity increase upon glass transition temperature. Thus those small "quenched-in nuclei" particles are entrapped within the amorphous matrix and upon heating this growth controlled system that is the transformation curve is intercepted by some fraction upon solidification, form the fcc-Al crystals [65]. They have supported their theory using a methodology in such a way that two different amorphization paths were used one of which is rapid solidification and the other is amorphization through excessive cold

rolling. These two types of samples were investigated using FEM to reveal the differences amorphous state which is attributed to the lack of quenched-in nuclei in cold sample whereas coming from liquid state resulted in fcc-Al like MRO structure in amorphous ribbons.

Another approach is the phase separation in amorphous state by spinodal decomposition [66]. Unlike quenched-in nuclei theory, this approach suggests a fully amorphous matrix which obtained by rapid solidification method that undergoes a chemical separation upon heating into Al-rich and depleted zones. Thus these Al-rich zones are said to be the regions having 74-126 nm sizes where fcc-Al crystallization takes place. The amorphous state phase separation in these alloys is described with the coupled-flux nucleation approach that is the homogenous nucleation which occurs independent of time [67].

Although both of these approaches are remarkable works regarding the evolution of primary crystallization in Al-based marginal glass forming alloys, a full agreement that describes the nucleation behavior is still lacking due to different aspects. For instance, even though the quenched-in nuclei is well supported by the FEM analysis relying on the signal that is absent in cold worked sample of the same composition, it is quite natural to question the integrity and the homogeneity of the amorphous state obtained by excessive cold working compared to melt-spun ribbons. Another issue as to how quenched-in nuclei theory can be speculated is given in the following sections of this chapter along with FEM analysis of the sputtered films of $Al_{90}Tb_{10}$ alloy. On the other hand the phase separation that is proposed to be the mechanism for some Al-based marginal glass forming alloys, specifically $Al_{88}Gd_6La_2Ni_4$ indicates in order to obtain such high number density products of devitrification the system has to have a miscibility gap in order to furnish the spinodal decomposition in amorphous state that aids the following fcc-Al crystallization. However this does not hold for binary alloys such as Al-Tb or Al-Sm system. In fact for the $Al_{88}Gd_6Er_2Ni_4$ alloy system which has a slight difference in composition with the related study in which nucleation is said to be followed by a phase separation, such behavior was not observed [66]. Moreover the chemically separated regions are quite large compared to the particle sizes of the evolving fcc-Al crystals.

A more recent study relies on short to medium range ordering for tackling this issue offers a different perspective by means of topological ordering in liquid state in Al-Tb system [51]. It was reported that high density of Al clusters in as-quenched states are inherited from the liquid state prior to quenching the melt, caused by Tb atoms attracting Al atoms thereby dividing the matrix to a continuous network. A very solid proof of that was revealed by the APT result of amorphous ribbons of $Al_{90}Tb_{10}$ alloy that has nearly 1 nm regions of pure Al clusters within the matrix that are thought to be having a massive role as to how nucleation of fcc-Al phase proceeds upon devitrification. It should be noted that liquid structure has more or less the same topological features with the solid amorphous state having slight changes in atomic positions due to higher vibration of atoms at elevated temperatures according to the Voronoi polyhedra (VP) analysis [51]. Therefore, it indeed is a promising challenge to alter the amorphization precursor from liquid, similar to the case in quenched-in nuclei study to extract potentially valuable information regarding how the mechanism of

nucleation is affected by the topological order in liquid state and therefore in solid amorphous state of course. This chapter focuses on amorphous ribbons and sputtered films of $Al_{90}Tb_{10}$ alloy to investigate their isothermal crystallization behaviors.

To design fine scale microstructures and control the materials performances, growth of the nanocrystals holds a particularly important role. The enigmatic nucleation behavior of the marginal glass forming alloys having very high number density devitrification products offers astonishing properties upon a proper control of the size of these nanocrystals. However the unusual nucleation number indeed affects the complexity of the analysis of the growth these nanocrystals. In Chapter 3 the isochronal and isothermal nucleation and growth behaviors have been investigated using DSC results. The outcomes were quite sufficient to state the difference in the nucleation and growth behavior of the fcc-Al crystals embedded in amorphous matrix. However especially for the isothermal investigations, JMA approach has its very strict assumptions to be applied on a particular system which turns out to be a problematic situation for Al-RE marginal glass forming alloys due to the fact that upon growth of the fcc-Al crystals the system is not capable of maintaining the overall homogeneity. Instead overlapping of the diffusion fields of the growing particles without interacting each which is called (soft impingement) occurs due to the very high number density of the particles where JMA approach is no longer available. JMA model is used for many phase transitions and was shown to be working well for various systems. However it only holds for the times before the impingement occurs, where the growth rate *R* is proportional to square root of the product of diffusivity (*D)* and time (*t)*. Ham model instead yields good solution with diffusivity independent of concentration and the results are reasonable except the final stages of the reaction. According to Ham the growth rate can be given as;

$$\frac{dR(t)}{dt} = \left[\frac{(Cm - C(t))}{Cp - Cm} \right] \frac{D}{R(t)} \qquad \text{Equation 4.2}$$

where C_m is the matrix and C_p is the precipitation concentration, and *C(t)* is the concentration of the interface at time *t*. Gibbs Thomson effect is neglected in this approach due to its low effect on solubility [68]. Ham model looks quite satisfactory to find the growth rate of a particle even under soft impingement circumstances. However the composition profile obtained by Ham model does not offer valuable information since the composition level is treated as an average. Frank's solution on spherical coordinate diffusion limited growth comes into play [69]. The approach involves a diffusion potential that is dependent on temperature or composition or both of them which is a function of a dimensionless reduced radius (s) which is given by;

$$s = r/\sqrt{Dt} \qquad \text{Equation 4.3}$$

where *r* is the radius *D* is diffusivity and *t* is time. This approach assumes that there is no convective diffusion instead there is only pure diffusive conditions [70]. It also refers to Nerst boundary condition of which the composition of the surface is maintained at a constant

value as the boundary moves. Thus Frank's solution can be used to model the growth of fcc-Al nanocrystals developing from the amorphous matrix and ending up with soft impingement involving composition profiles at different stages of the process.

4.3 Experimental Procedure

Melt-spun ribbons and sputtered films of $Al_{90}Tb_{10}$ alloys were produced according to the procedure explained in 2.3.1. For the fluctuation electrom microscopy (FEM) analysis aberration corrected FEI Titan field emission scanning/transmission electron microscope S/TEM was used and the experiments carried out in Material Science Department of University of Wisconsin. Amorphous melts spun ribbons and sputtered films of $Al_{90}Tb_{10}$ alloys were investigated using FEM which is a very powerful technique to probe the medium range order (MRO) in amorphous materials. The change in variance (see Equation 1.5) was recorded in 1000 sample positions with 2 nm sized beam.

The controlled annealing experiments were done in a silicon oil bath according to the isothermal DSC trace of melt-spun ribbons mentioned in 3.3.2. Melt-spun ribbons of $Al_{90}Tb_{10}$ were heated isothermally long enough to satisfy the predetermined time intervals set by DSC, 298, 365, 469, 634 and 785 seconds at 493 K. Sputtered films were held isothermally for 8, 24 and 36 minutes at the same temperature and quenched down to room temperature. For the particle size and nucleation number density calculations JEOL JEM2100F field emission scanning/transmission electron microscope were used at 200 keV operating voltage. Composition analysis carried out by energy dispersive X-ray spectroscopy (EDS) using scanning transmission electron microscope (S/TEM) mode. A beam size of 0.7 nm was used in high angle annular dark field (HAADF) Z-contrast mode with a single tilt beryllium holder for the S/TEM analysis whereas a double tilt beryllium holder was used for TEM analysis especially for the investigation of sputtered films. The compositional accuracy was tried to be maximized by the smallest beam size attained without deteriorating the sample.

4.3.1 Nucleation Number Density Calculations

Nucleation number density calculations of the fcc-Al nanocrystals embedded in the amorphous matrix for melt-spun ribbons and the sputtered films were conducted using HRTEM images due to the fact that nanocrystals in sputtered films have particle sizes that are well beyond the resolution of bright-field mode of TEM even though it is enough to resolve dendritic fcc-Al nanocrystals in melt-spun ribbons. Moreover counting the nanocrystals from the HRTEM gives even more accurate result comparing BF examination since a higher number of nanocrystals can be detected and thus included in the calculations for ribbons. Therefore the number of nanocrystals in a particular image is given by ;

$$N_A = \frac{\#\ of\ crystals}{Area\ of\ the\ Image}$$ Equation 4.4

The thickness of the examination area can be calculated through Equation 4.2

$$\frac{(I_t)}{(I_0)} = exp\left\{-\frac{t}{\wedge}\right\}$$ Equation 4.5

where the ratio of intensity of the incident beam (I_o), that is the intensity calculated from the hole of the sample, and the intensity of the beam that is transmitted through the sample (I_t) is related exponentially to the ratio of the thickness of the investigation are of the sample to the mean free path ($\wedge$) which is given as 130 nm for Al [71]. To calculate number density of nanocrystals per unit volume (N_v) the following equation can be used [72, 73];

$$N_v = \frac{N_A}{t+\bar{d}}$$ Equation 4.6

where $\bar{d}$ is the average diameter of nanocrystals and t is the thickness of the sample. 20 sets of HRTEM image were used for melt-spun ribbons and 30 sets of image were used for sputtered films each including at least two images for hole to calculate intensity of the incident beam. The intensity counts were read through the CCD detector via Gatan Digital Micrograph software.

4.4 Results and Discussions

Figure 4.2 shows the FEM results for amorphous melt-spun ribbons and the sputtered films. The difference in amorphous states that was shown in XRD results in Chapter 2 is well supported by FEM results. The reduction in Al like MRO can be seen from the variance difference that corresponds to pseudo (111) reflection of Al crystal in reciprocal space. Sputtering method results in a higher intermixing of Al and Tb atoms within the amorphous matrix due to the nature of sputtering process whereas in melt-spun ribbons having a liquid precursor due to higher viscosity, a topological order persists in the system that was detected by XRD studies that pose a pre-peak in liquid state [51]. In this respect the phase separation event that occurs at lower temperatures than the primary crystallization of fcc-Al may be an indication that the system is ought to have chemically separated zones that is already persisted in as-quenched melt-spun ribbons shown in APT results [51].

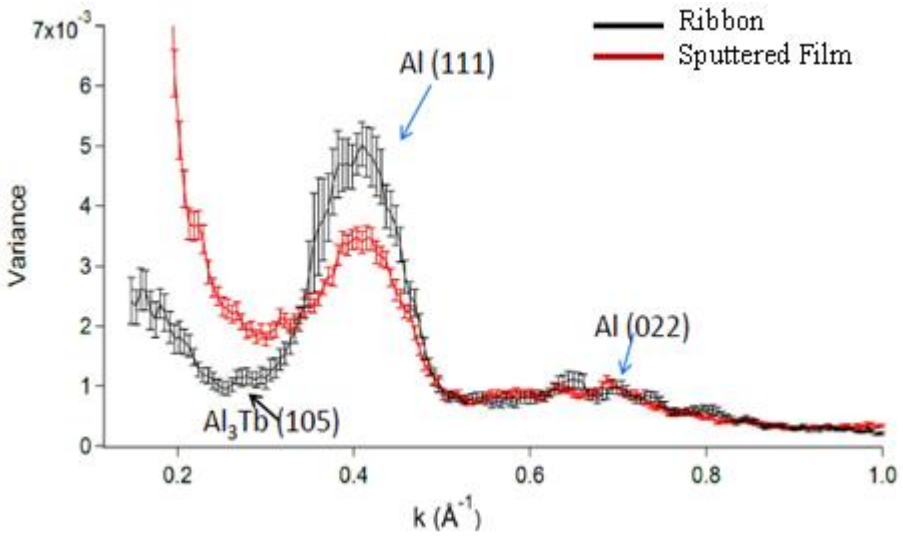

Figure 4.2 FEM results of melt-spun ribbons and sputtered films of $Al_{90}Tb_{10}$ alloy.

FEM results show that both sample types have an fcc-like MRO signal at the corresponding (111) reflection of aluminum crystal. This shows that both sample types have a topological ordering in amorphous state. Thus if quenched-in nuclei theory that suggests the occurrence of the entrapped small crystallites that transformed into fcc-Al particles upon heating is to be applied for marginal glass forming alloys, then the sputtering process that has a cooling rate on the order of 10^9 K/s is not sufficient enough not to intercept the transformation curve in TTT diagram which in turn makes the system a growth controlled instead of a nucleation controlled system. Figure 4.3 summarizes the nucleation and growth controlled metastable phases.

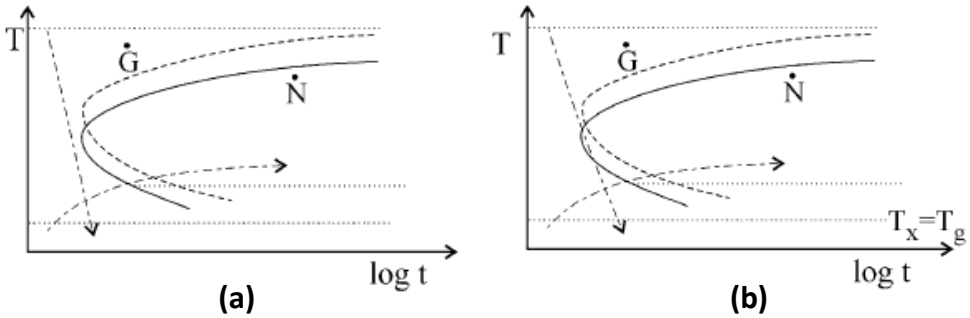

Figure 4.3 Schematic TTT diagrams showing cooling curves and kinetics of (a) nucleation controlled and (b) growth controlled in glass formation. Adopted from [74].

However by this convention there must be a glass transition T_g signal in DSC trace of sputtered film. Instead there is another exothermic peak apart from the peaks that are observed in melt-spun ribbons of the same composition. Thus after this phase separation peak the fcc-Al transformation curve that appears in DSC trace may well overlap with the T_g of the alloy. In this respect the glass transition temperature is reduced for sputtered films which is in accordance with the thermal analysis showing lesser activation energy for the sputtered films of $Al_{90}Tb_{10}$ alloy.

In an earlier study [75] nucleation number density were found using bright-field images for the melt-spun ribbons of the same composition and the average value maintained constant throughout the fcc-Al phase transformation until the intermetallic phase is formed. The average number density for 8 minutes of annealing at 493 K was found as 2×10^{21} m^{-3} by counting the nanocrystals from 20 set of BF images and taking the smallest fcc-Al crystal diameter around 10 nm. Figure 4.4 shows the HRTEM images of melt-spun ribbons and the sputtered films that were isothermally heated in a silicon oil bath for 8 minutes at 493 K. The bright-field images are not shown due to the very fine sizes of fcc-Al nanocrystals within the amorphous matrix of sputtered films. The nucleation number density calculations were done according to the methodology explained earlier in this chapter. Reduced FFTs of corresponding HRTEM images were shown from where the number of crystals in the images was counted. The results found from 30 sets of HRTEM image was calculated to yield a nucleation number density of 7×10^{21} m^{-3} and 5×10^{23} m^{-3} for melt-spun ribbons and sputtered films, respectively.

The differences in the development of fcc-Al nanocrystals upon heating have been shown in many aspects in earlier chapters. At this stage the indications of FEM and HRTEM results along with the phase separation peak observed in DSC trace of sputtered film might enlighten the mystery up to some degree. The pure Al regions that were shown in an earlier study with the use of APT [51] seemed to be responsible for the primary crystallization. Specifically it appears that the system is already chemically separated in solid amorphous state due to correlations in the liquid structure being frozen with the melt-spinning technique as it turns out to be one the main differences in DSC trace apart from the differences in cooling rate which nearly three orders of magnitude. However the interpretation should be carried out very carefully since the change in cooling rate indeed has an effect in the departure from the equilibrium state that is the main driving force acting for the metastable structures to evolve from the glassy matrix. Carefully designed experiments must be carried out just to probe the effect of cooling rate without letting it involved with the physical state of the system.

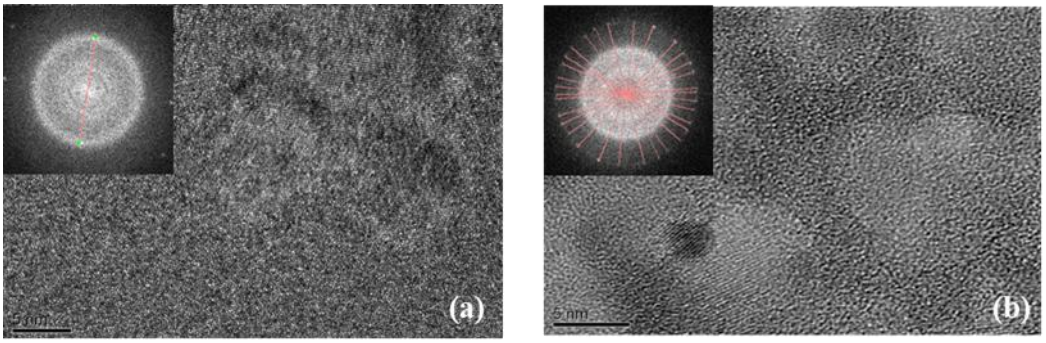

Figure 4.4 HRTEM results of (a) melt-spun ribbon (b) sputtered film of $Al_{90}Tb_{10}$ alloy annealed for 8 minute at 493 K.

It can be only topological or only energetic means or both at the same time that triggers the phase separation peak occurs in sputtered films yet a fact remains indisputable, the differences observed in FEM and XRD experiments. Combining the HRTEM results with the former ones, higher number of nucleation density of the fcc-Al nanocrystals with smaller sizes observed in sputtered films shows a correlation between the reduction in fcc-Al like MRO structure that in turns cause a separation possibly in smaller scales than what occurs in melt-spun ribbons in as-quenched state. In fact a finer scaled network that consists of pure Al islands in sputtered films can be attributed to the higher number of density and smaller size of fcc-Al nanocrystals that emerge from the amorphous matrix.

Figure 4.5 shows the selected area electron diffraction (SAED) patterns of melt-spun ribbons and the sputtered films of $Al_{90}Tb_{10}$ after annealing for 8 minutes at 493 K. A glance in the SAED patters reveals an obvious difference which is the diffraction pattern of the sputtered film having nearly perfect rings of Al reflections whereas melt-spun ribbons have relatively fewer reflections. That is in accordance with the number density calculations made out of HRTEM images indicating the nucleation number density of fcc-Al nanocrystals for sputtered films are way much higher than that of melt-spun ribbons.

In addition to this, there is splendid information hidden in the SAED pattern of the sputtered films which can be extracted by simple indexing of the reflections of Al crystals. The (200) reflection is not visible for the samples that are not titled. In other words all the fcc-Al nanocrystals are having a preferred growth direction in partially devitrified sputtered films under isothermal conditions in such a way that none of the (200) planes are positioned parallel to the incoming beam direction or having a really slight intensity on reflection which is veiled by intensity of (111) reflection which is the most intense coherent scattering plane in fcc-Al structure.

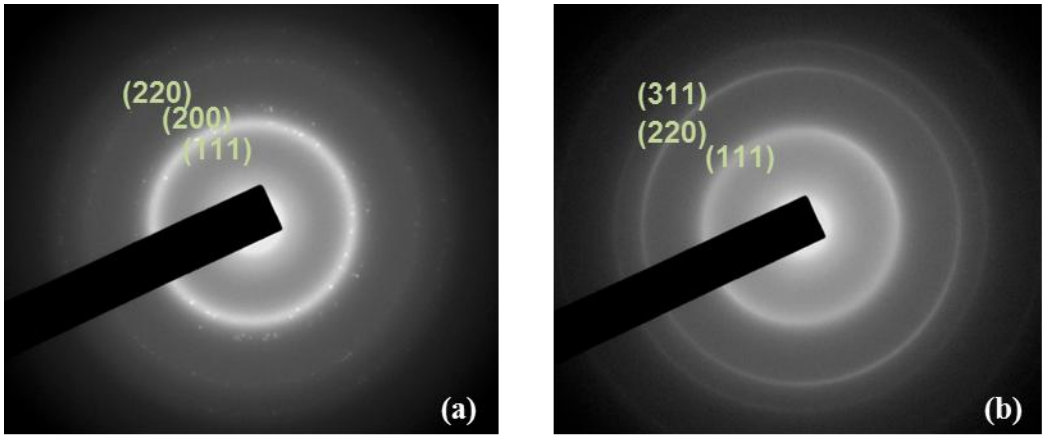

Figure 4.5 SAED of (a) melt-spun ribbon (b) sputtered film of $Al_{90}Tb_{10}$ annealed for 8 minutes at 493 K.

Figure 4.6 shows the SAED pattern for partially devitrified sputtered film of $Al_{90}Tb_{10}$ that is annealed for 8 minutes at 493 K obtained when the sample was tilted 10° in one X axis of TEM. When the sample tilted for some angles and especially for 10° the (200) reflection becomes visible and the other reflections along with (200) reflection have features of preferred orientation. The angular relationships between the first three diffraction rings revealed that the zone axis of the majority of the nanocrystals oriented at [011] direction. In fact that information possesses a great deal of importance when it is combined with other findings. It would not be reasonable to interpret these nanocrystals to be deformed plastically by looking at the most densely packed direction where the slip movement takes place since these nanocrystals are of really small sizes being almost defect free. Another mechanism must be taking place to turn the SAED pattern in such features. A possible explanation can be as follows. Since the number density of fcc-Al crystals in partially devitrified sputtered films are higher and the nanocrystals have smaller sizes, the growth behavior must be different as it was mentioned in Chapter 3. Nucleation might start up from these nanometer scaled network and as the nanocrystals grow, the amount of Tb atom that is expelled to matrix gets much higher compared to that of ribbons. This means that soft impingement occurs in sputtered films well before the normal time scales for the growth of fcc-Al nanocrystals in melt-spun ribbons. However until the concentration of the intermetallic phase evolves after fcc-Al crystallization in isothermal phase sequence of sputtered films is reached, the nanocrystals would try to grow. Thus as more Tb atoms are pushed out to matrix, there would be a stress field acting on nanocrystals of quite small sizes that is insufficient to deform them plastically but sufficient enough to rotate them by the lowest required stress direction. Eventually the corresponding SAED occurs in partially devitrified sputtered films under isothermal conditions.

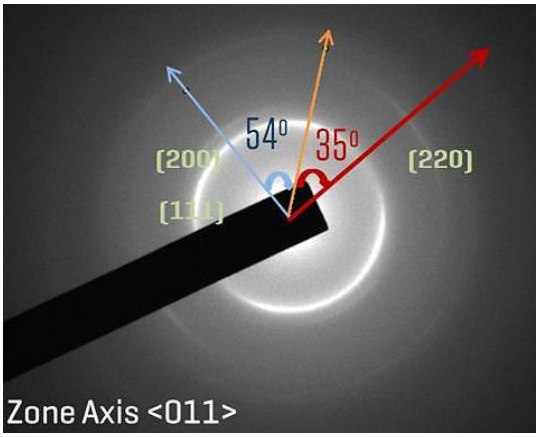

Figure 4.6 SAED of partially sputtered films of $Al_{90}Tb_{10}$ annealed isothermally at 493 K for 8 minutes. The sample was tilted in x direction during TEM investigation.

4.4.1 Growth Model

In order to understand the origin of this possible stress field caused by excessive expel of Tb atoms in sputtered films, a growth model based on composition and time relationships under isothermal conditions were applied. For this purpose careful compositional analyses have been carried out using S/TEM for the ribbons that were annealed isothermally at 493 K for 469 (~ 8 min) and 785 seconds. The utmost care in S/TEM composition analysis was given in order to obtain the composition of the interface between fcc-Al and the amorphous matrix as precise as possible. Figure 4.7 reveals the S/TEM image for 8 minutes annealed melt-spun ribbon in Z-contrast where the high atomic number species appear brighter. In that sense one can observe the brighter color around the fcc-Al. The interface composition after sets of different EDS results were determined to be 14.56 at% Tb and it decays as the probe is moved away from the interface towards the amorphous matrix. For the ribbon sample that is annealed at same temperature until the completion of the fcc-Al transformation that was held for 785 seconds the interface composition was detected as 14.12 at% Tb (image is not shown) which is in good agreement for the assumptions for the growth model to be used. Thus the 14.56 at% Tb is used in growth model to compute the quantity expelled and the related calculations were done according to the interface composition value that was measured by 0.7 nm beam size in Z-contrast S/TEM analysis.

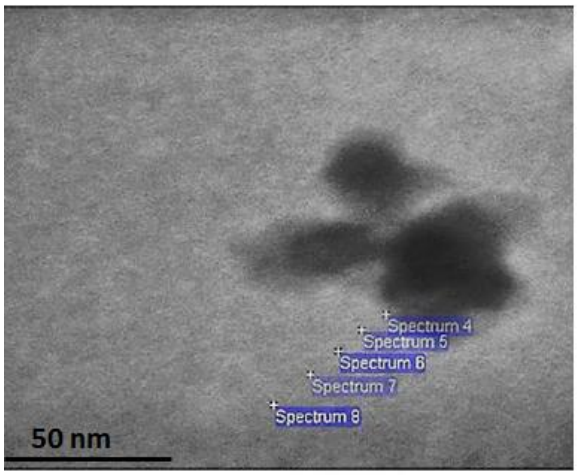

Figure 4.7 S/TEM Z-contrast image of an fcc-Al nanocrystal embedded in amorphous matrix in melt-spun ribbon annealed 8 minutes at 493 K under isothermal conditions.

It is indeed a difficult task to apply the same S/TEM investigations for partially devitrified sputtered films under same conditions since the nanocrystals themselves are quite small and have very close sizes to the beam size. Therefore the EDS result that is obtained would not give as precise results as in the case of sputtered films. For that reason the nanocrystal-matrix interface composition is assumed to be the same for both types of samples.

Frank's solution is used to describe the growth behavior of fcc-Al nanocrystals within the framework of this study. As mentioned earlier in this chapter this approach provides concentration profiles and can be applied to soft impingement conditions unlike JMA approach. The growth diffusion of a particle in spherical symmetry is defined using a function that depends on the reduced radius that is in turn the diffusivity, time and the radius of particle. Yet diffusivity is not a variable for Frank's solution, it is assumed constant throughout the growth process. The growth diffusion function is as follows;

$$F(s) = s^{-1}\exp\left(-\frac{1}{4}s^2\right) - 1\pi^{0.5}[1 - \mathrm{erf}\left(\frac{1}{2}s\right)] \qquad \text{Equation 4.7}$$

As the quantity such as heat or concentration is expelled, the reduction trend can be given by the above equation in a spherical growing phase so that the radius of the particle R is proportional to $t^{1/2}$ when $S = R/\sqrt{Dt}$ where $f(S)$ can be introduced as the reduced undercooling or supersaturation depending on the variations of the function. For the small values of s, the growth limited diffusion of a component in a particular system can be modeled by taking S~1.5 [67] and this was successfully applied for the growth of fcc-Al particles when yttrium was the growth limited diffusing element in Al-Y-Fe ternary marginal glass forming system [68]. In this respect the interface concentration that is maintained constant during the growth of the particle is given by;

$$C - C_0 = \frac{1}{2}(C_m - C_p)S^3 exp\left(\frac{S^2}{4}\right) F(s)$$ Equation 4.8

where C is the composition ahead of interface, C_0 is the nominal composition, C_m is the composition of matrix and C_p is the composition of the precipitate. In $Al_{90}Tb_{10}$ binary system the precipitation composition is taken as 100% Al and S is taken to be 1.5. The quantity expelled was found from the S/TEM interface composition analysis and introduced to the equation. In order to find the diffusivity of Terbium in amorphous matrix as the particle grows TEM analysis of the melt-spun ribbons of $Al_{90}Tb_{10}$ was carried out. Applying the particle growth with time and taking S as 1.5 a linear relationship has been found. From the predetermined times of annealing and a constant slope of the curve yielded to a D value of 2.5×10^{-19} m/s^2. Figure 4.8 shows the average radius of growing fcc-Al nanocrystals at different time durations of isothermal annealing at 493 K found by TEM analysis of melt-spun ribbons. It should be noted that the matrix is assumed to have an infinite size so that the matrix composition is equal to the nominal composition.

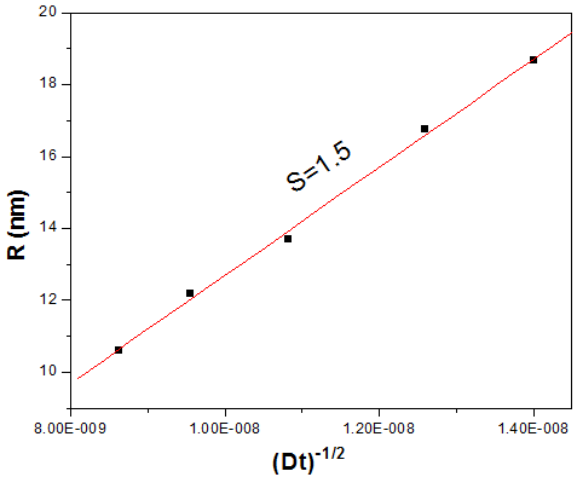

Figure 4.8 Diffusivity of Tb atoms with time under isothermal conditions at 493 K.

Application of Frank's solution was combined with the interface composition obtained by S/TEM for partially devitrified melt-spun ribbons for different times of the transformation dictated by the isothermal DSC trace at 493 K is shown in Figure 4.9. In Figure 4.9 (a) composition profile an isolated nanocrystal assumed to have spherical diffusion symmetry is shown at different times from the beginning to the end of the transformation. It should be noticed that interface composition is kept constant and as transformation pursues the Tb content in the matrix is increased for a fixed displacement from the interface of a particular fcc-Al nanocrystal.

In Figure 4.9 (b) the composition profiles of two fcc-Al nanocrystals growing towards each other within the amorphous matrix is shown. The nanocrystals are separated by 25 nm which

was taken as average separation distance of nanocrystals in partially devitrified melt-spun ribbons nm. It should be noted that the graph only shows the growth in one direction. However the assumption relies on growth in spherical symmetry. Thus it can easily be thought that same would happen in other directions if two isolated nanocrystals separated with the distance appears in the figure. One can see the difference of the overlapping of concentration profiles at higher concentrations as the transformation proceeds. Besides, as mentioned earlier this is only showing one dimensional representation. Therefore bearing in mind the spherical symmetry, the Tb content would be even higher in three dimensions and eventually the soft impingement which affects the system to be more sluggish in growth takes place.

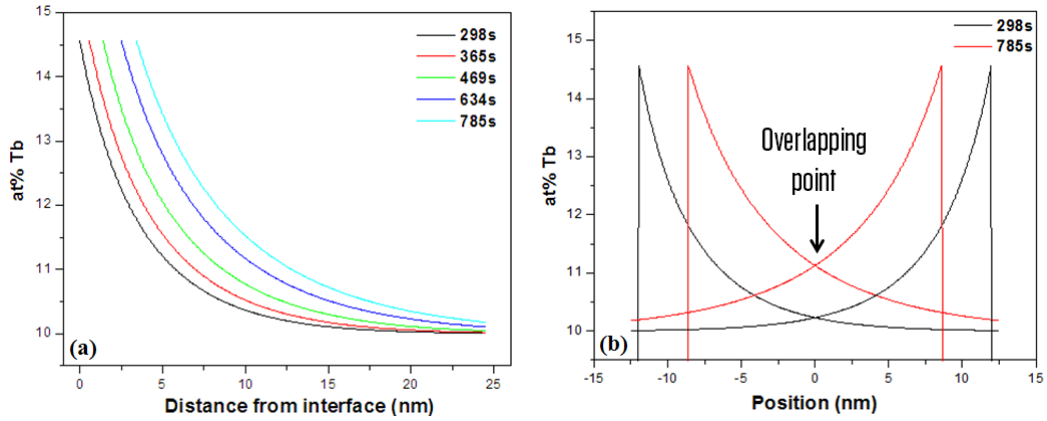

Figure 4.9 (a) composition profile of an isolated fcc-Al nanocrystal in partially devitrified melt-spun ribbons annealed at 493 K under isothermal conditions (b) composition profiles of two fcc-Al nanocrystals growing towards each other under same conditions.

Using the same growth model along with the same interface composition, isothermal growth behavior of fcc-Al nanocrystals in partially devitrified sputtered films can be modeled. According to Frank's rigorous solution, growth of particles having spherical symmetry involving soft impingement of sluggish diffusion S was taken as 1.5 as well. Even though it has been shown that growth mechanism differs for the fcc-Al nanocrystals in sputtered films this model is applied to show the difference in Tb content in matrix with change in time compared to that of melt-spun ribbons. Thus it is assumed that the diffusivity in Tb in amorphous matrix is independent of nucleation and growth mechanism as well as the Tb content in matrix.

Figure 4.10 shows the evolution of two fcc-Al nanocrystals annealed at 493 K for different times. The main difference in the composition profile compared to Figure 4.9 (b) is that the average distance between two nanocrystals were taken to be 9 nm unlike that in melt-spun ribbons. It can easily be observed that as nanocrystals evolve with time, the composition profiles overlap at higher Tb contents as expected. Moreover this effect is more prevailed

due to the fact that the number density of fcc-Al nanocrystals in sputtered films is much higher than that of melt-spun ribbons. Therefore the increase in the Tb content as each and every nanocrystal grows in amorphous matrix may cause a stress field acting to rotate the crystals since expectation of a plastic deformation would be irrelevant as far as the purity of the nanocrystals are concerned.

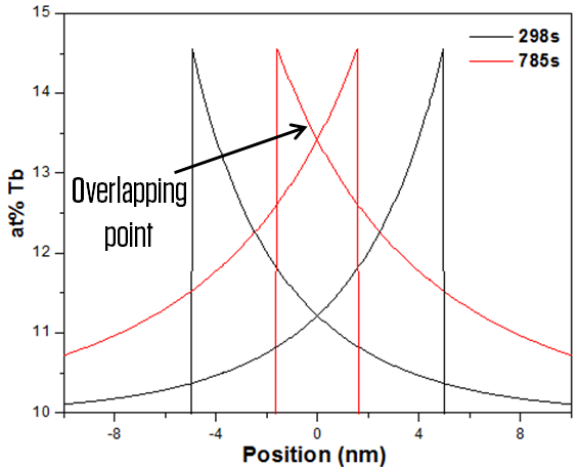

Figure 4.10 Composition profiles of two fcc-Al nanocrystals growing towards each other in partially devitrified sputtered film annealed at 493 K under isothermal conditions.

4.5 Conclusion

The effect of altering the amorphization precursor on the amorphous structure was shown by FEM analysis for the melt-spun ribbons and sputtered films having liquid and vapor precursor, respectively. The amorphous structure revealed higher intermixing of Al and Tb elements for the films as expected. Furthermore a decrease the fcc-Al like MRO order that is said to be inherited from the liquid state was observed. Controlled devitrification of these samples under isothermal conditions was investigated using TEM in order to enlighten the mystery of nucleation mechanism in marginal glass forming alloys. Higher nucleation number density of fcc-Al nanocrystals was detected. This was attributed to the smaller scale division of pure Al regions within the network in sputtered film and more it was particularly inferred that the nucleation might preferentially originated from these zones thus ending up in a higher number density. A texturing behavior was observed in SAED of partially devitrified sputtered films when the zone axis was set to be <011>. This was attributed to a possible stress field arising upon the growth of fcc-Al nanocrystals in sputtered films due to the excessive Tb atoms expelled to matrix as growth of nanocrystal proceeds. In this respect a growth model based on Frank's solution that involves constant interface concentration in spherical symmetry diffusion was applied to melt-spun ribbons and sputtered films for better monitoring and analyzing the growth mechanism of the primary crystallization that was

elaborated in Chapter 3 since JMA approach is already disturbed by the inhomogeneity of the system as far as the network type distribution of Al and Tb atoms are concerned as well as the sluggish diffusion due to soft impingement. The nanocrystal-amorphous interface composition was found using EDS under S/TEM investigation. Results were compared with the experimental composition data obtained by EDS for melt-spun ribbons and showed good agreement.

CHAPTER 5

CONCLUSION AND FUTURE RECOMMENDATIONS

5.1. Conclusion

The effect of altering the amorphization precursor from liquid to vapor phase on phase selection, nucleation and growth behavior and topological order in amorphous states in Al-Tb marginal glass forming alloys were studied in the content of this thesis.

Phase selection hierarchy was investigated using XRD, TEM and DSC analysis in the first part of the study. The difference in the amorphization methods was observed to lead different devitrification pathways. Isochronal DSC traces revealed shifts in exothermic peaks along with changes in peak shapes which imply the difference in the amorphization methods leads to different devitrification pathways for melt-spun ribbons and sputtered films. Synchrotron XRD was used to monitor stepped isochronal heating behavior as to how devitrification proceeds. A change in the phase transformation sequence was observed for the two type of samples. TEM analysis showed morphological difference of the evolving phases. Especially the size and shape difference for fcc-Al nanocrystallization and the first intermetallic phase formation between melt-spun ribbons and sputtered films is remarkable.

The second part of the study involves thermal analysis of the fcc-Al nanocrystallization in Al-Tb alloys. Isochronal and isothermal DSC traces were used in order to explain the nucleation and growth behavior with the use of different methods. Activation energies were calculated using Kissinger and Ozawa methods. Isochronal activation energies showed difference for the fcc-Al nanocrystallization between two types of samples. Furthermore JMA approach and Matusita analysis on nucleation and growth behavior of melt-spun ribbons and sputtered films indicated change in the mechanisms of primary crystallization. This was attributed to the exothermic event occurs well before the fcc-Al phase transformation. In addition, the circumstances to make a correlation of Kissinger activation energy and isothermal activation energy were also discussed in the second part of the study.

The last part of the study consists of controlled devitrification of melt-spun ribbons and sputtered films of Al-Tb alloy under isothermal conditions. In addition to differences shown in amorphous states in previous parts FEM investigation of as-spun and as-sputtered samples were done to probe the change in topological ordering. The results suggested that fcc-Al like MRO is reduced for sputtered films. Partially devitrified samples were examined under TEM and the nucleation number density of the fcc-Al nanocrystals was detected to be higher in sputtered films. This was attributed to the finer scale network in amorphous states prior to devitrification. Furthermore it was shown that the system needs to arrange itself in a chemically separated state prior to crystallization due to the fact that a phase separation event happens for sputtered film whereas the amorphous state of ribbons has already 1 nm pure Al

regions that are said to be inherited from the liquid structure. Therefore the system does not undergo any step such as phase separation before devitrification. The last part of the study includes a growth model for fcc-Al nanocrystals under isothermal conditions. Frank's solution was applied for both types of samples in such a way that the constant interface composition was used according to the composition analysis carried out by EDS under S/TEM examination. The contradictions to the assumptions of JMA approach such as structural homogeneity and soft impingement effect were overcome. Thus with the use of this model a possible stress field that may occur as the fcc-Al nanocrystals advances to grow in sputtered films due to the increased amount of Tb content that is pushed out was numerically represented in composition profiles. Therefore the texture occurs in SAED of partially sputtered film was explained in this manner.

5.2. Future Recommendations

The origin of the network type amorphous structure divided by pure Al regions that were shown in earlier studies was supported in this work with the results. It is still an unknown if the MRO appearing in amorphous state is inherited from the liquid structure or the cooling rate is not sufficient to obtain a more homogenous amorphous state. In this study this dilemma was examined using a different amorphization precursor which led to decrease in MRO order and increased number density of fcc-Al nanocrystals upon. However in order to be more clear as to how the nucleation affect from the topological ordering, the cooling rate parameter has to be avoided by different experimental set-ups which are required to be implemented to clarify this issue. The difficulty of such experiment may be surpassed with a comprehensive atomic simulation where synchrotron XRD results shown in this work can be used to furnish the atomic coordinates for sputtered. This would provide a capability of simulating higher intermixing of atoms with a decrease in fcc-Al like MRO to show the topological effects in the absence of cooling rate. Energy levels can be compared with that of ribbon with the use of atomic simulations in order to see if a lower energy state can be obtained in that configuration.

One of the most important future studies should consist of solving the structures of intermetallic phases evolve in sequence showed in Chapter 2 and labeled as second and third transformation, respectively. The space groups of these phases along with the lattice constants should be found out.

A fruitful future work may be use of APT for sputtered films both for as-sputtered case and for a heat treatment consist of heating the system to phase separation state and quenching. The former experiment might provide valuable information if the system has a "pseudo-grained" structure which is thought to be affecting the nucleation and growth behavior of fcc-Al nanocrystals. For the latter experiment, the pure Al regions that are expected to occur according to the framework of this study can be compared with that of melt-spun ribbons. This may enlighten the theory of the effect of topological ordering on nucleation mechanism

in a brighter fashion and also may reveal a better solution for the increased nucleation number density in sputtered films.

Another possible way to show the relationship between the topological ordering and nucleation can be EXAFS study. The coordination around Tb atoms that were studied earlier by atomic simulations can be analyzed in a great precision both for melt-spun ribbons and sputtered films. Therefore the possibility of liquid structure possessing a structure beyond short range order may be elaborated.

Apart from the efforts related to understand the enigmatic nucleation and growth behavior of marginal glass forming alloys, corrosion resistance of Al-Tb system can be studied. Amorphous thin films can be applied to crucial tiny components by sputtering processes in case the corrosion resistance studies give satisfactory results. In addition to that, better mechanical tests to understand the deformation mechanism should be performed to observe possible shear bands in sputtered films. However even if the consistency in mechanical properties is achieved a more complex concern still holds. Bulk production of these systems will remain as a bigger challenge that acts as a barrier for these materials to be used in certain applications. Thus new processes or alloy design can be seen as a future study.

REFERENCES

[1] Yavari A.R., Lewandowski J.J., Eckert J., Mechanical properties of bulk metallic glasses, MRS Bull. 32 (2007) pp. 635.

[2] Louzguine D.V., Inoue A. Comparison of the long-term thermal stability of various metallic glasses under continuous heating, Scr. Mater. 47 (2002) 887.

[3] Klement W., Williens R.H., Duwez P., Non-crystalline structure in solidified gold-silicon alloys, Nature 187 (1960) pp. 869 – 70.

[4] Chen HS, Turnbull D. Formation, Stability and structure of palladium-silicon based alloy glasses. Acta Metall. 17 (1969) pp.1021–31.

[5] Kui HW, Greer AL, Turnbull D. Formation of bulk metallic glass by fluxing. Appl. Phys. Lett. 45 (1984) pp. 615–6.

[6] Inoue A., Amorphous, nanoquasicrystalline and nanocrystalline alloys in Al-based systems, Prog. Mater. Sci. 43 (1998) pp. 365 – 520.

[7] Inoue A., Zhang T., Masumoto T. Al–La–Ni amorphous alloys with a wide supercooled liquid region. Mater Trans JIM 30 (1989) pp. 965–72

[8] Peker A., Johnson W. L., A highly processable metallic glass $Zr_{41.2}Ti_{13.8}Cu_{12.5}Ni_{10.0}Be_{22.5}$, Appl Phys Lett 63 (1993) pp. 2342–4.

[9] Gorant J., Liquid golf, Popular Mechanics 175 (1998) pp. 30

[10] A. Inoue, T. Zhang, J. Saida, M. Matsushita, M. Chen, T. Sakurai, Mat. Trans. JIM 40 (1999) pp. 1181

[11] Löffler J. F., Bulk metallic glasses, Intermetallics, 11 (2003) pp. 529-540

[12] Busch R., Bakke E., Johnson W.L., Viscosity of the supercooled liquid and relaxation at the glass transition of the Zr46.75Ti8.25Cu7.5Ni10Be27.5 bulk metallic glass forming alloy, Acta Mater. 46 (1998) pp. 4725 – 4732.

[13] Suryanarayana C., Inoue A, Bulk Metallic Glasses, CRN Press (2011), pp. 16-160

[14] Perepezko J.H., Nucleation-controlled reactions and metastable structures, Progress in Materials Science, 49 (2004) pp.263-87

[15] Angell C.A., Formation of glasses from liquids and biopolymers, Science 267 (1995) pp. 1924–35.

[16] Turnbull D., Metastable structures in metallurgy. Metall. Trans. B 12 B (1981) pp. 217–30.

[17] Turnbull D., Under what conditions can a glass be formed? Con- temp. Phys. 10 (1969) pp. 473–88.

[18] Busch R, Schroers J, Wang WH., Thermodynamics and kinetics of bulk metallic glass. MRS Bull (8) (2007);32 pp. 620–3.

[19] Adam G., Gibbs J.H., On temperature dependence of cooperative relaxation properties in glass-forming liquids. J Chem Phys 1 (1965);43 pp. 139.

[20] Richert R., Angell C. A., J. Chem. Phys. 108 (1998) pp. 9016.

[21] Goitiandia L., Alegría A., The Adam–Gibbs equation and the out-of-equilibrium α relaxation of glass forming systems J. Chem. Phys. 121 (2004) pp. 1636.

[22] Inoue A., Stabilization of metallic supercooled liquid and bulk amorphous alloys, Acta Mater. 48 (2000) pp. 279 – 306.

[23] Greer A. L., Confusion by design, Nature 366 (1993) pp. 303.

[24] Frank F. C., Supercooling of liquids, Proc. R. Soc. A 215 (1952) pp. 43 .

[25] Miracle D.B., A structural model for metallic glasses, Nat. Mater. 3 (2004) pp. 697 – 702.

[26] Iwamatsu M., Lai S. K., Lowest-energy structures of 13-atom binary clusters: Do icosaheldral clusters exist in binary liquid alloys, J. Non-Cryst. Solids 353 (2007) pp. 3698 – 3703.

[27] Sheng H. W., Luo W. K., Alamgir F. M., Bai J. M. & Ma E. Atomic packing and short-to-medium-range order in metallic glasses, Nature 439 (2006), pp. 419-425.

[28] Liebermann, H., Graham, C., Production of amorphous alloy ribbons and effects of apparatus parameters on ribbon dimensions, IEEE Transactions on Magnetics 12 6 (1976) pp. 921–923.

[29] Materials Preparation Center, A.L., US DOE Basic Energy Sciences, Ames, IA, USA, http://www.ameslab.gov/mpc. (Last visited on: 17.02.2013).

[30] Yasui K., Phuong P. Y., Kuroiki Y., Takata M., Akahane T.,Improvement in crystallinity of ZnO Films Prepared by rf magnetron sputtering with grid electrode, Jpn. J. Appl. Phys. 44 (2005) pp. 684-87.

[31] Sagel A., Sieber H., Perepezko J.H., Synthesis of an amorphous Zr–Al–Ni–Cu alloy with large supercooled liquid region by cold-rolling of elemental foils Acta Mater 46 (1998) pp. 4233.

[32] Suryanarayana, C., Inoue, A., Iron based bulk metallic glasses, Internatinal Materials Reviews, 58 (2013) pp.131-66.

[33] Johnson, W.L., Thermodynamic and kinetic aspects of the crystal to glass transformation in metallic materials. Prog. Mater. Sci. 30 (1986) pp. 81–134.

[34] Aoki, K., Amorphous phase formation by hydrogen absorption. Mater.Sci. Eng. A 304–6 (2001) pp. 45–53.

[35] Battezzati, L., Thermodynamics of metastable phase formation. Phil.Mag. B 61(1990) pp 511-24.

[36] Indian Academy of Science, Resonance, http://www.ias.ac.in (2009) pp. 807-807, (Last Visited on: 05.04.13).

[37] Kooi B.J, Groot M. G., De Hosson J. Th. M., In situ transmission electron microscopy study of the crystallization of $Ge_2Sb_2Te_5$ J. Appl. Phys. **95** (2004) pp.924-33

[38] Guo H., Yan P. F., Wang, Y. B., Tan, J, Zhang, Z. F., Sui, M. L., Ma, E., Tensile ductility and necking of metallic glass, Nature materials 6 (2007) pp. 735 – 39.

[39] Kalay Y.E., Chumbley L.S., Anderson I.E., Characterization of a marginal glass former alloy solidified in gas atomized powders, Mater. Sci. Eng. A 490 (2008) pp. 72 – 80.

[40] Voyles, P. M., Gibson, J. M., Treacy, M. M. J, Fluctuation microscopy: a probe of atomic correlations in disordered materials, Journal of Electron Microscopy 49 (2000) pp. 259 – 66.

[41] Fluctuation Microscopy https://tem.msae.wisc.edu/fluctuation-microscopy/ (Last visited on 25.05.2013).

[42] EXAFS Spectroscopy, http://www.dragon.lv/exafs/about_exafs.htm (Last visited on 28.05.13).

[43] Diamond UK lightsource, www.diamond.ac.uk//Home/About/Synchrotrons (Last Visited on: 06.04.2013).

[44] Elettra www.elettra.trieste.it/lightsources/elettra/elettra-beamlines (Last visited on 24.05.2013).

[45] Inoue A., Kitamura A., Masumoto T. J., Mater. Sci. 1981;16:1895.

[46] A. Inoue, K. Ohtera, A.P. Tsai, T. Masumoto, New Amorphous with good ductility in Al-Y-M and Al-La-M (M=Fe,Co,Ni or Cu) Systems, Jpn. J. Appl. Phys. 27 (1988) L280.

[47] Y. He, S.J. Poon, G.J. Shiflet, Synthesis and Properties of Metallic Glasses that Contain Aluminum Science 241 (1988) 1640.

[48] Battezzati L., Kusy M., Ronto V, Al-Rare-earth-Transition Metal Alloys: Fragility of Melts and Resistance to Crystallization, Properties and Applications of Nanocrystalline Alloys from Amorphous Precursors NATO Science Series 184 (2005) pp. 267-278

[49] Battezzati L, Pozzovivo S., Rizzi P., Phase Transformations in $Al_{87}Ni_7Ce_6$ and $Al_{87}Ni_7Nd_6$ Amorphous Alloys, Materials Transactions, 43(2002) pp. 2593-2599

[50] Sabetshargi R,, Altounian Z., Muir W.B., Formation, Structure and Crystallization of Al-Rich Metallic Glasses, J. App. Phys, 74 (1994) pp. 4438

[51] Kalay Y.E., Kalay I., Hwang J., Voyles P.M., Kramer M.J., Local chemical and topological order in Al-Tb and its role in controlling nanocrystal formation, Acta Mater. 60 (2012) pp. 994 – 1003.

[52] Lin g.J., Wang W.W.,Wu X.Q.,Lei J.H.,Yin S.,Crystallization and corrosion resistance of as-spun $(Al_{86}Ni_9La_5)_{98}Zr_2$ amorphous alloy, Journal of Alloys and Compounds,478 (2009) pp. 763-766.

[53] Cheng Y.Q., Ma E., Atomic-level structure and structure-property relationship in metallic glasses, Prog. Mater. Sci. 56 (2011) pp. 379.

[54] Hammersley A.P, ESRF Internal Report, ESRF98HA01T, FIT2D V9.129 Reference Manual V3.1 (1998).

[55] Kissinger H.E., Reaction Kinetics in Differential Thermal Analysis, Anal. Chem. 29 (1957) pp.1702.473.

[56] T. Ozawa, Bull. Chem. Soc. Jpn., 38 (1965).

[57] Matusita K.,Komatsu T.,Yokota R, Kinetics of non-isothermal crystallization process and activation energy for crystal growth in amorphous materials, J. Mater. Sci. 19 (1984) pp.291.

[58] N. Afify, M.A. Abdel-Rahim, A.S. Abdel-Halim, M.M. Hafiz, J. Non-Cryst. Solids 128 (1991) 269

[59] Kalay Y.E., Chumbley S., Anderson I.E., Crystallization behavior in highly driven marginal glass forming alloy, J. Non-Cryst. Solids 354 (2008) pp. 3040 – 3048.

[60] Li X. P., Yan M., Yang B. J., Wang J. Q., Schaffer G. B., Qian M., Crystallization behaviour and thermal stability of two aluminium-based metallic glass powder materials, Mater. Sci. Eng. A 530 (2011) pp. 432- 439.

[61] Ruitenberg G., Woldt E., Petford-Long A.K., Comparing the johnson-mehl-avrami-kolmogorov equations and linear heating conditions,Thermochim. Acta 378 (2001) pp.97.

[62] Pratap A., Kirit N., Rao T.,Majmudar P, Saxena N. S., Kinetics of crystallization of amorphous $Cu_{50}Ti_{50}$, J. Non-Cryst. Solids 345 (2004) pp. 178-181.

[63] Venkataraman S., Hermann H., Mickel C., Shultz L., Sordelet J.D., Eckert J., Calorimetric Study of the crystallization kinetic of $Cu_{47}Ti_{33}Zr_{11}Ni_8Si_1$, Phys. Rev. B. 75 (2007) pp. 104206:1-104206:9.

[64] Schroers J., Busch R. Masuhr A., Johnson W. L., Continuous refinement of the microstructure during crystallization of supercooled $Zr_{41}Ti_{14}Cu_{12}Ni_{10}Be_{23}$ melts, Appl. Phys, Lett 74 (1999) pp. 2806-2809.

[65] Wilde G., Sieber H., Perepezko JH., Glass formation versus nanocrystallization in an $Al_{92}Sm_8$ alloy, Scripta Mater. 40 (1999) pp. 779 – 783.

[66] Gangopadhyay A.K., Croat T.K., Kelton K.F., The effect of phase separation on subsequent crystallization in $Al_{88}Gd_6La_2Ni_4$, Acta Mater. 48 (2000) pp. 4035 – 4043.

[67] Kelton K.F., Time-dependent nucleation in partitioning transformations, Acta Mater. 48 (2000) pp. 1967-1980.

[68] Ham F.S., Theory of diffusion-limited precipitation, J. Phys. Chem. Solids, 6 (1958) pp. 335-351.

[69] Frank F., Radially symmetric phase growth controlled by diffusion, Proc. Royal Soc. A. 201 (1950) pp.586-599.

[70] Allen D.R., Foley J.C., Perepezko J.H., Nanocrystal development during primary crystallization of amorphous alloys, Acta Mater. 46 (1998) pp. 431 – 440.

[71] Stratton W.G., Medium Range Order in High Aluminum Content Amorphous Alloys Measured by Fluctuation Electron Microscopy, Ph.D. Thesis, (2007) University of Wisconsin-Madison, pp. 51.

[72] Hebert R.J., Perepezko J.H., Effect of cold-rolling on the crystallization behavior of amorphous $Al_{88}Y_7Fe_5$ alloy, Mater. Sci. Eng. A 375 – 377 (2004) pp. 728 – 732.

[73] Cahn J.W., Nutting J., Transmission quantitative metallography, Trans. Met. Soc. A.I.M.E. 215 (1959) pp. 526 – 528.

[74] Perepezko J.H., Hebert R.J., Tong W.S., Amorphization and nanostructure synthesis in Al alloys, Intermetallics 10 (2002) pp. 1079 – 1088.

[75] Demirtaş T., Kalay, Y. E., Kinetics of fcc-Al nanocrystallization in $Al_{90}Tb_{10}$ Metallic Glass, J. Non-Cryst. Solids 378 (2013) pp. 71-78.

[76] Jin L., Kang Y.B., Chartrand P., Fuerst C.D., Thermodynamic evaluation and optimization of Al-Gd, Al-Tb, Al-Dy, Al-Ho and Al-Er systems using a modified quasichemical model for the liquid, CALPHAD 34 (2010) pp. 456 – 466.

APPENDIX A

EQUILIBRIUM PHASE DIAGRAM OF Al-Tb SYSTEM

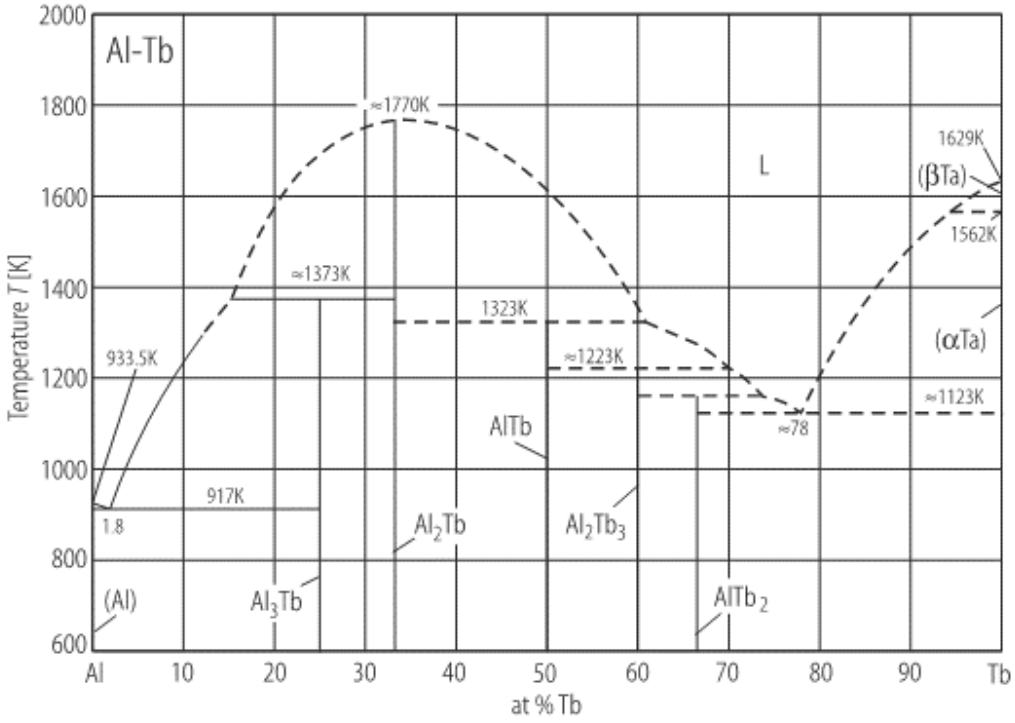

Figure A.1 The calculated equilibrium phase diagram of Al-Tb system by CALPHAD software [76].

APPENDIX B

THE GROWTH-DIFFUSION AND DIFFUSION-GROWTH FUNCTIONS

	spherical case 3 dimensions		cylindrical case 2 dimensions	
s or S	$F(s)$	$f(S)$	$F_2(s)$	$f_2(S)$
0	∞	0	∞	0
0·1	9·1388	$0{\cdot}4580 \times 10^{-2}$	2·7059	0·01356
0·2	4·1639	0·01682	2·0190	0·04080
0·3	2·5176	0·03476	1·5973	0·07351
0·4	1·7133	0·05706	1·3406	0·1116
0·6	0·9282	0·1097	0·9594	0·1890
0·8	0·5586	0·1678	0·7046	0·2646
1·0	0·3539	0·2272	0·5221	0·8352
1·2	0·2303	0·2852	0·3872	0·3996
1·4	0·1521	0·3405	0·2860	0·4576
1·6	0·1010	0·3923	0·2098	0·5094
1·8	0·06716	0·4402	0·1525	0·5554
2·0	0·04454	0·4843	0·0097	0·5964
2·2	0·02938	0·5245	0·0780	0·6327
2·4	0·01924	0·5612	0·0547	0·6650
2·6	0·01249	0·5946	0·0379	0·6937
2·8	0·008020	0·6250	0·0258	0·7193
3·0	0·005095	0·6525	0·0174	0·7421
3·2	0·003197	0·6776	0·0115	0·7625
3·4	0·001981	0·7004	0·00751	0·7808
3·6	0·001200	0·7211	0·00483	0·7972
3·8	0·0007296	0·7400	0·00304	0·8120
4	0·0004334	0·7572	0·00190	0·8254
5	0·00002544	0·8236	0·000150	0·8757
6	$10^{-6} \times 0{\cdot}9910$	0·8673	0·000006	0·9078

Figure B.1 The diffusion-growth and growth-diffusion functions that are used in Frank's solution [69].